Diss. ETH No. 14045

# Investigation and Improvement of
# Airborne Laser Scanning Technique for
# Monitoring Surface Elevation Changes of Glaciers

A dissertation submitted to the

SWISS FEDERAL INSTITUTE OF TECHNOLOGY ZURICH

for the degree of

Doctor of Technical Sciences

presented by

ETIENNE FAVEY

Dipl. Verm. Ing. ETH

born October 26, 1971

citizen of Stäfa, ZH, Pompaples, VD and Eclépens, VD

accepted on the recommendation of

Prof. Dr. H.-G. Kahle, examiner

Prof. Dr. A. Grün, co-examiner

Zurich 2001

*To my wife and her support through this long task.*

# Abstract

Headlines of global warming and melting glaciers predict sustainable climate changes for future generations. How much mass the glaciers actually loose, has been—despite its importance—investigated only for a few glaciers, as in-situ measuring methods are time-consuming and usually under-sampled.

Airborne laser scanning is a young technology opening new possibilities for qualitative and quantitative determination of surface elevation changes of glaciers. Its rise was possible through the combination of several modern measuring methods, such as high-precision DGPS positioning in kinematic mode, attitude measurements using inertial systems, and laser distance measurements to non-cooperative targets.

This work investigates the feasibility and possible improvements of the airborne laser scanning technique with respect to the special circumstances of determining surface elevation changes of glaciers. This consists of an error analysis of the method as well as the scrutiny of its limitations, and its application to remote, alpine areas without the need of in-situ measurements.

The key problem consists in bringing together all necessary elements for georeferencing the laser data, where the quality of each contributing part has to be monitored regarding accuracy and systematic effects. The quality of the GPS trajectory can be degraded by various factors like atmospheric refraction, radio frequency interference, or obstruction of satellite visibility. The reliable identification of the integer-valued carrier phase ambiguities can be hindered or even made impossible by such effects. The attitude solution was realized using an inertial measurement unit. A separate attitude solution with lower accuracy using a GPS multi-antenna array was developed and used to control and correct IMU drift and offset errors. A self-calibration procedure for determining boresight misalignment angles was elaborated. The used laser scanning system showed increased blunder effects with low received signal power. An approach for detecting and removing blunder was implemented.

Using the laser scanning solution presented in this work, a height accuracy of 0.3 m could be realized flying over a runway at 500 m above ground. Higher flying height above ground and turbulences impede the realization of this data quality in the mountains; it amounts to about 0.5 m.

In the test area at Unteraargletscher, Bernese Alps, Switzerland, measurements for a temporal analysis were repeatedly made using the laser scanning technique. For the lower parts of Unteraargletscher, digital surface models originating from photogrammetry are available for comparison. The determination of the surface elevation change distribution was shown to be feasible with an accuracy of 0.5–0.7 m.

The areas covered by airborne laser scanning are located between 2500 and 3400 m above sea level. For the period 1998–1999, a surface elevation increase of 2–4 m was

measured. This positive change can be related to the immense amount of snowfall during the winter 98/99.

The coverage of Unteraargletscher with measurements of surface elevation change could be completed up to the remote firn areas thanks to the airborne laser scanning technique. It is available for mass balance and flow modeling calculations.

# Zusammenfassung

Pressemeldungen von globaler Erwärmung und schmelzenden Gletschern prophezeien nachhaltige Klimaveränderungen für kommende Generationen. Wieviel die Gletscher tatsächlich an Masse verlieren, wurde — trotz seiner Wichtigkeit — aufgrund der zeitaufwändigen und örtlich beschränkten Messmethoden vor Ort bisher nur für wenige Gletscher gemessen.

Fluggestütztes Laserscanning, eine junge Technologie möglich durch die Vereinigung moderner Messmethoden wie hochpräziser kinematischer GPS-Positionierung, Lagewinkelbestimmung durch inertiale Messsysteme, und reflektorlose Laserdistanzmessungen, eröffnen neue Möglichkeiten für die qualitative und quantitative Erfassung von Höhenveränderungen von Gletschern.

Diese Arbeit untersucht die Durchführbarkeit und Verbesserungsmöglichkeiten der fluggestützten Laserscanning-Technik im Hinblick auf die speziellen Umstände, die bei der Erfassung von Höhenänderungen von Gletschern vorliegen. Dies beinhaltet eine Fehleranalyse der Methode an sich, sowie die Erforschung ihrer Grenzen und ihrer Anwendbarkeit auf entfernte, alpine Regionen ohne notwendige Bodenmessungen im Zielgebiet selbst.

Das zentrale Problem besteht im Zusammenfügen aller nötigen Elemente zur Georeferenzierung der Laserdaten, wobei die Qualität der beitragenden Systeme hinsichtlich Genauigkeit und systematischer Effekte überprüft werden muss. Die Qualität der GPS Trajektorie kann durch verschiedene Faktoren wie atmosphärische Refraktion, Störsignale, oder Abschattungseffekte stark beeinträchtigt werden, da die Lösbarkeit möglichst vieler Phasenmehrdeutigkeiten dadurch verringert oder gar verunmöglicht wird. Für die Lagewinkelbestimmung wurde eine Lösung aus mehreren GPS-Antennen realisiert, um die Drift- und Versatzeffekte des Intertialsystems zu bestimmen und zu korrigieren. Für die Bestimmung der Einbauwinkel des Lasersystems relativ zum Inertialsystem wurde eine Selbstkalibration anhand der gemessenen Daten realisiert. Das verwendete Lasersystem zeigte zudem Fehlereffekte bei niedriger Empfangssignalstärke. Für deren Erkennung und Elimination wurde ebenfalls ein Algorithmus entwickelt.

Mit der Laserscan-Lösung, die in dieser Arbeit vorgestellt wird, konnte bei einer Flughöhe von 500 m über einer Flugpiste eine Höhenmodell-Genauigkeit von 0.3 m realisiert werden. Im Gebirge gestaltet sich aufgrund der höheren Flughöhe über Grund und Turbulenz-Effekten zwischen den Bergen die Realisierung der Datenqualität etwas schwieriger und bewegt sich im Bereich von 0.5 m. Im Testgebiet Unteraargletscher wurden Messungen mit der Laserscan-Technik für temporale Analysen wiederholt realisiert. Für die tiefergelegenen Teile des Unteraargletschers stehen digitale Höhenmodelle aus der Photogrammetrie zum Vergleich zur Verfügung. Für die Messungen der Höhenänderungsverteilung auf dem Gletscher zeigte sich eine Genauigkeit von 0.5–0.7 m als realisierbar.

Als Höhenänderung konnte in den gemessenen Gebieten des Unteraargletschers ein Zuwachs von 2–4 m für die Periode 1998–1999 festgestellt werden. Die Gebiete liegen zwischen 2500 und 3400 m über Meer. Dieser lokale Zuwachs kann mit den heftigen Schneefällen des Winters 98/99 in Verbindung gebracht werden.

Die Abdeckung des Unteraargletschers mit Höhenänderungsmessungen wurde dank der Lasertechnik erstmals bis in die obersten Firngebiete erweitert, und steht für weitere Massenbilanzberechnungen und Fliessmodellierungen zur Verfügung.

# Contents

# List of Figures

# List of Tables

# 1. Introduction

## 1.1. Motivation and Aims of Project

Airborne laser scanning has experienced a rapid increase of interest in the recent years. Naturally, this new method evokes dreams of easier data collection with reduced costs and pain to researchers of environmental sciences such as glaciology. But for a task like estimating surface elevation changes for deriving mass balance thereof, only sparse experiences have been made due to the fact, that most laser scanning activity is focused on urban applications.

Measuring the mass balance of glaciers is important to understand the counteracting of glacier dynamics and climate change. Yet, the determination of mass balance distributions with the traditional method by interpolating results from a number of *in situ* stake measurements is time consuming and is, despite its importance, only made for a small number of glaciers in the world. Alpine glaciers are sensitive to changes in local climate (e.g. Oerlemans, 1994), and may contribute significantly to sea level variations (Meier, 1984; Schwitter and Raymond, 1993). By using remote sensing methods, mass balance cannot be observed directly, but estimates of volume changes are easily feasible. Those estimates can be used to validate calculations of net mass balance based on traditional stake methods (Funk et al., 1997), and to test theoretical concepts about the response of glaciers to changes in climate (Jóhannesson et al., 1989).

Estimates of surface elevation changes may also serve as input data for numerical flow models (Guðmundsson and Bauder, 1999) based on the kinematic boundary condition (Equation 1.2), which is used in conjunction with other remote sensing products to determine the mass balance distribution without resorting to direct field measurements. Therefore necessary accurate Digital Surface Models (DSM) can be generated from aerial photographs only if the glacier displays enough surface texture, which unfortunately is not always the case. In fact, a general lack of texture for snow poses a fundamental difficulty for generating accurate DSMs of accumulation areas. A way out is airborne laser altimetry, which is a promising method for DSM generation of snow-covered areas as it may be used independently of surface texture, external light sources, and control points.

This work assesses the feasibility of the application of airborne laser scanning in mountainous areas for measuring surface elevation changes of glaciers. The test
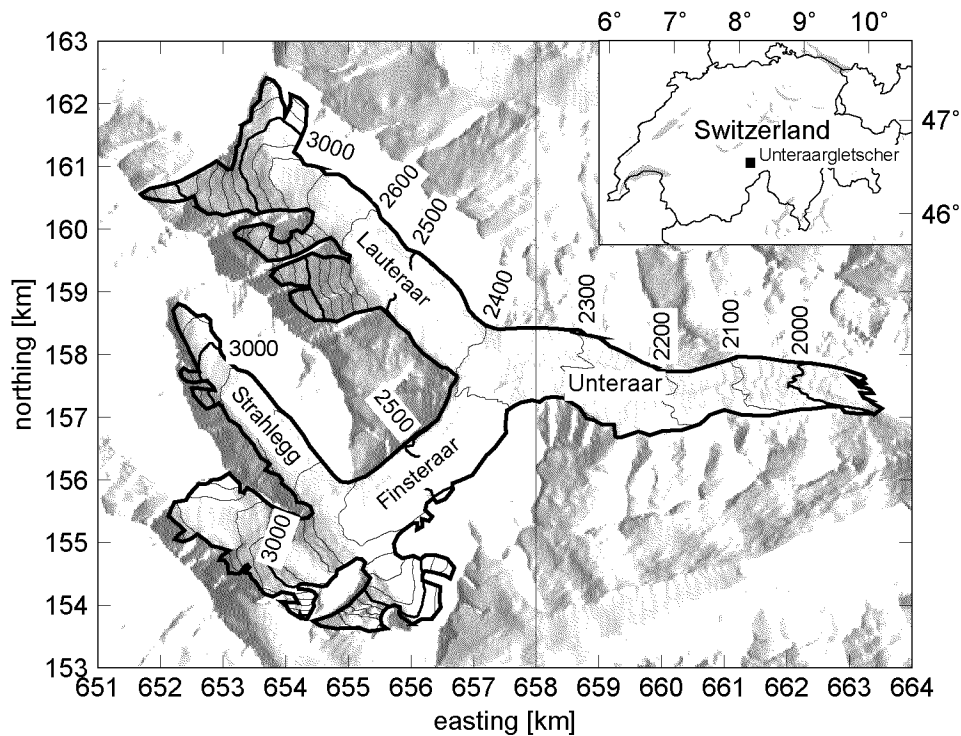
Figure 1.1.: Map of Unteraargletscher. The area to be mapped by airborne laser scanning is the upper part of the glacier to the west of the 658 km line. The glacier boundary is drawn as a bold line. Contour interval: 100 m

data is taken mainly on Unteraargletscher, Bernese Alps, Switzerland (Figure 1.1), where it is used for an already existing numerical flow model by glaciologists. The accumulation zone of the glacier was chosen to extend the existing DSM generated by photogrammetric means. For comparison purposes, one part of the area covered by photogrammetric DSMs was also scanned by the airborne laser system.

Software for georeferencing laser profiling data has already been developed in our institute at an earlier stage. This includes the processing of kinematic GPS data with 'on the fly' ambiguity resolution in the dual frequency mode, as well a some self-calibration approach to calculate bore-sight misalignments directly from laser data for the special case of measuring water surfaces. This was to be extended to a complete direct georeferencing system applicable to any type of laser data. Especially in areas with no known ground truth like remote mountainous regions, the cost and difficulty of establishing ground control points is immense. That is where direct georeferencing of airborne data can be of great help.

## 1.2.   Related Work

### 1.2.1.   Airborne Laser Altimetry

During the last decade Airborne Laser Altimetry (ALA) has matured so that very precise extended digital surface models were obtained operationally with height accuracies better than 20 cm. At present automatic algorithms are under development and partly operational for deriving digital elevation models (DEM) on the basis of ALA-data. Typical laser surveying results reveal that DEMs derived from ALA-data have at least the same accuracy as photogrammetric surveys. Even in forest areas DEMs can be generated (Lindenberger, 1993; Kraus and Pfeifer, 1998), because the number of laser returns from ground are sufficient if the survey is carried out during the winter season. Recognizing these advantages, the group of customers for ALA has been growing rapidly. Various service providers and airborne laser scanning system manufacturers have been established on the market. Manufacturers are e.g. Optech, Toposys and SAAB. In Europe service providers are e.g. Toposys, TopScan and Terra Surveys.

Most airborne laser altimetry activities are concentrated on urban areas as a new tool to quickly generate Digital Surface Models. Remote sensing research focuses currently on automatic object extraction methods in order to recognize and remove houses, trees and other objects in a Digital Surface Model (DSM) to generate a Digital Elevation Model (DEM) (e.g. Maas and Vosselman, 1999; Haala and Brenner, 1999; Axelsson, 2000).

Nevertheless, airborne laser altimetry also experienced increased interest from other science branches such as glaciology. Airborne surface profiling of glaciers has been conducted in North America on a number of glaciers (Echelmeyer et al., 1996; Sapiano et al., 1998; Aðalgeirsdóttir et al., 1998). The accuracy in height of the repeated laser profiling was estimated to be about 0.3 m. DSMs over the Greenland ice sheet with 10–20 cm accuracy in height were measured by NASA using a scanning laser altimeter first by Garvin and Williams (1993) and later by Thomas et al. (1995) and Krabill et al. (1995). Validation was done by either comparing selected points, or by comparing two strips measured by the same system in a perpendicular flight line arrangement at the crossover area (repeatability). Kennett and Eiken (1997) have made laser scanning measurements on a Norwegian glacier with a nominal accuracy in height of 10–20 cm, derived from repeatability and some measurements over an ice-free area.

Airborne laser profiling has been intensively used for Geoid determination in Greece and Switzerland. The principle with a self-calibration technique is described by Geiger et al. (1994). For geoid determination, the laser distance to the sea surface is measured. Since the sea surface height is close to the equipotential surface of the gravity field (discarding currents and wind effects) it is possible to obtain the relief of the gravity equipotential surface by sampling the sea surface height. The self-calibration procedure assumes, that the measured surface is flat, which is almost

true in the case of lakes. Cocard et al. (1997) applied this method to map the surface of the Ionian Sea. Favey and Schlatter (1998) determined the geoid of the Lake of Geneva by both airborne laser altimetry and by conventional methods to serve as reference. Thus a qualitative and quantitative comparison could be made. The geoid determined by laser profiling matches the reference geoid by ±3 cm with a systematic offset of 10 cm.

## 1.2.2. Glaciology

The traditional approach to determine the mass balance distribution is to interpolate results from a number of *in situ* stake measurements (Østrem and Brugman, 1991). This method is not only time consuming, but also prone to errors on the order of the signal to be observed itself (Østrem and Haakensen, 1999). Thus various alternative approaches to measure mass balance with possibly a reduced amount of field work have been suggested and tested. These methods may be divided into two groups, depending on whether it is the spatially averaged annual mass balance (net balance of the whole glacier) or the mass balance distribution that is determined (Guðmundsson and Bauder, 1999).

Estimating net mass balance change requires information on the rate of change in glacier volume. This information can be extracted from maps of different time periods, or from comparing DSMs. In Switzerland, such studies were conducted for the Rhonegletscher (Chen and Funk, 1990) and for Griesgletscher (Funk et al., 1997). Combining the information of old maps and height information measured by airborne laser profiling was done by Sapiano et al. (1998) on nine different glaciers in Alaska. They derive the net mass balance by extrapolating the height difference from old maps along their laser profiles to a volume change of the whole glacier, and then applying assumed ice densities. With the help of an empirical energy-balance model from Oerlemans and Fortuin (1992), conclusions about an average temperature change are drawn.

Most approaches to estimate the mass balance *distribution* are based on the use of the continuity equation:

$$\frac{\partial h}{\partial t} + \nabla \cdot \boldsymbol{q} = \dot{b} \qquad (1.1)$$

where the mass balance rate $\dot{b}$ is determined indirectly from the observed surface elevation changes with time $\partial_t h$ and by estimating the horizontal divergence of the flux vector $\boldsymbol{q}$. Thus, for this method some knowledge about the flow field of the glacier is needed. Examples for the use of this method can be found in Reynaud et al. (1986) and Rasmussen (1988).

Yet another approach is proposed by Guðmundsson and Bauder (1999), which uses estimates of surface elevation changes $\partial_t h$ as input data for a numerical flow model based on the kinematic boundary condition (Equation 1.2). In conjunction with

other remote sensing products, DSM changes are used to determine the mass balance distribution without resorting to direct field measurements. The kinematic boundary condition

$$\frac{\partial h(x,y)}{\partial t} + v_x(x,y)\frac{\partial h(x,y)}{\partial x} + v_y(x,y)\frac{\partial h(x,y)}{\partial y} - v_z(x,y) = \dot{b}(x,y) \qquad (1.2)$$

describes the relation of quantities defined at the glacier surface with the mass balance rate $\dot{b}(x,y)$. The surface slopes $(\partial_x h, \partial_y h)$ and the surface elevation changes $(\partial_t h)$ can be calculated from Digital Surface Models (DSM), which is not the case with the surface velocity $v = (v_x, v_y, v_z)$. Some first results for the lower part of Unteraargletscher are presented in Bauder and Guðmundsson (1996). A detailed description of the method, especially on the calculation of the velocity vector components $v_x$, $v_y$ and $v_z$, is given in Guðmundsson and Bauder (1999).

This work focuses on assessing how well airborne laser scanning can help determine some of the elements on the left hand side of Equation 1.2 for Unteraargletscher. The glacier has been the subject of numerous glaciological studies over the last 150 years. An extensive list of references to glaciological work is listed in Zumbühl and Holzhauser (1988, 1990). Recent studies on Unteraargletscher have focused on the flow properties of the confluence area of the two main tributaries Finsteraar- and Lauteraargletscher (Guðmundsson et al., 1997; Guðmundsson, 1999b), on strain-rate variations during mini-surges (Guðmundsson, 1999a), and on the temporal variations in shearing with depth (Guðmundsson et al., 1999).

## 1.2.3.   GPS and INS for Sensor Orientation

Coalescing GPS and INS for sensor orientation is not a new idea. For example Goldfarb and Schwarz (1985) merge these two systems for airborne positioning purposes. How well GPS and INS can be joined and what kind of trade-offs one has to consider was studied by Lipman (1992). He concludes, that the kind of coupling to be chosen depends on the final user's particular situation and needs. Kerr (1994) studies the use of GPS/INS for georeferencing multi-sensor scanner data. Using GPS aiding for Strapdown INS Orientation using Kalman filtering has been studied to improve the orientation solution (e.g. Škaloud, 1995; Söhne, 1996). A continuation of this approach to optimize the estimation procedure in INS/GPS integration using an adaptive Kalman filter is followed by Mohamed (1999).

Deriving vehicle attitude information from multiple GPS receivers has been tried since the early days of GPS. Most implementations are based on the approach described by e.g. Cohen et al. (1992). One of the first presentation of flight test results, using four antennae on a Douglas DC-3, was given by van Graas and Braasch (1991). Using multiple antennae connected to one single receiver was a widely followed approach (e.g. Santerre and Beutler, 1993); even commercial systems emerged, though they have mostly disappeared today. Trimble Inc. produced a four-antennae GPS receiver called VECTOR designed for attitude determination. Cohen et al. (1992)

find an attitude accuracy of 0.07 degrees ($1\sigma$) for a 3 m baseline using this special hardware. Kinematic tests with Ashtech's 3DF system were made on a truck, using a Litton strapdown INS as reference information (Schwarz et al., 1992). The observed accuracy using 1–2 m baselines was about 0.2–0.5 degrees.

A setup on a Twin Otter aircraft was realized by Cannon and Sun (1996), which is somewhat similar to our implementation presented in Section 4.3. As two of the antennae were installed on the wingtips, Cannon and Sun (1996) model wing flexure along with their attitude solution. The observed agreement between GPS and INS was 0.12 degrees RMS. Their evaluations were made with the software developed at their institute (Lu, 1995). Another approach that makes use of the known antenna geometry to help ambiguity resolution is presented in Euler and Hill (1995). A more general overview on sensor orientation issues is given by Škaloud (1999). His work focuses on filtering and de-noising the INS signal and using INS information to help resolve the GPS ambiguity resolution.

In the past few years, georeferencing methods for airborne laser profiling data for determining water surfaces were developed at our institute (Geiger et al., 1994; Favey and Schlatter, 1998). For profiling, the positioning is solved separately from the aircraft attitude using the kinematic GPS software developed by Cocard (1995). The kinematic GPS algorithms were validated in flight by using photogrammetry (Grün et al., 1993), as well as during various terrestrial campaigns. The positioning solution was also used for airborne gravity surveys (Klingelé et al., 1997) as a source for airborne gravity reduction.

## 1.3. Thesis Outline

In Chapter 2, as a theoretical background, the basic equations and their error analysis of direct georeferencing are presented. An overview of the used laser scanning system is given, with some comments regarding timing, reflectivity on snow and ice, and laser distance blunder detection. The hardware used for realizing the laser scanning measurements is presented.

Chapter 3 presents an extension to existing kinematic GPS software for processing a moving basevector, attached to the aircraft. In a second part, various error effects are studied, which degrade the positioning results of kinematic DGPS trajectory. Mitigation approaches for tropospheric path delay error are discussed, as well as the influence of cycle slips, and satellite loss due to interference or obstruction.

Chapter 4 focuses on a crucial element of direct georeferencing: the sensor attitude determination. A method for calculating the aircraft attitude from an array of multiple GPS antennae is presented. This GPS attitude is used to estimate and correct systematic INS error effects. A comparison between this solution and an independent commercial solution is used to verify the solution's performance.

Chapter 5 treats the determination of the inner orientation parameters lever arms

and boresight misalignment. For the angular misalignment offsets, a self-calibration technique using directly the laser height data is developed. The way irregularly distributed points are gridded to a regular grid is described.

Chapter 6 presents the results of laser scanning on the glacier. A repeatability analysis using the strip overlaps is made. The temporal aspect of generating DSMs by remote sensing to generate surface elevation changes is treated and the glaciological impact is discussed.

In Chapter 7, the results of laser scanning measurements are compared to various sources of 'ground truth', such as terrestrially measured GPS points and photogrammetrically generated DSMs of part of the target glacier's area. The relation between the different geodetic data, in which the laser and the photogrammetric DSM are given, is discussed.

Chapter 8 draws conclusions from the research work conducted and also gives recommendations for future investigations.

Some of the material presented in this work has been either previously published or submitted for publishing. In those cases where the candidate has been either the author or the first co-author of these papers, quotations are not indicated as such, but the work is simply referenced.

# 2. Airborne Laser Scanning Technique

## 2.1. Introduction

The goal of airborne laser scanning is to produce a DSM by measuring the absolute surface elevations. Using a laser beam, the distance from the aircraft to the ground is measured as

$$r = \frac{1}{2}ct \qquad (2.1)$$

where $t$ is the traveling time of the laser signal, and $c$ is the speed of light. The aircraft position can be determined through the use of differential GPS carrier phase positioning with an accuracy of a few centimeters (e.g. Krabill and Martin, 1987; Cocard, 1995; Seeber, 1993). This positioning capability, when combined with the attitude of the moving platform, serves to reconstruct the full vector of the GPS antenna to the ground (e.g. Geiger et al., 1994; Vaughn et al., 1996). The ground point is then calculated by vector additions and rotations, as described in the last section of this chapter.

The laser scanning was realized in cooperation with the Institute of Navigation, University of Stuttgart, using the ScaLARS II laser scanner they developed (Hug, 1996). After describing the specialties of this laser scanner hardware, the instrument setup and specifications used for generating the laser data are given in detail.

## 2.2. Distance Measurement with Laser Light

### 2.2.1. Distance Measurement with the c/w Technique

The continuous wave technique of measuring ranges is based on determining the time $t_L$ a modulated signal needs to travel to the target and back. Wehr and Lohr (1999) give a detailed overview of this technique, of which a short summary is cited hereafter. As the period $T$ of the signal is known, the traveling time $t_L$ is directly

proportional to the phase difference $\phi$ between the received and the transmitted signal. Thus $t_L$ is calculated by

$$t_L = \frac{\phi}{2\pi}T + nT \tag{2.2}$$

where $n$ is the number of full wavelengths included in the distance from the laser transceiver to receiver. Related to the modulation signal frequency, $t_L$ can be written as

$$t_L = \frac{\phi}{2\pi}\frac{1}{f} + \frac{n}{f} \tag{2.3}$$

If the phase difference $\phi$ is measured, the range is

$$R = \frac{c}{4\pi f}\phi + \frac{nc}{2f} \tag{2.4}$$

and the range resolution is therefore

$$\Delta R = \frac{1}{4\pi}\frac{c}{f}\Delta\phi \tag{2.5}$$

Thus, the range resolution can be increased (lower $\Delta R$) by using a higher frequency $f$ for a given phase resolution $\Delta\phi$. The ranging accuracy is additionally related to the signal to noise ratio (Hug, 1996), whose square root is proportional the received optical power $P_R$, as well as to the noise input bandwidth $B$, which is proportional to the measurement rate.

$$\sigma_R \sim \frac{\lambda}{4\pi}\frac{\sqrt{B}}{P_R} \tag{2.6}$$

As ScaLARS II uses two modulation frequencies of 1 and 10 MHz, the 10 MHz determines the range resolution and accuracy, whereas the 1 MHz determines the maximum unambiguous range

$$R_{\max} = \frac{c}{4\pi f}\phi_{\max} = \frac{\lambda}{2} \tag{2.7}$$

Thus the longest unambiguous range, that this laser system can determine is about 70 m, which can pose problems in the steep cliffs adjacent to the glacier and on steep parts on the glacier itself.

The problems due to ambiguity resolution are discussed in detail in Section 2.2.4.

## 2.2.2.  Laser range calibration and refraction correction

The laser range calibration was done by the University of Stuttgart by measuring a true reference range with the laser equipment. The reference range $s$ was measured by differential GPS/INS (Thomas, 2000).

The laser range correction to be applied to the measured range $l_m$ was modeled as

$$s \doteq l_c = l_m + f(r) + f(b) \tag{2.8}$$

where $s$ stands for the true range and $l_c$ for the corrected measurement. The first correction $f(r)$ is related to crosstalk effects of the c/w measuring technique, where $r \sim \frac{l_m - s}{s}$. $f(b)$ is a correction of $l_m$ dependent on the received laser power $b$.

The atmospheric correction due to the meteorological conditions prevailing at the scene of calibration is intrinsic to the modeling functions $f(r)$ and $f(b)$. Thus a remaining refraction correction to the vertical airborne laser measurements is modeled by combining Equations B.5 and B.6 (cf. Appendix B).

Let $k$ be the correction factor, the meteocorrected vertical range in the air $l_a$ may be modeled as:

$$l_a = k \cdot l_c \tag{2.9}$$

with

$$k = \frac{2n_0}{n_a + n_g} \tag{2.10}$$

where

$n_0$  :  refraction index, that was valid for the horizontal calibration measurement
$n_a$  :  refraction index at the airplane
$n_g$  :  refraction index on the ground at the glacier

To get an estimation for the magnitude of this effect, a typical setting for the glacier is taken. Using the equations in Appendix B.1, $n_0(400\,\text{m})$, $n_a(3500\,\text{m})$, and $n_g(2500\,\text{m})$ are calculated and inserted inserted into Equation 2.10. The resulting factor $k = 1.000060$ shows, that the remaining correction due to different atmospheric conditions at the different scenes of range distance measurement is on the order of $6\,\text{cm/km}$.

A first test flight over the glacier area were undertaken in August 1997. During this campaign, several problems occurred, which made the data quality to be worse than $1\,\text{m}$ (Favey et al., 1999). Based on these experiences, the laser scanning hardware was improved by the Institute of Navigation, University of Stuttgart. The time digitization unit built into the laser scanning device needed to be replaced, as it was not functioning properly. The crosstalk correction needed to be revised. The laser power was upgraded in order to reach longer distances.
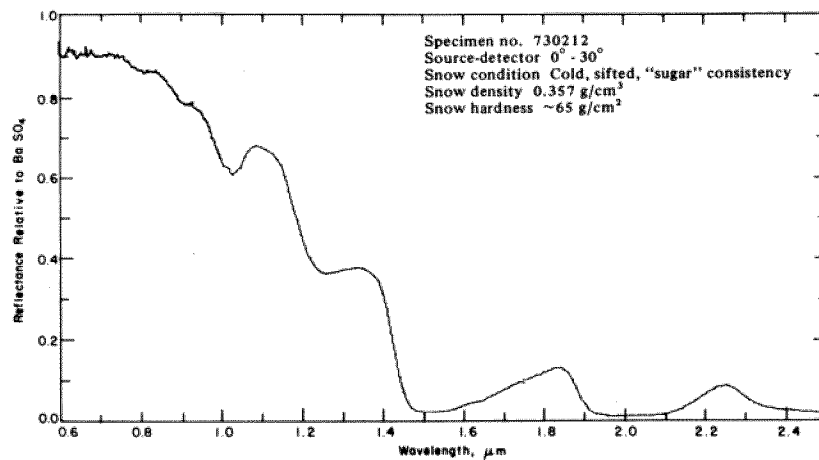
Figure 2.1.: Typical reflectance properties of snow and ice in relation to the wave-length (from O'Brien and Munis, 1975). Note the very good reflectance of light at 810 nm and the decrease of reflectance with higher wave-lengths.

## 2.2.3.  Albedo of Snow and Ice for the Laser Wavelength

O'Brien and Munis (1975) have studied the reflectance properties of snow with varying conditions. The reflectance of snow respective to the laser light wavelength is shown in Figure 2.1. The laser light of 0.81 $\mu$m the ScaLARS II system uses is close to visible light and has very good reflectance properties even on old and refrozen snow, as opposed to a wavelength of 1.5 $\mu$m, where snow appears to be almost black.

Depth of insertion into snow at a wavelength close to visible light is according to Gubler (1998) less than 1 cm, and thus was not further investigated. Snow and glacier ice are a nearly perfect diffuse reflector.

## 2.2.4.  Blunder Detection and Removal

The laser scanning system ScaLARS uses the continuous wave technique for mea-suring distances. The count of full wavelengths $n$ in Equation 2.4 is an ambiguous value. It has to be solved for each modulated frequency. According to Equation 2.7, the ambiguity for the longest wavelength has to be determined with a priori knowledge of the terrain with an accuracy of $\lambda/2 \approx 75$ m for the longest wavelength.

If the terrain is slowly changing like in a flat area or with rolling hills, this ambiguity can easily be initialized by using the flying height above ground given as GPS altitude minus ground height read from a map. During the rest of the strip, the phase stays locked and the distances can be determined without problems.

In an alpine environment, distance changes over more than 150 m can occur within one single scan mirror rotation due to step cliffs. A loss of phase lock can also occur

if the reflected signal intensity is very low. If the ambiguity is determined from the previously measured distances, it may easily be fixed to a wrong value, as the terrain may have changed over more than 70 m.

There exists a DHM covering all of Switzerland with a 25 m grid spacing and an accuracy of 10–20 m. It is called DHM25 and was produced from topographic maps by the Swiss Federal Office of Topography. This DHM was used to address the problem of the long wavelength ambiguity fixing. Each calculated ground point height is compared with a reference height derived from the DHM25 by bilinear interpolation. If the difference is greater than 70 m, the slant range is corrected by one wavelength and the newly calculated ground point compared again. This way, the long wavelength can always be determined correctly.

Even if the longest wavelength ambiguity could be correctly resolved, the shorter wavelength ambiguity sometimes cannot be derived correctly. A comparison with known ground truth revealed an increased blunder probability with low reflectance intensity (cf. Section 7.2.3, page 119). This problem was already noted by Hug (1996) during the development of the ScaLARS II instrument. Introducing an intensity threshold is not satisfactory, as too much (about 10%) of the good data would be incorrectly eliminated as blunder.

This problem was addressed using a simple blunder detection algorithm. Given a georeferenced laser point coordinate $x_k = (x_k, y_k, z_k)^T$, a corresponding height is interpolated from the surrounding laser data points $x_i$ located at a distance $\rho_i = \sqrt{(x_i - x_k)^2 + (y_i - y_k)^2}$, and the difference $dh$ is built:

$$dh = z_k - \frac{\sum\limits_{i \neq k} w_i(\rho_i) \cdot z_i}{\sum\limits_{i \neq k} w_i(\rho_i)} \tag{2.11}$$

where $w_i(\rho_i)$ is a weight function given as:

$$w_i = \frac{\varepsilon^n}{\rho_i^n + \varepsilon^n} \tag{2.12}$$

The characteristics of the weighting function are described in detail in Section 5.4. For the special purpose blunder detection, the correlation length $\varepsilon$ is chosen long enough to include about 5–10 neighboring measurements, where as an exponent $n = 6$ is chosen in order to have multiple nearest neighbors equally weighted. Figure 2.2 shows the chosen form of the weight function used for blunder detection.

This way an outlier can still be detected, even if another of the contributing points $x_i$ is blunder as well, because the other points in the domain will draw the interpolated height towards the correct ground position. If

$$|dh| > \Delta h_{\max} \tag{2.13}$$
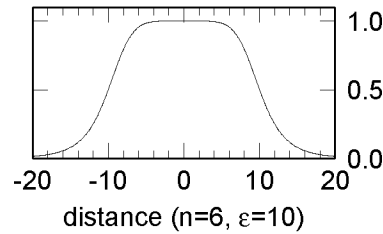
Figure 2.2.: Form of the weight function $w(n, \varepsilon)$ versus the distance $\rho$.

the point $k$ is rejected as blunder.

The threshold $\Delta h_{\max}$ depends mainly on the wavelength $\lambda_2$ of the high modulation frequency. Using the height accuracy of the final ground point $\sigma_{x_3}$ from Equation 2.27, we can write a criterion for choosing $\Delta h_{\max}$:

$$3 \cdot \sigma_{x_3} < \Delta h_{\max} \leq \frac{\lambda_2}{2} \tag{2.14}$$

The studied laser data shows a very characteristic distribution around $N\lambda_2$ values (Table 7.3) with about 5–10% of all data being blunder. The percentage is strongly depending on the reflectance intensity. If blunder should be detected also in darker parts where points with a wrong ambiguity $N$ appear with increased probability close together, (yet not necessarily with the same sign of $N$,) it is advisable to use an $\Delta h_{\max}$ closer to $\frac{\lambda_2}{2}$ than to $3 \cdot \sigma_{x_3}$. The smaller the threshold is set, the more likely good data is discarded because it is noisy due to rough terrain. The closer it is to $\frac{\lambda_2}{2}$, the more robust it is against a local accumulation of blunder.

Small features like thin crevasses or small rocks of the size of $\lambda$ are likely to be eliminated as blunder as well. On the other hand, large features such as cliffs or step-like terrain will not be eliminated if more than half of the contributing points to the interpolation are situated on the feature.

## 2.3.  Instrument Setup and Specifications

### 2.3.1.  The Aircraft

All of the three laser scanner flights were performed with a slightly varying instrument setup, especially with systems that were improved and thus changed over the years.

The flights were performed with a DeHavilland DHC-6 Twin Otter aircraft (Fig. 2.3) owned by the Swiss Federal Office of Topography (L+T) and operated by pilots of the Swiss Air Force. The aircraft is equipped with two fully operational RC30 aerial cameras and the Aerial Survey Control Tool (ASCOT) navigation system by

LH-Systems. To mount the laser scanning system, the aerial camera just behind the cockpit was unmounted. The laser scanner system was mounted instead to fit its field of view optimally through the opening of the aircraft floor. The aircraft is also equipped with a Collins AP-106 flight control system and FD 112-C flight director.



Figure 2.3.: The DeHavilland DHC-6 Twin Otter

## 2.3.2.   GPS receivers

The aircraft was equipped with up to seven GPS receivers operating at sampling rates between 1 Hz and 4 Hz (Table 2.1). Four single frequency antennae were installed on the wings, the tail, and the fuselage. Additionally, three dual frequency antennae were installed distributed along the fuselage (Figure 2.4).

The single frequency receivers were operated on a higher frequency to use the denser information for GPS attitude determination. The REAR receiver was used for trajectory recovery as well as for attitude determination on all flights. The FWDB antenna was only used to provide the Applanix System with a GPS antenna during the 1999 flight.

Additional data was collected by the Leica GPS receiver, which is used for the ASCOT navigation system. An AM differential signal radio receiver providing differential GPS carrier phase corrections was connected to the ASCOT system to ensure an optimal realization of the planned flight lines. The navigation part was operated entirely independently of the laser scanning and data logging facilities.
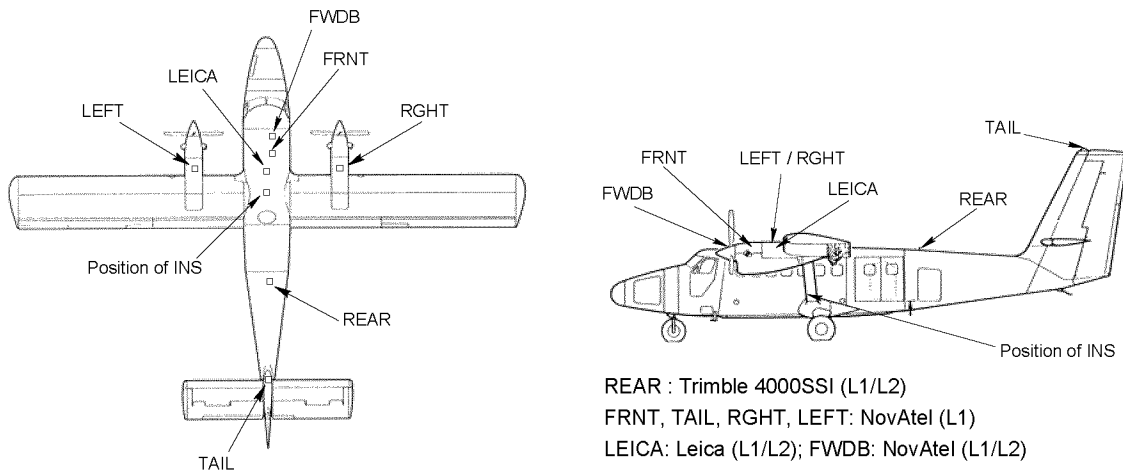
Figure 2.4.: Distribution of GPS antennae on the DeHavilland Twin Otter. The location of the strapdown INS system is marked as well.

| ID | receiver type | frequency | operated at |
|---|---|---|---|
| REAR | Trimble 4000 SSI | dual | 2 Hz, 1997–99 |
| LEICA | Leica SR9500 | dual | 1 Hz, used for ASCOT navigation system |
| FWDB | NovAtel GPSCard | dual | 1 Hz, 1999 only, for Applanix system |
| FRNT | NovAtel GPSCard | single | 4 Hz, 1998–99 |
| TAIL | NovAtel GPSCard | single | 4 Hz, 1998–99 |
| LEFT | NovAtel GPSCard | single | 4 Hz, 1998–99 |
| RGHT | NovAtel GPSCard | single | 4 Hz, 1998–99 |

Table 2.1.: Airborne GPS receivers and antennae

Two industrial personal computers (INPC) were used to log the data of the four NovAtel receivers, each computer taking care of two receivers. A third INPC was used to log the data of the strapdown inertial system of iMAR (See Figure 2.9).

## 2.3.3.  Gyro Platform and Strapdown INS Systems

Three different inertial measurement units (IMU) were used, as the newer systems becoming available performed with better accuracy than the preceding systems. The first system used to determine the aircraft attitude was a Sperry Gyro platform, formerly build into an air force fighter and later adapted for civilian use to acquire attitude measurements. This system provides directly the attitude angles with a resolution of 0.001°. It suffers from drift effects, and was used only during the 1997 test campaign.
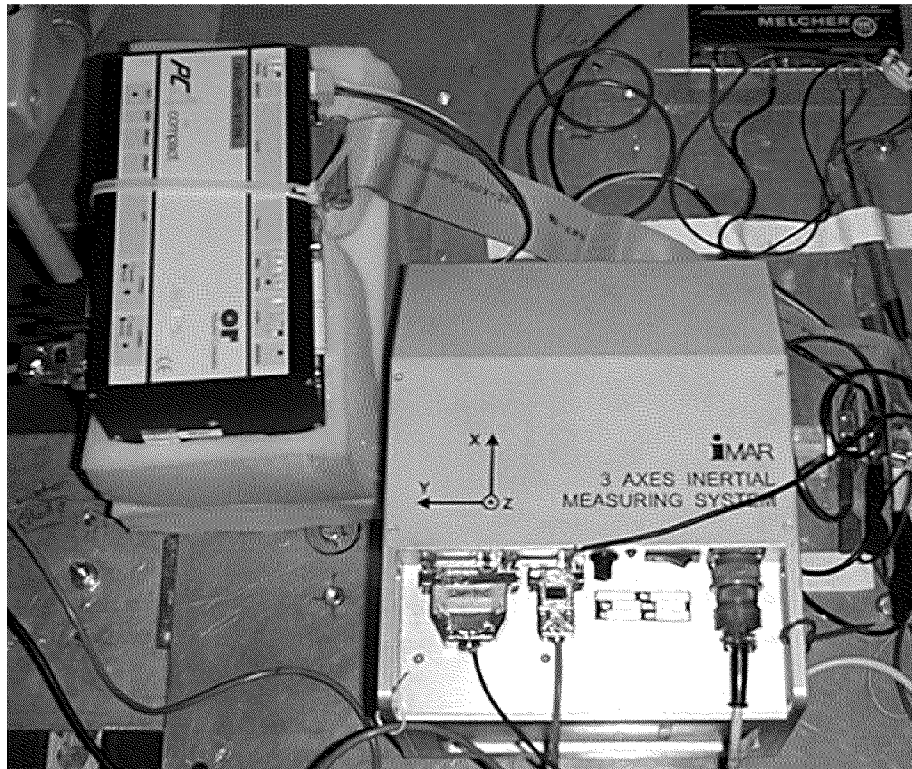


Figure 2.5.: Inertial System of iMAR installed on the aircraft floor. The industrial PC to the left was used to control the unit and to log the data.

During the two main campaigns of 1998 and 1999, a strapdown IMU of iMAR GmbH was used. It operates at a measuring frequency of 100 Hz, and provides an angular resolution of 0.001°. It uses shock-resistant closed loop fiber optical gyros (FOG) and three accelerometers arranged in perpendicular axes. The system uses an initial alignment performed before every survey to determine its orientation with respect to

the earth. For this purpose the gravity vector (local vertical) and the earth's rotation axis (true north direction) are determined. After this initialization procedure, the raw measurements are merely logged. Some aiding capabilities are build into the post-processing software provided by the manufacturer to use the gravity vector to minimize roll and pitch drift effects. Yet these aiding capabilities were not used, as they showed swaying effects superimposed by the filtering. To estimate the drift and offset, an approach using the lower accuracy GPS attitude as stabilizing reference is presented in Chapter 4.
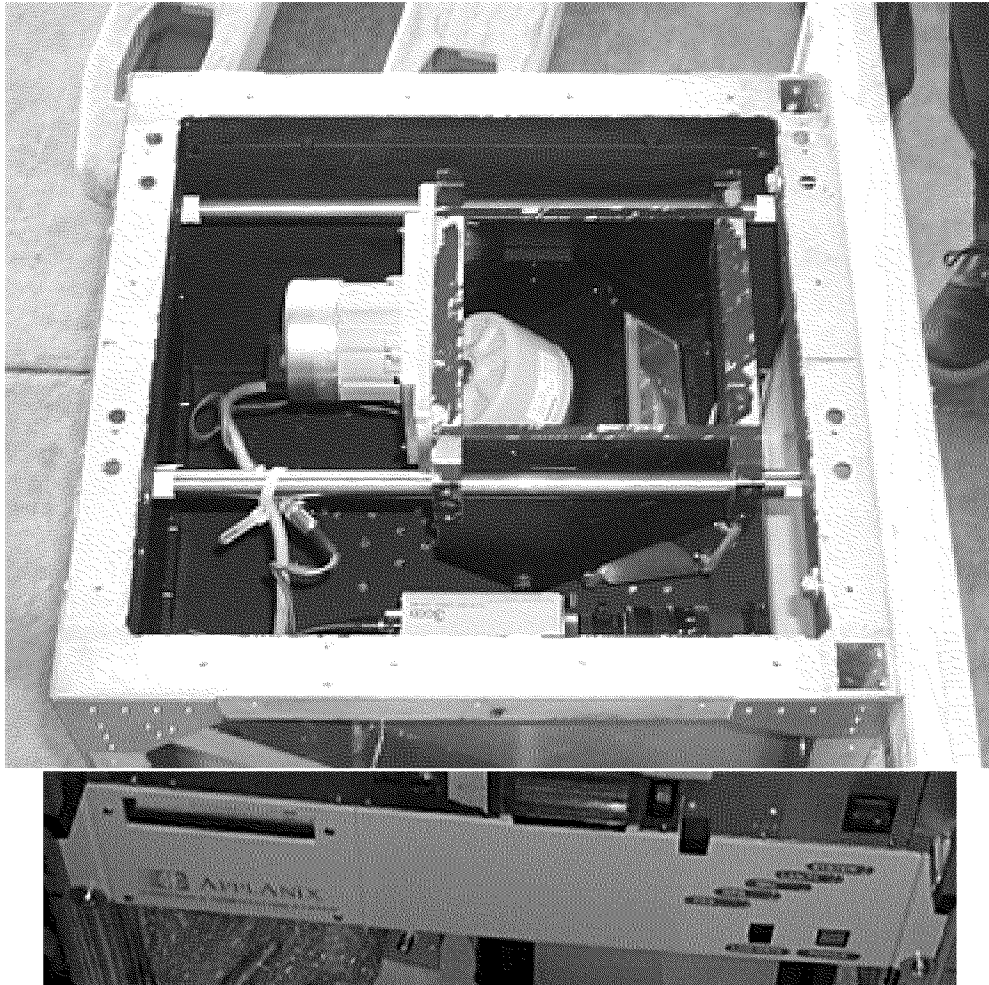


Figure 2.6.: Inertial System of Applanix. The top image shows the IMU mounted on top of the yellow laser scanning mirror motor. The bottom image shows the Applanix control unit mounted in a rack.

A third IMU of Applanix Corp., POS AV 310, was used during the 1999 campaign. It operates at a measuring frequency of up to 200 Hz, and provides an angular accuracy of 0.013° RMS for roll and pitch, and 0.035° RMS for heading (manufacturer's product specification). This system was used along with the iMAR system to vali-

date the attitude solution approach presented in this work.

## 2.3.4.   Laser Scanning System ScaLARS II
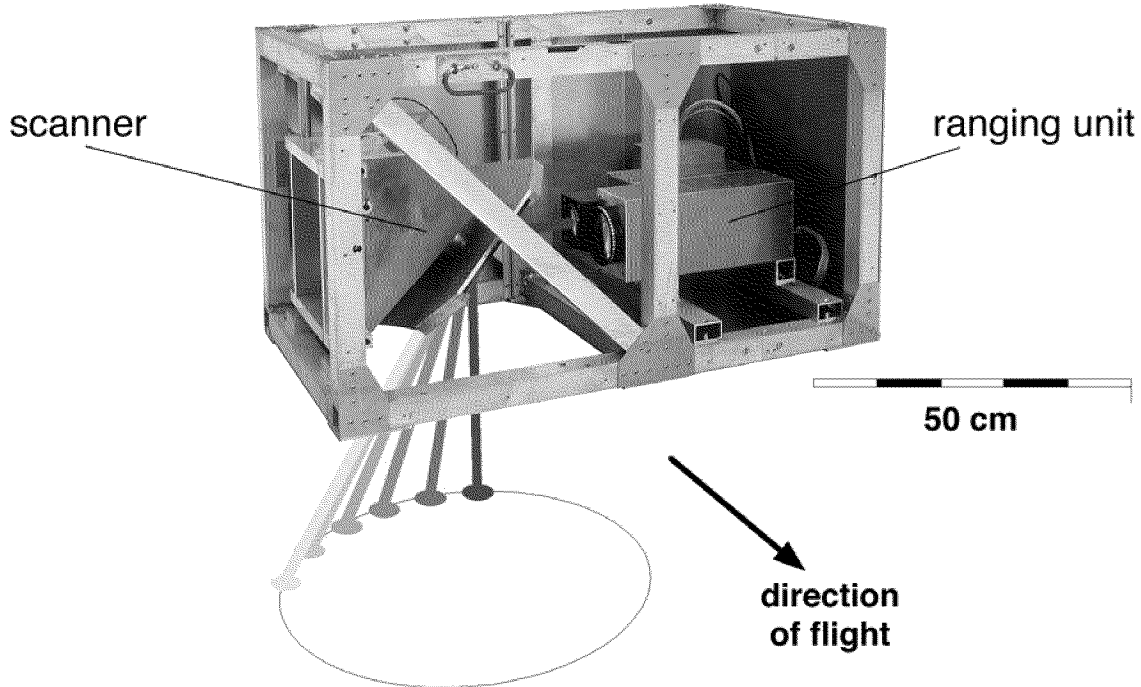


Figure 2.7.: The ScaLARS II laser scanner built by the Institute of Navigation, University of Stuttgart (Graph by A. Wehr, Univ. Stuttgart). The laser scanning hardware was flown in anti-parallel direction than shown in this graph, as the system would not fit into the airplane the other way around.

The laser scanning system used during all flights was ScaLARS II, developed by the Institute of Navigation, University of Stuttgart. Opposed to most other airborne laser systems using light pulses, it uses a range measuring technique called continuous wave (c/w) modulation (Hug, 1996).

The laser transmits a continuous signal. Ranging is carried out by modulating the light intensity of the laser light with two sinusoidal signals, which are received with a time delay corresponding to the length of the traveled path. The technique is described in more detail in Section 2.2.

ScaLARS II uses a nutating mirror (Palmer scan mechanism, Figure 2.8) to produce an elliptical scan pattern on the ground. The laser system was initially designed to operate at a flying height of 150–450 m above ground (Hug, 1996). It was later enhanced to measure up to 750 m.
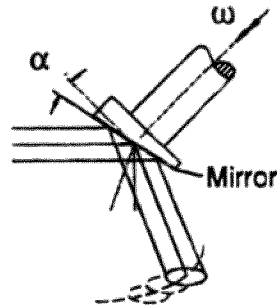
Figure 2.8.: Scanning mechanism: Palmer scan (from Wehr and Lohr, 1999). $\omega$ stands for the angle of mirror rotation; it is digitized to reproduce the scanning geometry. $\alpha$ is the angle of the true mirror plane to the mirror axis normal.

| wavelength | 810 nm |
|---|---|
| beam divergence | 2 mrad |
| measuring range ($\rho = 20\%$ ) | 750 m |
| scan rate | $\leq$ 20 Hz |
| footprint on ground | $\approx$ 2 m |
| point spacing | $\approx$ 2 m |
| measurement rate | 7.5 kHz |
| swath width ($h = 700$ m) | 338 m |
| uncertainty in slant range | 0.12 m |
| modulation c/w-sinusoidal | 10 MHz, 1 MHz |
| scanning angle in flight direction | $\pm$ 9.7° |
| scanning angle perpendicular to flight direction | $\pm$ 13.6° |
| measuring ground reflectivity | yes |

Table 2.2.: Important laser system parameters

The modulation frequencies of 1 and 10 MHz introduce a range ambiguity of 149.85 and 14.985 m respectively. Thus, if the phase shift on both frequencies can successfully be measured, an initial ambiguity of <75 m must be determined by other means using e.g. maps or existing DEMs (Equation 2.7).

The swath width $w$ can be determined for a given flying height above ground $h$ as:

$$w = 2h \tan \frac{\alpha}{2} \qquad (2.15)$$

where $\alpha$ is the scanning angle perpendicular to the flight direction.

An overview of the laser system parameters is given in Table 2.2.

## 2.3.5. Data Recording Hardware and Flight Setup
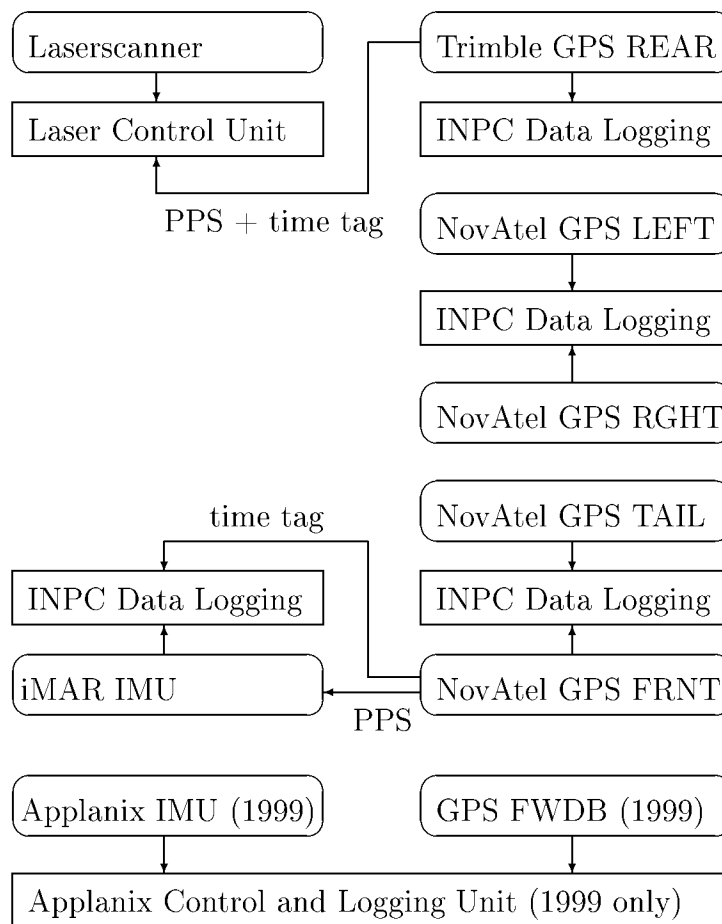


Figure 2.9.: Data recording equipment and instrument setup for the test flights 1998 and 1999

In-flight data recording was realized using several industrial personal computers (INPC) mounted in a rack. As the entire rack was suspended on shock-mounts,

the INPCs did not suffer from vibration during data recording. Figure 2.9 shows the data recording setup for the flights of 1998 and 1999. Figure 2.10 shows all the components mounted in the Twin Otter.
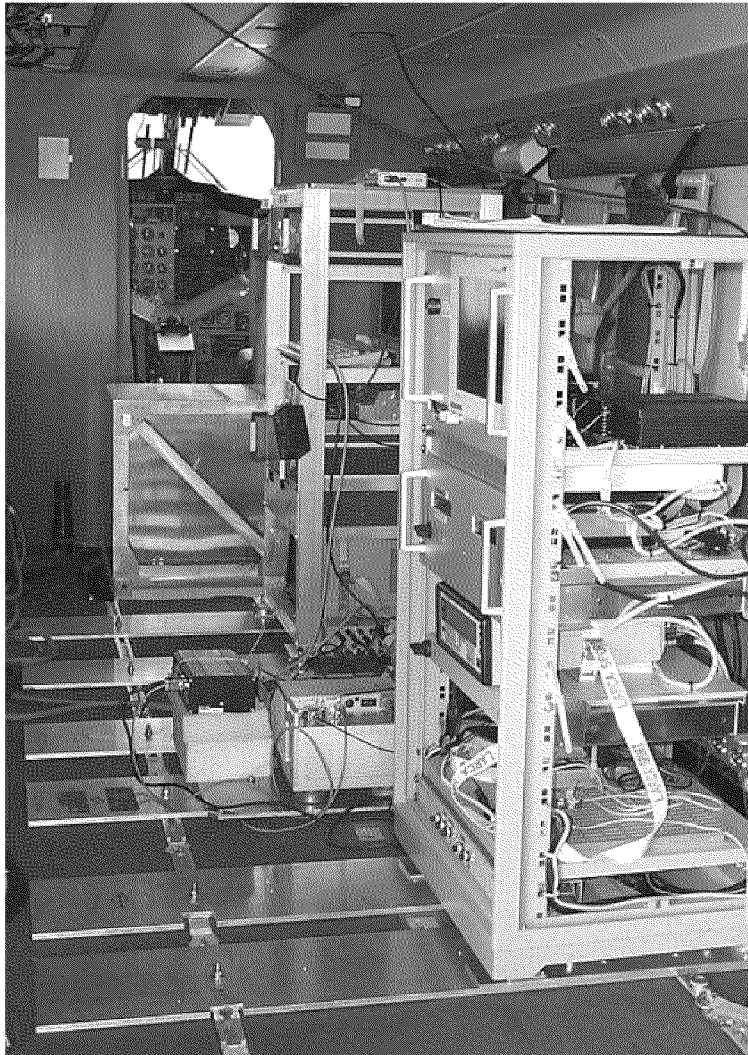


Figure 2.10.: Laser data equipment ready for takeoff.

## 2.3.6. Laser Scanning Data Processing Overview

The laser scanner raw data itself was preprocessed by the Institute of Navigation, University of Stuttgart. They calculated the slant range, the direction of the laser beam in the laser body frame, the received signal intensity, and the corresponding time already synchronized to GPS time.

Figure 2.11 shows an overview of the subsequent calculation steps realized as part of this work. The positioning and attitude data is first calculated on its own. Then

**Laser**　　　　　　**Positioning**　　　　　　　**Attitude**

GPS　　　　　　　INS

| | | |
|---|---|---|
| raw laser data | GPS double freq<br>1 recv. on aircraft<br>1 ground reference<br>IGS prec. ephem. | GPS single freq<br>4 recv. on aircraft<br>IGS prec. ephem. |

inertial system
raw data

| | | |
|---|---|---|
| calculation of slant<br>range and direction<br>(Section 2.2) | kinematic DGPS<br>trajectory solution | for each receiver<br>kinematic solution with<br>trajectory as reference<br>(Section 3.2) |

preprocessing
and integration
of raw data

attitude angle solution
from GPS
(Section 4.3)

inertial system
attitude angle
solution

time synchronized
merging to calculate
ground point

corrected attitude angles
cleaned of gyro drift
(Section 4.4)

correction of 150m ambiguity
15m blunder detection and
removal (Sections 2.2.4, 7.2.3)

geodetic datum transformation
projection system and geoid
undulation (Section 7.1)

calibration of boresight mis-
alignment angles (Section 5.3)

interpolate to regular grid
(Section 5.4)

georeferencing laser
scanning data (Section 2.5)

volumetric calculation with
grids from different epochs
(Section 6.3)

Figure 2.11.: Data flow and processing steps for evaluating laser scanning data.

the elements are time-synchronized and merged into one single data file, which is used as input to the blunder detection, the self-calibration and the georeferencing algorithms.

At this point, each single laser distance measurement is available forming an irregularly distributed cloud of points. Interpolation for comparison and visualization is done directly from these irregularly distributed points as needed.

## 2.4. Time Synchronization

As laser scanning involves coalescing the data of several decentralized measurement and logging units, an improper time synchronization will be a serious source of errors. Looking at Equation 2.16 for direct georeferencing, errors in the synchronization directly affect the location and orientation of the laser beam.

Assume a 1 ms synchronization error jeopardizing the data. The along-track position error is then about 7 cm, when assuming an aircraft velocity of 70 m/s (which corresponds to the cruising speed during the laser scan flights). As the laser unit uses a palmer scanner with a mirror rate of 20 revolutions per second, the assumed delay would cause a yaw angle bias on the order of 7°. Considering INS data, a 1 ms delay would cause an angular error of 0.01° assuming a vehicle rotation rate of 10° per second. Thus it becomes evident that the time synchronization must be at least at the level of a few microseconds to ensure proper geolocation of the laser data.

The time synchronization between the systems was realized using a PPS (pulse per second) signal generated by the GPS receiver on every full second of UTC. These pulses are logged along with a time internal to the logging system, which allows to establish the relation between the internal and the GPS time frame. Figure 2.9 (page 21) shows how the systems were connected to each other.

Analyzing the time synchronization performance of a GPS receiver's PPS output and event marker registration, Danuser (1992) found the PPS of two receivers tested to be accurate with $1\,\mu s$, which complies with the manufacturer's specification. The event marker registration was found to have an accuracy of $0.1\,\mu s$ exceeding even its specification.

This performance can be jeopardized by hardware dependent delays due to transmission and processing. The readings of the PPS pulses have to be registered within the logging hard- and software immediately upon arrival, which is usually realized by low level coding of the data logging routines using a real time clock. The relation of the internal logging clock with UTC can then be established by modelling the internal clock drift behavior using polynomials.

## 2.5. Processing of Airborne Laser Scanning Data

## 2.5.1.  Direct Georeferencing Basic Equations

Apart from using a laser beam to measure the distance from the aircraft to the ground, the aircraft position and attitude are needed to be able to georeference the measurement. The aircraft position is determined through the use of differential GPS carrier phase positioning. This positioning capability, when combined with the attitude of the moving platform, defines a local-level reference frame.

Within this frame, the distance to the ground is measured by a laser signal sent out at time $t_s$ and received later at time $t_r$. The traveling time $t = t_r - t_s$ is directly proportional to the distance $r$ from the aircraft to the ground (Equation 2.1).

The direction $s$ of the laser beam is determined by the position of the scanning mirror and the known geometrical design of the laser beam's and mirror's position.
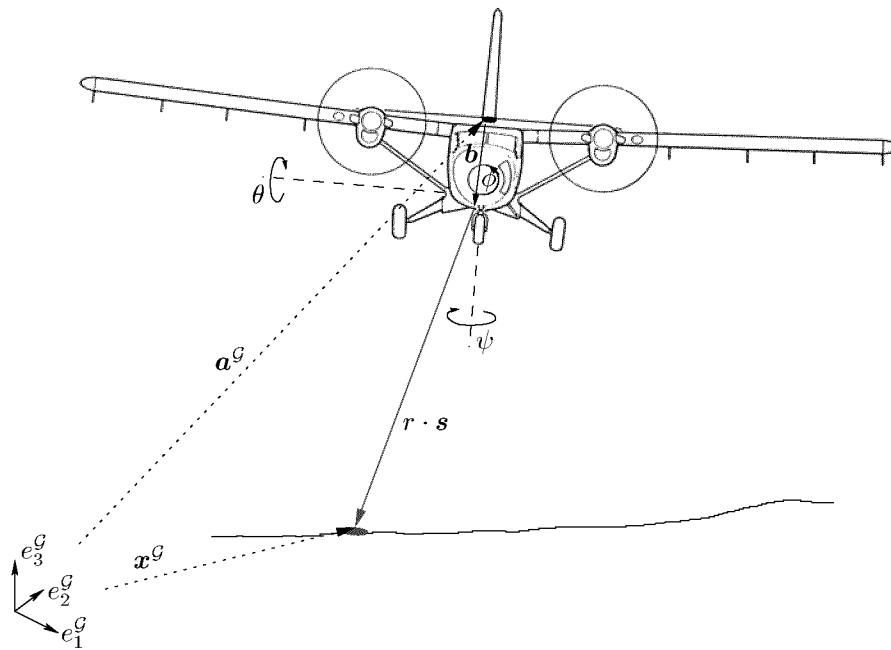


Figure 2.12.: Principle of airborne laser scanning

All those elements put together lead to the observation equation for airborne laser altimetry:

$$x^{\mathcal{G}} = a^{\mathcal{G}} + R_{\mathcal{G}/\mathcal{L}} R_{\mathcal{L}/\mathcal{B}} \left( R_{\mathcal{B}/\mathcal{S}} \cdot r s^{\mathcal{S}} + b^{\mathcal{B}} \right) \qquad (2.16)$$

where

$x^{\mathcal{G}}$    :   Position of ground point to be determined
$a^{\mathcal{G}}$    :   Position of GPS antenna

$R_{\mathcal{G}/\mathcal{L}}$  :  Rotation matrix from local level to geocentric system

$R_{\mathcal{L}/\mathcal{B}}$  :  Rotation matrix between body and local level frame

$R_{\mathcal{B}/\mathcal{S}}$  :  Misalignment rotation matrix between scanner and body frame consisting of the angles $\boldsymbol{\alpha} = (\alpha_1, \alpha_2, \alpha_3)^T$ (cf. Equation 2.19).

$r$  :  Slant range measured by laser device

$s^{\mathcal{S}}$  :  Direction of laser beam pointing in the scanner coordinate frame.

$b^{\mathcal{B}}$  :  Lever arm baseline between scanner point of reference and GPS antenna phase center

Using the position of the GPS antenna, we may write:

$$R_{\mathcal{G}/\mathcal{L}} = R_3(-\lambda) \cdot R_2\left(\varphi + \frac{\pi}{2}\right) \tag{2.17}$$

where $\lambda$ and $\varphi$ are longitude and latitude, respectively. The rotation from the body frame to the local level frame is done with the attitude angles roll ($\phi$), pitch ($\theta$) and yaw ($\psi$).

$$R_{\mathcal{L}/\mathcal{B}} = R_3(-\psi) \cdot R_2(-\theta) \cdot R_1(-\phi) \tag{2.18}$$

The remaining boresight misalignment rotation is unknown and represents the calibration to be determined.

$$R_{\mathcal{B}/\mathcal{S}} = R_3(-\alpha_3) \cdot R_2(-\alpha_2) \cdot R_1(-\alpha_1) \tag{2.19}$$

A detailed discussion about the coordinate frames involved is given in Section 4.2.1.

## 2.5.2.  Error propagation of observables onto ground point position

As Equation 2.16 shows, errors in the contributing measurement systems propagate differently to the final ground point coordinates $x^{\mathcal{G}}$. Their proper time synchronization is also a crucial issue dealt with separately in Section 2.4. If Equation 2.16 is transformed to the local level frame ($\mathcal{L}$) and differentiated, we get

$$dx^{\mathcal{L}} = \frac{\partial\left(R_{\mathcal{L}/\mathcal{G}}a^{\mathcal{G}}\right)}{\partial a^{\mathcal{L}}}da^{\mathcal{L}} + \frac{\partial\left(R_{\mathcal{L}/\mathcal{B}}l^{\mathcal{B}}\right)}{\partial l^{\mathcal{B}}}dl^{\mathcal{B}} + \frac{\partial\left(R_{\mathcal{L}/\mathcal{B}}l^{\mathcal{B}}\right)}{\partial \vartheta}d\vartheta \tag{2.20}$$

where

$$l^{\mathcal{B}} = \left(R_{\mathcal{B}/\mathcal{S}} \cdot r s^{\mathcal{S}} + b^{\mathcal{B}}\right)$$

and $\partial\vartheta$ means the derivation to the attitude angles $\vartheta^T = (\phi\ \theta\ \psi)$. The derivation of $l^{\mathcal{B}}$ includes the laser system performance and the influence from the elements of the sensor orientation within the aircraft. Using the approximation for $\partial_\vartheta$ as described in Appendix A.1, Equation 2.20 can be written as

$$dx^{\mathcal{L}} = da^{\mathcal{L}} + R_{\mathcal{L}/\mathcal{B}}dl^{\mathcal{B}} + R_{\mathcal{L}/\mathcal{B}}L^{\mathcal{B}}d\vartheta \tag{2.21}$$

where $\boldsymbol{L}^{\mathcal{B}}$ is a skew symmetric matrix containing the elements of $\boldsymbol{l}^{\mathcal{B}}$ analogous to Equation A.8 (page 156). If the elements in $\boldsymbol{l}^{\mathcal{B}}$ are separately looked at, Equation 2.21 becomes:

$$d\boldsymbol{x}^{\mathcal{L}} = d\boldsymbol{a}^{\mathcal{L}} + \boldsymbol{R}_{\mathcal{L}/\mathcal{B}}d\boldsymbol{b}^{\mathcal{B}} + \boldsymbol{R}_{\mathcal{L}/\mathcal{B}}\boldsymbol{R}_{\mathcal{B}/\mathcal{S}}d\boldsymbol{r}^{\mathcal{S}} + \boldsymbol{R}_{\mathcal{L}/\mathcal{B}}r\boldsymbol{S}^{\mathcal{S}}d\boldsymbol{\alpha} + \boldsymbol{R}_{\mathcal{L}/\mathcal{B}}\boldsymbol{L}^{\mathcal{B}}d\boldsymbol{\vartheta} \qquad (2.22)$$

where $\boldsymbol{S}^{\mathcal{S}}$ is the skew symmetric counterpart of $\boldsymbol{s}^{\mathcal{S}}$ and $\boldsymbol{r}^{\mathcal{S}} = r\boldsymbol{s}^{\mathcal{S}}$.

From Equation 2.22 it is obvious that an error in the GPS position $\boldsymbol{a}^{\mathcal{L}}$ will propagate linearly into the resulting ground point coordinates $\boldsymbol{x}^{\mathcal{G}}$. So does the lever arm $\boldsymbol{b}^{\mathcal{B}}$ as well as the laser distance $\boldsymbol{r}^{\mathcal{S}} = r\boldsymbol{s}^{\mathcal{S}}$, though they are rotated with the attitude matrix. Thus an error in those vectors will show up as a linear effect, but rotated depending on the aircraft attitude. Especially the elements in nadir direction ($r_3^{\mathcal{B}}$ and $b_3^{\mathcal{B}}$) will affect the accuracy of the result's height, as the roll and pitch angles stay small while following the planned flight lines.

Equation 2.22 can also be written in matrix notation as

$$d\boldsymbol{x}^{\mathcal{L}} = \boldsymbol{A} \cdot d\boldsymbol{m} = \begin{pmatrix} \boldsymbol{I}, & \boldsymbol{R}_{\mathcal{L}/\mathcal{B}}, & \boldsymbol{R}_{\mathcal{L}/\mathcal{B}}\boldsymbol{R}_{\mathcal{B}/\mathcal{S}}, & \boldsymbol{R}_{\mathcal{L}/\mathcal{B}}r\boldsymbol{S}^{\mathcal{S}}, & \boldsymbol{R}_{\mathcal{L}/\mathcal{B}}\boldsymbol{L}^{\mathcal{B}} \end{pmatrix} \cdot \begin{pmatrix} d\boldsymbol{a}^{\mathcal{L}} \\ d\boldsymbol{b}^{\mathcal{B}} \\ d\boldsymbol{r}^{\mathcal{S}} \\ d\boldsymbol{\alpha} \\ d\boldsymbol{\vartheta} \end{pmatrix} \qquad (2.23)$$

By setting all but one element of $d\boldsymbol{m}$ to zero, it is easily possible to calculate the selected element's influence onto the ground point coordinates for a given airborne setting. In the following, three different flying heights (400, 700 and 1000 m) above ground and attitude angles of $\boldsymbol{\vartheta}^{T} = (0, 0, 0)$ are assumed. For the amplitude of $dm_i$, values of the system components' a priori accuracy information are considered. By setting $dm_i = \sigma_{m_i}$, the worst case effect of an error in one single component is studied.

| obs. | $dx_1$ [m] | $dx_2$ [m] | $dx_3$ [m] |
|---|---|---|---|
| $da_1 = 0.05\,\text{m}$ | 0.05 | | |
| $da_2 = 0.05\,\text{m}$ | | 0.05 | |
| $da_3 = 0.12\,\text{m}$ | | | 0.12 |
| $db_1 = 0.01\,\text{m}$ | 0.01 | | |
| $db_2 = 0.01\,\text{m}$ | | 0.01 | |
| $db_3 = 0.01\,\text{m}$ | | | 0.01 |

Table 2.3.: Estimation of influence of an error in one observable onto the ground point position.

For kinematic GPS ($d\boldsymbol{a}$), the accuracy is known from experiences in previous campaigns (e.g. Cocard, 1995; Favey and Schlatter, 1998). The accuracy of the lever

arm $d\boldsymbol{b}$ is known to be at the centimeter level, as it was measured terrestrially with theodolite and leveling (Geiger et al., 1997). All observables in Table 2.3 propagate linearly onto $d\boldsymbol{x}$, when assumed that the roll and pitch angles are $\approx 0$.

| obs. | $h = 400\,\text{m}$ | | | $h = 700\,\text{m}$ | | | $h = 1000\,\text{m}$ | | |
|---|---|---|---|---|---|---|---|---|---|
| | $dx_1^{\mathcal{L}}$ | $dx_2^{\mathcal{L}}$ | $dx_3^{\mathcal{L}}$ | $dx_1^{\mathcal{L}}$ | $dx_2^{\mathcal{L}}$ | $dx_3^{\mathcal{L}}$ | $dx_1^{\mathcal{L}}$ | $dx_2^{\mathcal{L}}$ | $dx_3^{\mathcal{L}}$ |
| $dr_1 = 0.0005r$ | 0.20 | | | 0.35 | | | 0.50 | | |
| $dr_2 = 0.0005r$ | | 0.20 | | | 0.35 | | | 0.50 | |
| $dr_3 = f(r)$ | | | 0.05 | | | 0.12 | | | 0.20 |
| $d\vartheta_1 = 0.01°$ | 0 | 0.07 | −0.02 | 0 | 0.12 | −0.03 | 0 | 0.17 | −0.04 |
| $d\vartheta_2 = 0.01°$ | −0.07 | 0 | 0.01 | −0.12 | 0 | 0.02 | −0.17 | 0 | 0.03 |
| $d\vartheta_3 = 0.01°$ | 0.02 | −0.01 | 0 | 0.03 | −0.02 | 0 | 0.04 | −0.03 | 0 |

Table 2.4.: Estimation of influence in [m] of an error in angle $d\vartheta_i$ onto the ground point position depending on the flying height above ground $h$.

The estimation of the magnitude of the laser vector errors $d\boldsymbol{r}^{\mathcal{S}}$ includes

- the uncertainty of the distance measurement dependent on the signal to noise ratio (see Equation 2.6), which in turn is proportional to the measured distance $r$ itself. This uncertainty affects essentially the component $dr_3$.

- the digital readout accuracy of the mirror position. This is the main part in the components $dr_1$ and $dr_2$ (Hug, 1996).

- the dynamic uncertainty of the mirror plane deviation (see Figure 2.8). This has been calibrated by the University of Stuttgart. The remaining errors are negligible compared to the item above, except for high dynamic flight conditions. According to Hug (1996), dynamic mirror inclination errors of up to 0.1° are possible, when the aircraft is subject to strong accelerations, causing greater errors (cf. Equation 7.4, page 132).

- the beam divergence $\delta$. Due to the c/w technique used for distance measurement (see Section 2.2.1), the resulting distance is the result of an integration over the whole footprint area. The footprint diameter is given as $d_F = r \cdot \delta$ Thus a horizontal displacement on a target with will result in a vertical shift on a target with a slope analogous to Equation 2.24.

The filiation of the influence of $d\boldsymbol{r}$ in Table 2.3 is described in detail by Hug (1996). The estimations were taken from his work, as well as from Thomas (2000).

The influence of an error in a misalignment angle $d\boldsymbol{\alpha}$ differs from an error in the attitude $d\boldsymbol{\vartheta}$ only by the absence of the lever arm $\boldsymbol{b}$. Thus the effect of an angular error is listed in Table 2.4 only for $d\boldsymbol{\vartheta}$, as a misalignment error will show up with nearly the same propagation behavior. The values were calculated with the assumption of a horizontal planar target. If the target is inclinated with a slope angle of $\beta$, the

errors in the horizontal ground point components $dx_1$ and $dx_2$ will as well propagate into the height component $dx_3$ with

$$dx_3 = dx_1 \cdot \tan\beta \sin\gamma + dx_2 \cdot \tan\beta \cos\gamma \tag{2.24}$$

depending on the slope direction $\gamma$. Using Unteraargletscher as target, this issue becomes important, as the surface slopes range from $10°$ at the confluence area up to more than $25°$ in the firn areas (cf. Table 7.5). In the cliff areas enclosing the glacier, the mean slope is even $40°$.

## 2.5.3.  Accuracy estimation for the ground point coordinates

Using the matrix $\boldsymbol{A}$ of Equation 2.23, the accuracy of $\boldsymbol{x}$ can be estimated as

$$\boldsymbol{C}_{xx} = \boldsymbol{A}\boldsymbol{C}_{mm}\boldsymbol{A}^T \tag{2.25}$$

where $\boldsymbol{C}_{xx}$ represents the covariance matrix of $\boldsymbol{x}$, and $\boldsymbol{C}_{mm}$ is filled with the covariances of the observables in $\boldsymbol{m}$. Assuming that all observables are independent from each other, $\boldsymbol{C}_{mm}$ can simply be written as

$$\boldsymbol{C}_{mm} = \begin{pmatrix} \sigma^2_{a^{\mathcal{L}}_1} & 0 & 0 & 0 & \dots & 0 \\ 0 & \sigma^2_{a^{\mathcal{L}}_2} & 0 & 0 & \dots & 0 \\ 0 & 0 & \sigma^2_{a^{\mathcal{L}}_3} & 0 & \dots & 0 \\ 0 & 0 & 0 & \sigma^2_{b^{\mathcal{B}}_1} & \dots & 0 \\ \vdots & \vdots & \vdots & \vdots & \ddots & \vdots \\ 0 & 0 & 0 & 0 & \dots & \sigma^2_{\vartheta_3} \end{pmatrix} \tag{2.26}$$

Using Equation 2.25 an estimation of the accuracy of the resulting ground point coordinates can be made by inserting known a priori values for $\sigma^2_{m_i}$. Using the same values as in the previous section, and assuming a horizontal, planar target, we get

$$\begin{aligned} \sigma_{x_1} &\approx 0.57 \cdot 10^{-3} \cdot r \\ \sigma_{x_2} &\approx 0.57 \cdot 10^{-3} \cdot r \\ \sigma_{x_3} &\approx 0.25 \cdot 10^{-3} \cdot r \end{aligned} \tag{2.27}$$

Of course $\sigma_{x_3} \geq 0.15\,\text{m}$ always holds true due to contributing elements which are independent of $r$. The limiting factors are especially the accuracy of the raw distance measurement and the GPS height accuracy.

For a tilted target, the height accuracy $\sigma_{x_3}$ gets worse analogous to Equation 2.24.

# 3. Processing of Kinematic GPS Data

## 3.1. Introduction

Kinematic differential GPS for determining the trajectory of a moving receiver is a widely used method (Seeber, 1993). Several approaches to fix the integer ambiguities 'on the fly' have been proposed and successfully implemented (e.g. Hatch, 1990; Teunissen, 1994; Cocard, 1995). Also for attitude determination, algorithms lended from spacecraft orientation have been adopted (van Graas and Braasch, 1991; Cohen and Parkinson, 1992) and dedicated multi-antenna GPS receivers with one single oscillator have been realized and tested (e.g. Cohen and Parkinson, 1991; Schwarz et al., 1992).

The INS attitude determination suffers from drift effects, which can be determined and corrected using a GPS attitude determination (Chapter 4). Using a multi-antenna array on the aircraft, the coordinates of all antennae relative one master antenna have to be determined at a high measurement rate. Ordinary single frequency GPS receivers have been used, each one connected to an antenna of the array on the aircraft (cf. Figure 2.4). The existing software approach for kinematic GPS processing (Cocard, 1995) needs to be extended to process moving baselines and provide the vectors needed for attitude determination.

Cocard (1995) gives a detailed analysis of the processing of kinematic GPS data. This chapter is composed of two parts. First, an extension of his approach to process moving baselines is presented. They are the needed link between the existing algorithms for trajectory recovery and the attitude determination approach presented in Chapter 4. The second part deals with problems specific to the airborne case of kinematic GPS processing.

## 3.2. Processing of a Moving Baseline of Single Frequency Observations

## 3.2.1. Observation Equations

Given two antennae mounted rigidly on a vehicle with a known geometry, the GPS observables inherently contain the attitude information of this baseline. The coordinates of a moving antenna (index $m$) are solved with respect to a chosen reference antenna (index $r$), which in this special case is moving along as well. After time-adjusting the resulting vector, it can directly be used for GPS attitude determination described in Section 4.3.

The basic observation equations for positioning are given as (e.g. Cocard, 1995):

$$\rho_r^s(t_R) = ||\boldsymbol{x}^s(t_T) - \boldsymbol{x}_r(t_R)|| + c \cdot \tau_r - c \cdot \tau^s + d_{Ion_r}^s + d_{Trp_r}^s \tag{3.1}$$

for code observations and

$$\varphi_r^s(t_R) = ||\boldsymbol{x}^s(t_T) - \boldsymbol{x}_r(t_R)|| - A^s\lambda + c \cdot \tau_r - c \cdot \tau^s - d_{Ion_r}^s + d_{Trp_r}^s \tag{3.2}$$

for carrier phase observations, where

| | |
|---|---|
| $t_T, t_R$ | 'true' transmitting and receiving time respectively |
| $c$ | speed of light in the vacuum |
| $||\boldsymbol{x}^s(t_T) - \boldsymbol{x}_r(t_R)||$ | slant range between satellite $s$ and receiver $r$ |
| $\tau^s, \tau_r$ | satellite and receiver clock bias respectively |
| $d_{Ion_r}^s, d_{Trp_r}^s$ | ionospheric and tropospheric path delay respectively |
| $\lambda$ | carrier wavelength |
| $A^s$ | ambiguity of the carrier phase |

For differential positioning, the same equations for a second, moving receiver $m$ are specified and the *single differences* are built:

$$\Delta\rho_{mr}^s(t_N) = \rho_m^s(t_{Nm}) - \rho_r^s(t_{Nr}) \tag{3.3}$$
$$\Delta\varphi_{mr}^s(t_N) = \varphi_m^s(t_{Nm}) - \varphi_r^s(t_{Nr}) \tag{3.4}$$

with the nominal time

$$t_{Ni} = t_{Ri} + \tau_i \tag{3.5}$$

for receiver $i$, respectively. Inserting Equations 3.1 and 3.2, this becomes:

$$\begin{aligned}
\Delta\rho_{mr}^s &= ||\boldsymbol{x}^s(t_{Tm}) - \boldsymbol{x}_m(t_{Rm})|| - ||\boldsymbol{x}^s(t_{Tr}) - \boldsymbol{x}_r(t_{Rr})|| \\
&\quad + c \cdot \Delta\tau_{mr} - c \cdot \Delta\tau_{mr}^s + \Delta d_{Ion_{mr}}^s + \Delta d_{Trp_{mr}}^s
\end{aligned} \tag{3.6}$$

$$\begin{aligned}
\Delta\varphi_{mr}^s &= ||\boldsymbol{x}^s(t_{Tm}) - \boldsymbol{x}_m(t_{Rm})|| - ||\boldsymbol{x}^s(t_{Tr}) - \boldsymbol{x}_r(t_{Rr})|| \\
&\quad + c \cdot \Delta\tau_{mr} - c \cdot \Delta\tau_{mr}^s - \Delta A^s\lambda - \Delta d_{Ion_{mr}}^s + \Delta d_{Trp_{mr}}^s
\end{aligned} \tag{3.7}$$

The satellite specific data such as its position $\boldsymbol{x}^s(t_T)$ and clock bias $\tau^s$ are known from precise ephemerides. Thus the unknown terms to be solved for are the moving

receiver position $\boldsymbol{x}_m(t_{Rm})$ and clock bias $\Delta\tau_{mr}$, the single difference ambiguities $\Delta A^s$, and eventually remaining error effects such as atmospheric and multipath effects, depending on the application.

The reference coordinates $\boldsymbol{x}_r$ can be set to the code solution of the chosen reference antenna, as only the orientation of the relative baseline vector with respect to the satellites is of interest. The length of this vector is theoretically constant (cf. Section 3.2.3).

## 3.2.2.  Time Bias Correction of Solved Baseline Vector

Looking at Equations 3.6 and 3.7, it is apparent that the resulting coordinates $\boldsymbol{x}_m(t_{Rm})$ and $\boldsymbol{x}_r(t_{Rr})$ provide not yet the components to calculate the vector needed for attitude determination:

$$\boldsymbol{k}(t_N) = \boldsymbol{x}_m(t_N) - \boldsymbol{x}_r(t_N) \tag{3.8}$$

Due to the fact, that the clock biases $\tau_m$ and $\tau_r$ are specific to each receiver, the true time at which the antenna coordinates are known differ $(t_{Rm} \neq t_{Rr})$, even though the nominal time of reception $(t_N)$ is the same. Yet to build the vector $\boldsymbol{k}$, the coordinates have to refer to the same time. With clock biases on the order of a millisecond and a flying speed of $\approx 70\,\mathrm{m/s}$, a vector 'distortion' of about $7\,\mathrm{cm}$ would be the result of asynchronous primitives.

Thus the coordinates of the reference and moving antennae must be adjusted to one and the same 'true' GPS time, at which vector $\boldsymbol{k}$ should be known. To be synchronous with the INS data, the suggestion is to adjust the coordinates to the nominal time $t_N$, at which the measurements should have been taken.

For receiver $j$ holds:

$$\boldsymbol{x}_k(t_N) \approx \boldsymbol{x}_j(t_{Rj}) + \tau_j \cdot \boldsymbol{v}_j(t_{Rj}) \tag{3.9}$$

where the velocity vector $\boldsymbol{v}_j$ can be derived by interpolating from the position solutions at the epochs $(i)$ and $(i+1)$:

$$\boldsymbol{v}_j(t_{Rj}) = \frac{\boldsymbol{x}_j\left(t_{Rj}^{(i+1)}\right) - \boldsymbol{x}_j\left(t_{Rj}^{(i)}\right)}{t_{Rj}^{(i+1)} - t_{Rj}^{(i)}} \tag{3.10}$$

## 3.2.3.  Constraining Baseline Length for Antenna Array

The single difference equations (3.3 and 3.4) are applied to two antennae mounted rigidly on a vehicle with a known geometry. Thus the baseline length theoretically remains constant during the whole flight. This fact can be exploited by constraining the baseline length during the ambiguity resolution process to help solving the ambiguities. Using the least squares approach described by Cocard (1995), pseudo

measurements are added as an additional line to the design matrix $\boldsymbol{A}$. For the difference of the antenna positions with known baseline length $l_{mr}$ holds:

$$||\boldsymbol{x}_m(t_{Rm}) - \boldsymbol{x}_r(t_{Rm})|| - l_{mr} = 0 \tag{3.11}$$

Note that the coordinates of the reference receiver $\boldsymbol{x}_r$ must be adjusted to the reception time of the moving receiver $t_{Rm}$ in order not to introduce a 'distorted' baseline length (cf. Section 3.2.2).

To add this pseudo observation to the design matrix, it must first be linearized as

$$l_{mr} - l_0 = \sum_i \frac{\partial l_i}{\partial p_i} dp_i = \sum_i a_i dp_i \tag{3.12}$$

where

$l_0$ is the approximated baseline length obtained from the GPS observations using approximative values $p_0$ for the unknown parameters,

$dp_i$ are the linearized unknown parameters,

$a_i = \frac{\partial l_i}{\partial p_i}$ are the coefficients of the linearization.

The coefficients $a_i$ are then with $\boldsymbol{x}_m = (x_m, y_m, z_m)^T$ and $\boldsymbol{x}_r$ analogously:

| $a_i =$ | $x_m$ | $y_m$ | $z_m$ | $c \cdot \Delta\tau_{mr}$ | $\Delta A^s$ |
|---------|-------|-------|-------|---------------------------|--------------|
|         | $e_x$ | $e_y$ | $e_z$ | 0                         | 0            |

$$\tag{3.13}$$

with

$$e_x = \frac{x_m - x_r}{||\boldsymbol{x}_m - \boldsymbol{x}_r||} \qquad e_y = \frac{y_m - y_r}{||\boldsymbol{x}_m - \boldsymbol{x}_r||} \qquad e_z = \frac{z_m - z_r}{||\boldsymbol{x}_m - \boldsymbol{x}_r||} \tag{3.14}$$

where $e_{x,y,z}$ are the cartesian coordinates of the unit vector between the moving receiver and the reference receiver, at the reception time of the moving receiver $(t_{Rm})$.

## 3.2.4. Summary and Results

The kinematic GPS evaluation software of Cocard (1995) is extended to be able to process single frequency GPS measurements of a moving baseline. This includes

- the ability to introduce reference coordinates of a moving reference receiver time synchronized with the observations,

- adjustment of the reference and resulting coordinates to different times,

- the ability to constrain the baseline to a known length to aid ambiguity resolution.
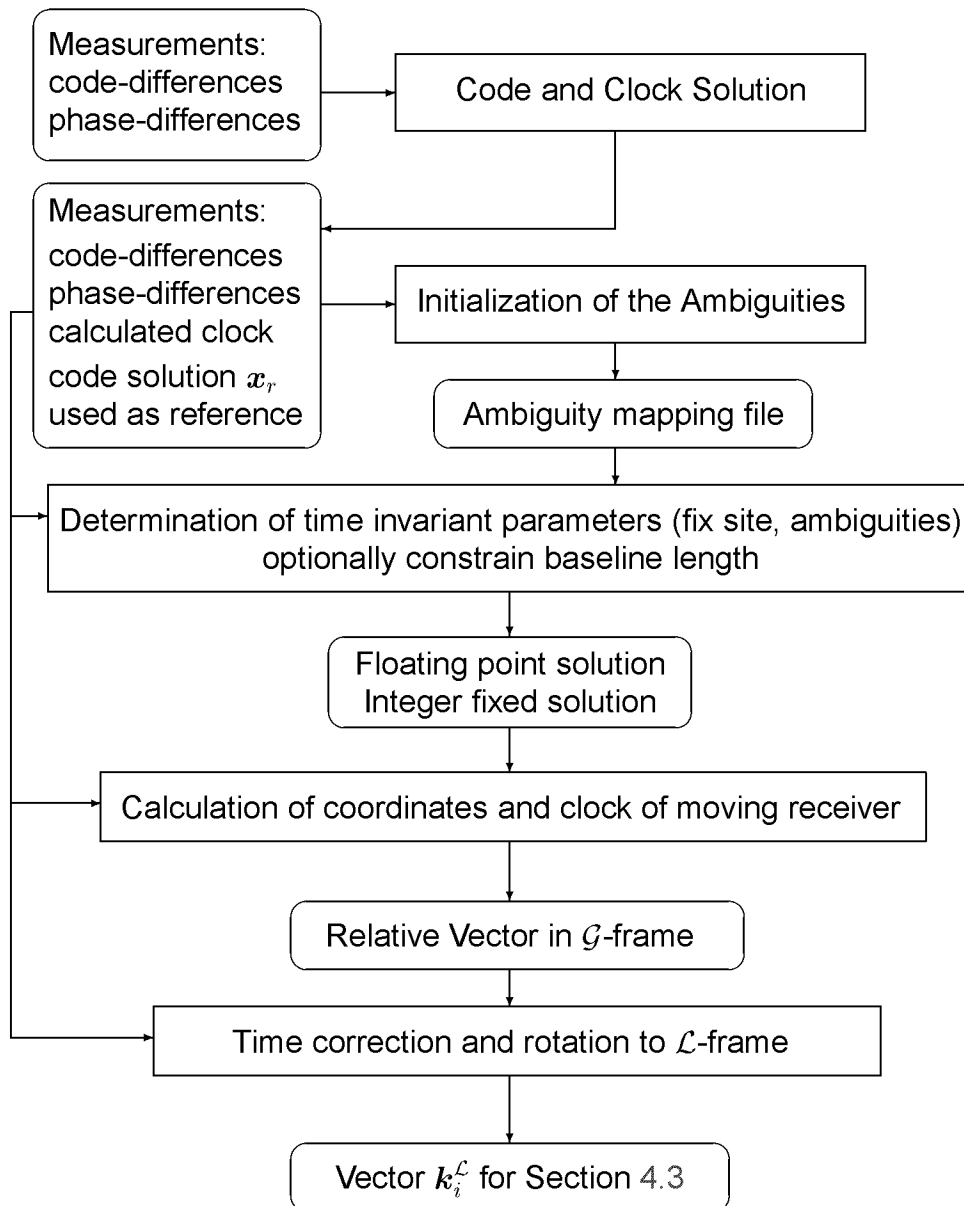
Figure 3.1.: Flowchart of extended GPS processing for attitude vectors.

| epochs # | flight | baseline | length [m] | RMS [cm] | mean [cm] | \|max\| [cm] | ua # |
|---:|---|---|---|---|---|---|---|
| 7879 | 99-244a | REAR-FRNT | 3.937 | 0.6 | −0.2 | 6.2 | 0 |
| 7879 | 99-244a | REAR-TAIL | 6.129 | 0.6 | 0.0 | 15.5 | 0 |
| 7879 | 99-244a | REAR-LEFT | 4.417 | 0.6 | −0.4 | 6.4 | 0 |
| 7879 | 99-244a | REAR-RGHT | 4.425 | 0.7 | −0.3 | 7.1 | 0 |
| 23040 | 99-244b | TAIL-FRNT | 9.737 | 0.5 | 0.1 | 7.1 | 0 |
| 23040 | 99-244b | TAIL-REAR | 6.129 | 0.6 | 0.2 | 23.8 | 0 |
| 23040 | 99-244b | TAIL-LEFT | 9.595 | 0.6 | −0.2 | 6.4 | 0 |
| 23040 | 99-244b | TAIL-RGHT | 9.598 | 0.6 | −0.3 | 5.7 | 0 |
| 3057 | 98-237c | FRNT-TAIL | 9.737 | 0.6 | 0.2 | 4.5 | 0 |
| 2729 | 98-237c | FRNT-REAR | 3.936 | 0.5 | 0.2 | 4.7 | 0 |
| 6656 | 98-237c | FRNT-LEFT | 3.033 | 0.6 | 0.0 | 5.5 | 0 |
| 6656 | 98-237c | FRNT-RGHT | 2.624 | 0.5 | −0.2 | 5.4 | 0 |
| 24836 | 98-238a | FRNT-TAIL | 9.737 | 0.5 | 0.1 | 6.2 | 0 |
| 12417 | 98-238a | FRNT-REAR | 3.936 | 0.9 | −0.1 | 13.6 | 1 |
| 24836 | 98-238a | FRNT-LEFT | 3.033 | 1.1 | −0.2 | 41.6 | 1 |
| 24836 | 98-238a | FRNT-RGHT | 2.624 | 1.1 | 0.1 | 17.7 | 1 |

Table 3.1.: Statistics of various moving baselines' evaluation results. The observable is the baseline length's deviation of the true length determined from the terrestrial lever arm measurements. Column ua stands for remaining unresolved ambiguities.

Figure 3.1 gives an overview of the modified processing for a moving reference-slave pair.

The resulting vectors $k_i$ of multiple reference-slave pairs can then be used to calculate the attitude of the aircraft (Section 4.3). Due to the short baselines on the aircraft, usually all ambiguities can be solved (cf. Table 3.1). The RMS of the difference of the baseline lengths determined by kinematic GPS minus the calibrated baseline length is of the order of 5–11 mm, depending on whether all ambiguities could be solved. The maximum deviations on the order of decimeters are due to steep turns of the aircraft between the lines, where loss of lock occurs and the number of available satellites decreases; under extreme circumstances as few as four satellites remain locked (e.g. during flight 98-238a).
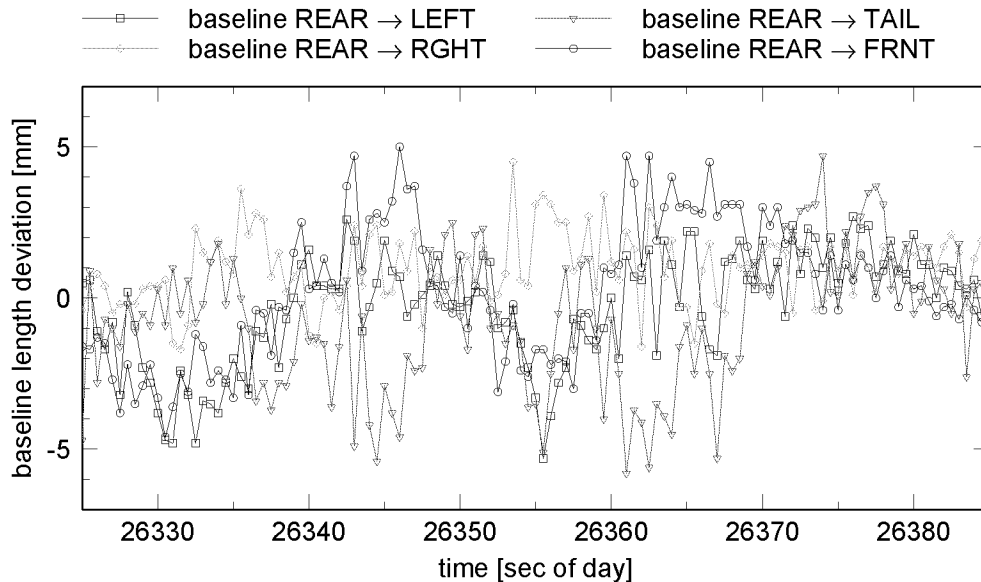


Figure 3.2.: Zoomed view of the baseline lengths' deviation of the true length during the laser scan flight 99-244a.

Figure 3.2 shows the typical baseline length's deviation from the calibrated length. The baseline length can be taken as an indicator for correctly solved ambiguities. Degradation of the differential position solution can be expected to originate from multipath effects and antenna phase center variations.

## 3.3.   Error Mitigation in Kinematic GPS Data

The GPS range measurements are affected by a variety of error sources like clock biases, tropospheric and ionospheric refraction, ephemeris errors, cycle slips, multipath, interference and noise. In static GPS measurements, most if not all of the

effects can successfully be estimated or eliminated by various techniques (Seeber, 1993). In a dynamic setting like in kinematic GPS applications, many of the effects cannot be estimated due to a strong correlation with the moving receiver's position. Yet they can be mitigated by choosing a measurement setup that minimizes the error effect.

## 3.3.1.   Detection of Cycle Slips in Kinematic Data

Many methods suitable for cycle slip detection in the static case cannot easily be applied to kinematic GPS data. Yet there exist a few methods, depending on what kind of observations can be logged by a specific receiver. Even though modern receivers are much less prone to cycle slips, they cannot be entirely excluded (Seeber, 1993). Common to all methods in a kinematic environment is that they may fail under severe ionospheric conditions with large short-time fluctuations (Cocard, 1995).

A strategy often followed is to detect a cycle slip within a Kalman filter position estimation process. The basic idea is to estimate the new position using past GPS data, doppler measurements, and—if available—INS data (Lipp and Gu, 1994). Cycle slips can be identified and corrected, when this estimate is compared with the measurements, and the accuracy of the estimation is better than a fraction of one cycle. Whether this method succeeds depends on the flight dynamics and the measuring frequency. During periods of high dynamics (e.g. during curves or with heavy turbulences) when a loss of lock is most likely, the estimates of such an extrapolation usually are not good enough (Cocard, 1995).

If both carrier phase measurements are available, the geometry-free linear combination L4 may be used to detect cycle slips:

$$\varphi_4 = \varphi_1 - \varphi_2 = \lambda_1 A_1 - \lambda_2 A_2 + (d_{Ion1} - d_{Ion2}) = \text{const} + \alpha d_{Ion} \tag{3.15}$$

Looking at subsequent epochs of L4 measurements, a cycle slip is indicated by the following difference:

$$\Delta\varphi_4 = \varphi_4(t_{i+1}) - \varphi(t_i) \approx \alpha \cdot \partial_t d_{Ion} \cdot \Delta t + \lambda_1 S_1 - \lambda_2 S_2 \tag{3.16}$$

where $S_1$ and $S_2$ are a cycle slip in the L1 and L2 measurement respectively. The change rate of ionospheric refraction $\partial_t d_{Ion}$ is negligible for small values of $\Delta t < 1\,\text{s}$. It is difficult to discriminate, in which frequency a cycle slip occurred, as the indicator is a combination of both. Theoretically, a cycle slip could occur in both frequencies simultaneously with opposite magnitude $\lambda_1 S_1 \approx \lambda_2 S_2$ passing the screening undetected. Yet the probability of such a case is rather small.

If phase rate measurements are available, the screening can be done on a per frequency basis. Using this method, the data of the single frequency receivers can also be screened. A cycle slip is indicated by the following difference:

$$S = \varphi(t_{i+1}) - \varphi(t_i) - \dot{\varphi} \cdot \Delta t \tag{3.17}$$

where $\dot{\varphi}$ is the phase rate measurement. This method is prone to dynamic flight behavior which degrades the approximation of the phase difference by the phase rate. A second limiting factor is the measuring noise of the phase rates. These two effects may turn the discrimination of a cycle slip to an impossible mission.

## 3.3.2.  Atmospheric Influences

The influence of ionospheric refraction can be modeled and estimated, if both GPS frequencies were observed by both, the reference as well as the moving receiver. For trajectory recovery, the ionospheric bias was introduced as an additional unknown as described by Cocard (1995). He states that by introducing this additional unknown, the percentage of epochs with correctly resolved ambiguities becomes significantly higher. Recent research developments try to fully model the ionospheric refraction using a regional permanent network of GPS receivers and a tomographic approach (Colombo, 2000).

In the case of moving baselines, which are at most 20 m long, the ionospheric refraction is negligible, as $\Delta d_{Ion_{mr}^s} \to 0$ (Equations 3.6 and 3.7). The same holds true for the tropospheric bias $\Delta d_{Trp_{mr}^s}$, as the path from the satellites to the antennae is nearly identical.

Yet, the troposphere remains as an only partially modeled error component for longer baselines appearing in the trajectory solution. Most of the troposphere effect can be modeled using the assumption of a standard atmosphere (see Appendix B.1). In this case, the formula of Saastamoinen (1973) is often applied:

$$d_{\text{Trp}} = 0.002277 \sec z \left( p + \left( \frac{1255}{T} + 0.05 \right) e - B \tan^2 z \right) + \delta \qquad (3.18)$$

where

| | |
|---|---|
| $d_{\text{Trp}}$ | the range correction in meter, typically on the order of 2 m. |
| $z$ | the apparent zenith distance of the satellite, for practical purposes, this value can be set to the true zenith distance |
| $p$ | the total barometric pressure in millibars, (standard atmosphere cf. Equation B.3) |
| $e$ | the partial pressure of water vapour in millibars, (standard atmosphere cf. Equation B.4) |
| $T$ | the absolute temperature in degrees Kelvin, (standard atmosphere cf. Equation B.2) |
| $B$ and $\delta$ | correction quantities for which Saastamoinen (1973) provides tabular information. In most cases, they can be set to approximative values: $B = 1$ and $\delta = 0$. |

The deviation of the standard atmosphere model values for pressure, temperature and water vapour pressure may lead to systematic height errors. For example in a

static GPS network in an Alpine valley with station heights differing up to 1000 m, a 'mismodeling' of the troposphere due to a temperature inversion resulted in height errors of about 10 cm (Geiger, 1988). GPS tomography for determining the tropospheric path delays is subject to recent research (Kruse, 2000), requiring a network of GPS receivers similar to the ionospheric approach.

The influence of tropospheric refraction onto the GPS height coordinate is for $z_{max} = 70°$ (Geiger, 1987):

$$\Delta h = 2.7 \Delta d_{Trp} \tag{3.19}$$

A deviation of the modeled troposphere from actual troposphere is thus amplified with a factor of almost 3. In the application of differential GPS evaluation, the height difference between the stations will be too small, if the modeled path delay is smaller than the actual path delay.
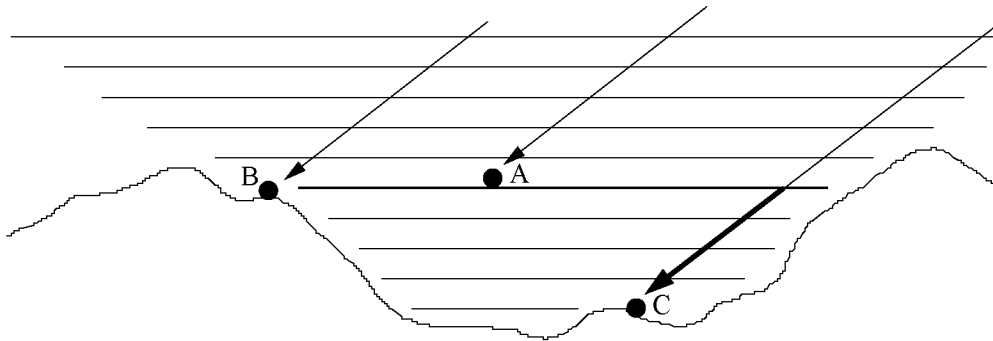


Figure 3.3.: Influence of the troposphere on relative positioning. Consider A to be the aircraft, B and C are reference receivers located on the ground in the vicinity of the target area. A possible error in modeling the troposphere will show an impact proportional to the height difference between the aircraft and the reference receiver.

Tropospheric mismodeling affects kinematic relative positioning more severly, the greater the altitude difference is between the reference ground station and the moving receiver on the aircraft (Figure 3.3). Such a systematic effect propagates directly into the georeferenced ground point position in an absolute manner (cf. Equation 2.22).

To mitigate this effect for the laser scanning campaigns, reference stations were chosen at about the same altitude as the flight lines. Table 3.2 gives an overview of the available reference station's mean height differences and baseline lengths to the respective laser scanning target area. If the kinematic data is evaluated from takeoff to landing, the aircraft will move through the tropospheric layers at least twice. It may thus move through an inversion layer having the standard troposphere model mismatch the actual conditions. Blomenhofer and Hein (1995) found the position solution residuals to be strained up to 20 cm for low elevation satellites in a precision approach scenario. The degrading effect of this layer crossing on the ambiguity

| station ID | target area | dist [km] | $\Delta h$ [km] |
|---|---|---|---|
| ZIMM | Aaregletscher | 63 | 2.5 |
| GRIM | Aaregletscher | 14 | 1.3 |
| JUJO | Aaregletscher | 13 | 0.0 |
| ETHZ | Runway Dübendorf | 10 | 0.3 |

Table 3.2.: Reference stations' mean distance and height difference to the laser scanner target area and flying height.

solution could thus be mitigated by limiting the trajectory solution to the period from reaching to leaving the mission altitude, if the flight mission itself lasts long enough.

The troposphere zenith path delay can be modeled using data from a network of meteorological ground stations. For Switzerland, this was done using a collocation method (Cocard et al., 1992). The software was named *Comedie*, which stands for '**Co**llocation of **Me**teorological **D**ata for **I**nterpretation and **E**stimation of Tropospheric Path Delays'. The accuracy of this zenith path delay model is on the order of 2 cm (Troller et al., 2000).

To see how the mismodeling of the troposphere may affect the kinematic GPS coordinates, the zenith path delay was calculated for each epoch and position of the aircraft trajectory as well as for the reference station using Comedie. This path delay was then mapped to the satellite zenith distance $z$ and applied as $\Delta d_{\text{Trp}}$ instead of the standard atmosphere approach. The mapping function used is derived from a horizontal atmosphere layer model as (Höflinger, 1993):

$$\Delta d_{\text{Trp}}(z, h) = \frac{\sqrt{R^2 \cos^2 z + 2RH + H^2} - R \cos z}{H} \Delta d_0 \qquad (3.20)$$

where

$$R = R_{\ominus} + h$$
$$H = H_T - h$$

and

$\Delta d_{\text{Trp}}$ the range correction in meter

$\Delta d_0$ the zenith path delay calculated using Comedie

$z$ the apparent zenith distance of the satellite, for practical purposes, this value can be set to the true zenith distance

$h$ the altitude of the GPS antenna

$R_{\ominus}$ the earth radius, $R_{\ominus} = 6\,378\,137\,\text{m}$

$H_T$ the altitude of the tropopause, $H_T = 12\,000\,\text{m}$
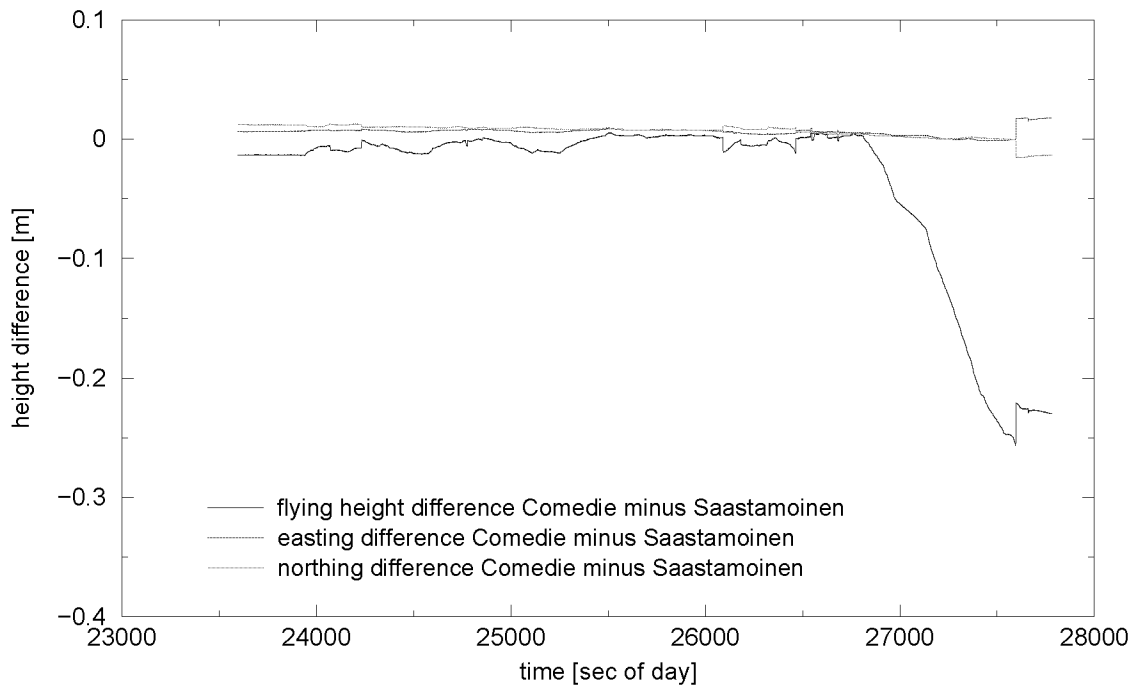
Figure 3.4.: Example of effect of differential troposphere error mismodeling. Trajec-
tory of glacier campaign 1999 using JUJO as reference station. The end
of the flight trajectory shows the increasing mismodeling effect onto the
height coordinate. This is due to an increasing height difference (up
to 3 km) between reference and moving receiver during approach and
landing.

Figure 3.4 shows the difference of a trajectory solution over the glacier using JUJO as reference station. The data evaluation window starts a few minutes before reaching the test area and ends with the landing procedure at the airport. As the major part of the trajectory is at the same altitude as the reference station itself, the differential modeling error effect onto the height coordinate is on the order of a few centimeters. As soon as the aircraft approaches the airport, the height difference between the reference and moving receivers increases. As the actual tropospheric meteo conditions modeled by Comedie do not coincide with the standard atmosphere values, the Saastamoinen approach uses, the mismodeling effect on the moving receiver's height increases up to 0.2 m.

As such a systematic height offset will directly propagate into a meteo-contamined surface elevation change estimate, it is important to either select the reference station location at the same altitude as the flying height or to model the tropospheric refraction correction using the actual meteo conditions.

### 3.3.3.   Multipath, Interference and Satellite Visibility Issues

**Multipath**

GPS multipath of a moving receiver still is in the early stages of research. Braasch (1994) tried to separate multipath errors from other receiver tracking errors due to acceleration of the antenna. As for the phase multipath, these two effects are of the same order, about a fourth to a third of the carrier phase wavelength.

Multipath error for GPS based attitude determination was studied by Cohen and Parkinson (1991) for the special case of a single oscillator multi-antenna receiver. He assumes, that the aircraft merely is a reflector causing multipath by mirroring satellites at always the same elevation and azimuth relative to the body frame. This assumption was also investigated by Lipp et al. (2000), who studied the signal to noise standard deviation distribution over the positive hemisphere above the aircraft. They collected data from various intercontinental flights. The resulting spatial distribution of the signal to noise standard deviation showed clearly an increase in the direction of the wings relative to the GPS antenna.

Even signal loss of satellites can occur due to multipath effects. Scaramuzza (1998) investigated signal loss that took place at specific satellite elevations. He showed, that the elevation dependent signal loss of a stationary reference receiver can be verified using a modeled reflector.

In the case of GPS receivers mounted on an aircraft, multipath error is also closely related the antenna phase center variations. (Wübbena et al., 2000) notes, that an aircraft surface should actually be considered as part of the antenna.

## Interference

Critical for the positioning solution is the unintentional and intentional Radio Frequency Interference (RFI) from radio stations in the proximity of the flight path. This is a serious threat to a usable result of airborne laser scanning. Scaramuzza (1998) found an RFI in the region of Lugano-Agno caused by an identified interfering station sending close to the L1 frequency. During our laser scanner flights, a signal loss of all L2 satellites occurred while on the way to the test area. The L1 data suffered substantial degradation as well. The post processing of the GPS data for the positioning solution had to be reduced to the part of the trajectory just over the target area, in order to achieve satisfactory results for ambiguity resolution.
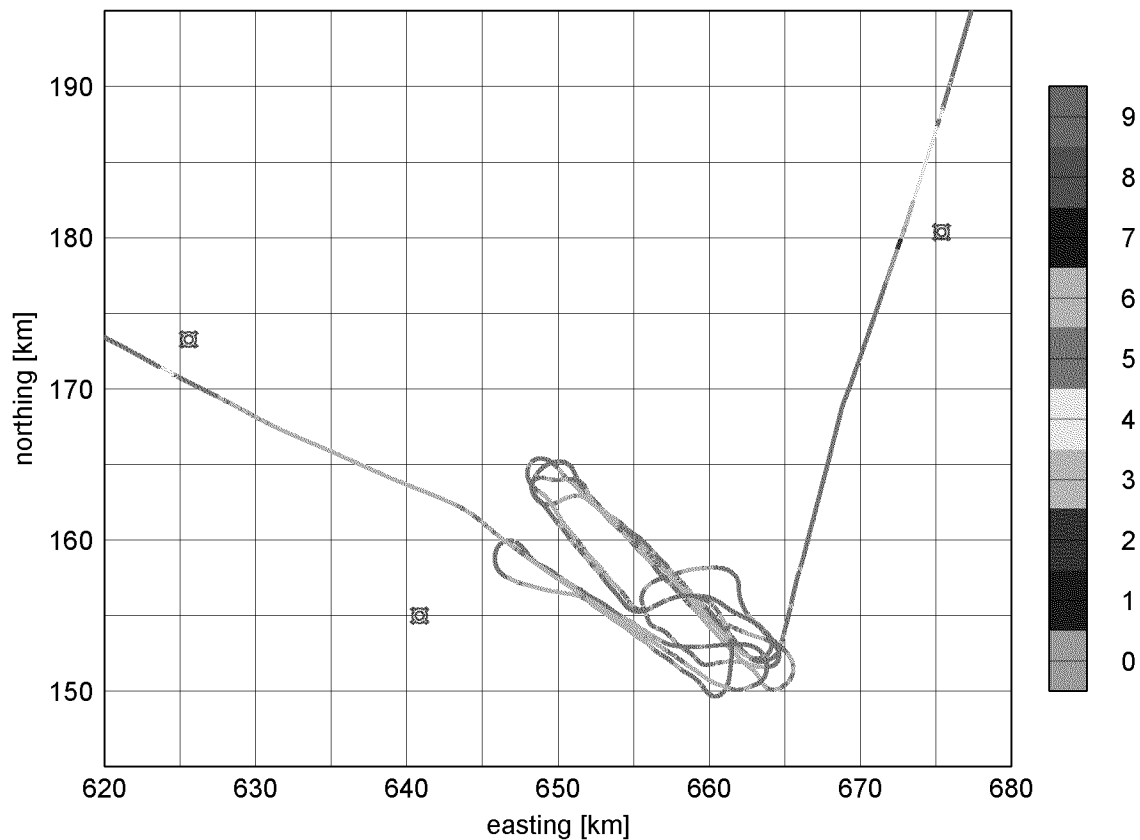


Figure 3.5.: Signal loss of the L2 frequency due to interference. The red symbols are potential interfering stations, where communications radio equipment is installed. The color scale denotes the average L2 carrier frequency signal to noise ratio. A value of zero means, that all satellites have been lost.

Figure 3.5 shows, that the signal loss happened just a few kilometers away from the Titlis radio equipment. After the completion of scanning the target area, the L2 frequency is degraded again when passing next to the Niederhorn radio station.

The presence of interfering stations in the proximity of the area to be mapped by laser scanning should always be part of flight planning procedures, in order to avoid flights with unusable data.

## Satellite Visibility

The issue of satellite visibility is closely related to multipath effects. GPS receivers track satellites, as long as they are visible. In the case of the laser scanning flights, the receivers apparently also track satellites, that are theoretically invisible due to obstruction by the aircraft body (Figure 3.6). All 5 antennae on the aircraft used for attitude determination were tracking satellites as low as -40° due to banking of the aircraft.

These theoretically invisible satellite observations do not appear with extraordinary residuals in the GPS evaluation. It is yet unclear, how this affects the ambiguity resolution quality of the trajectory.

It is well known that the antenna phase center is not stable with respect to varying azimuth, elevation or frequency. Antenna phase center variation calibration for the total hemisphere was studied by Wübbena et al. (2000). The antenna is rotated in azimuth and elevation when mounted on a robot in order to get satellite observations in all parts of the antenna frame hemisphere. The exact location of the antenna is known due to the known robot positions. A phase center variation diagram is defined for each calibrated antenna. Yet it is questionable, if these variations stay the same, when an antenna is mounted on a conducting skin of a vehicle.

An even more severe reason satellite visibility is reduced is the rough topography where glaciers generally are located. Due to obstruction from nearby mountains, the GPS receivers may be unable to track enough satellites for a good position solution. If the number of locked satellites drops below 5, the DOP quality indicator will increase rapidly. In such a case, the laser data cannot reliably be georeferenced. Figure 3.7 shows this problem on the laser strip closest to the Finsteraarfirn.
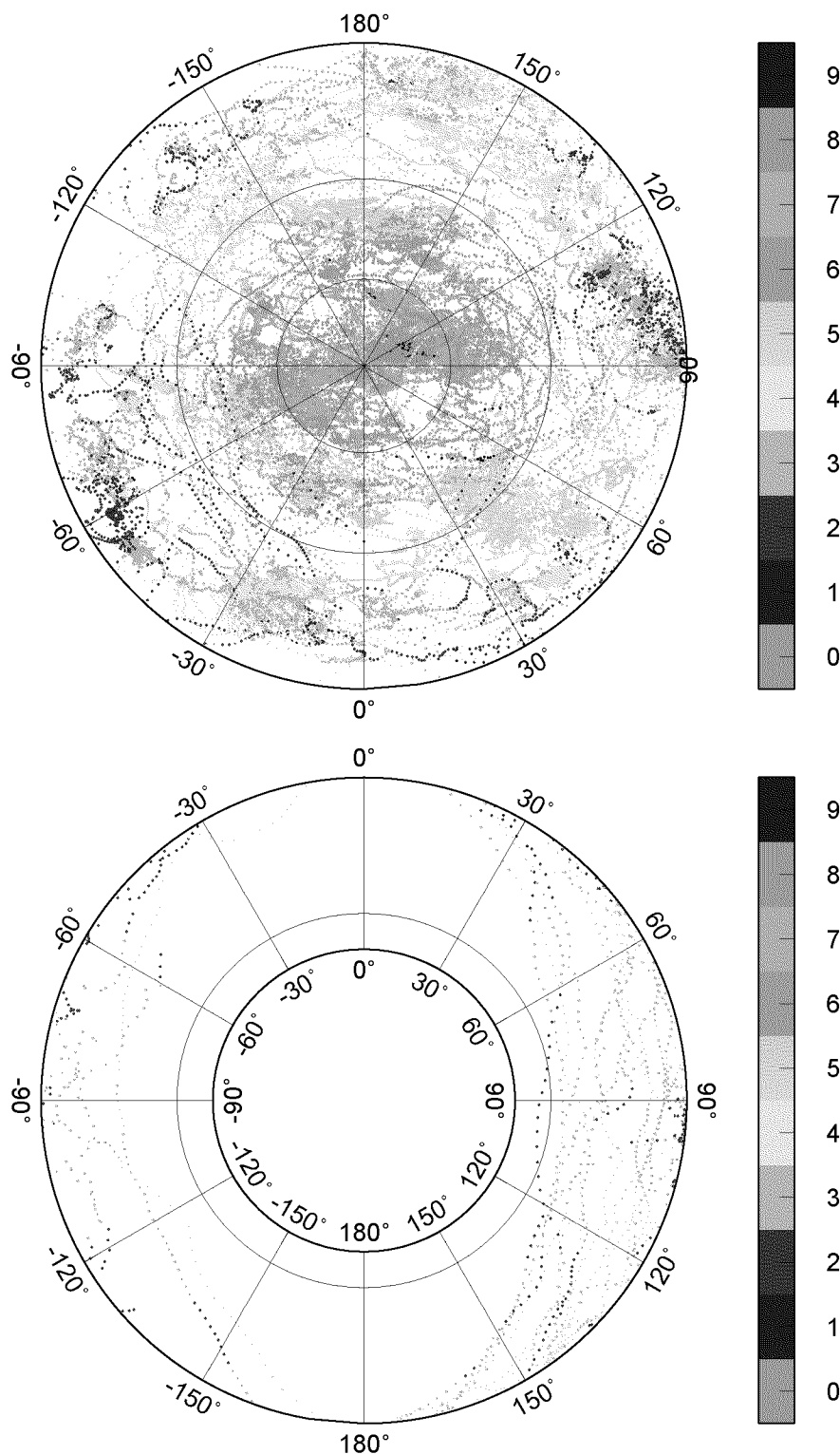
Figure 3.6.: Signal to Noise in Body frame elevation and azimuth of the L1 measurements of the REAR receiver. The satellites are tracked both in the positive (top plot) and negative (bottom plot) hemisphere of the aircraft. Note the antenna keeping the phase lock down to over 30° below the aircraft horizon.

Favey, E., 2001. *Investigation and Improvement of Airborne Laser Scanning Technique for Monitoring Surface Elevation Changes of Glaciers*. ETH Zurich, Diss. No. 14045
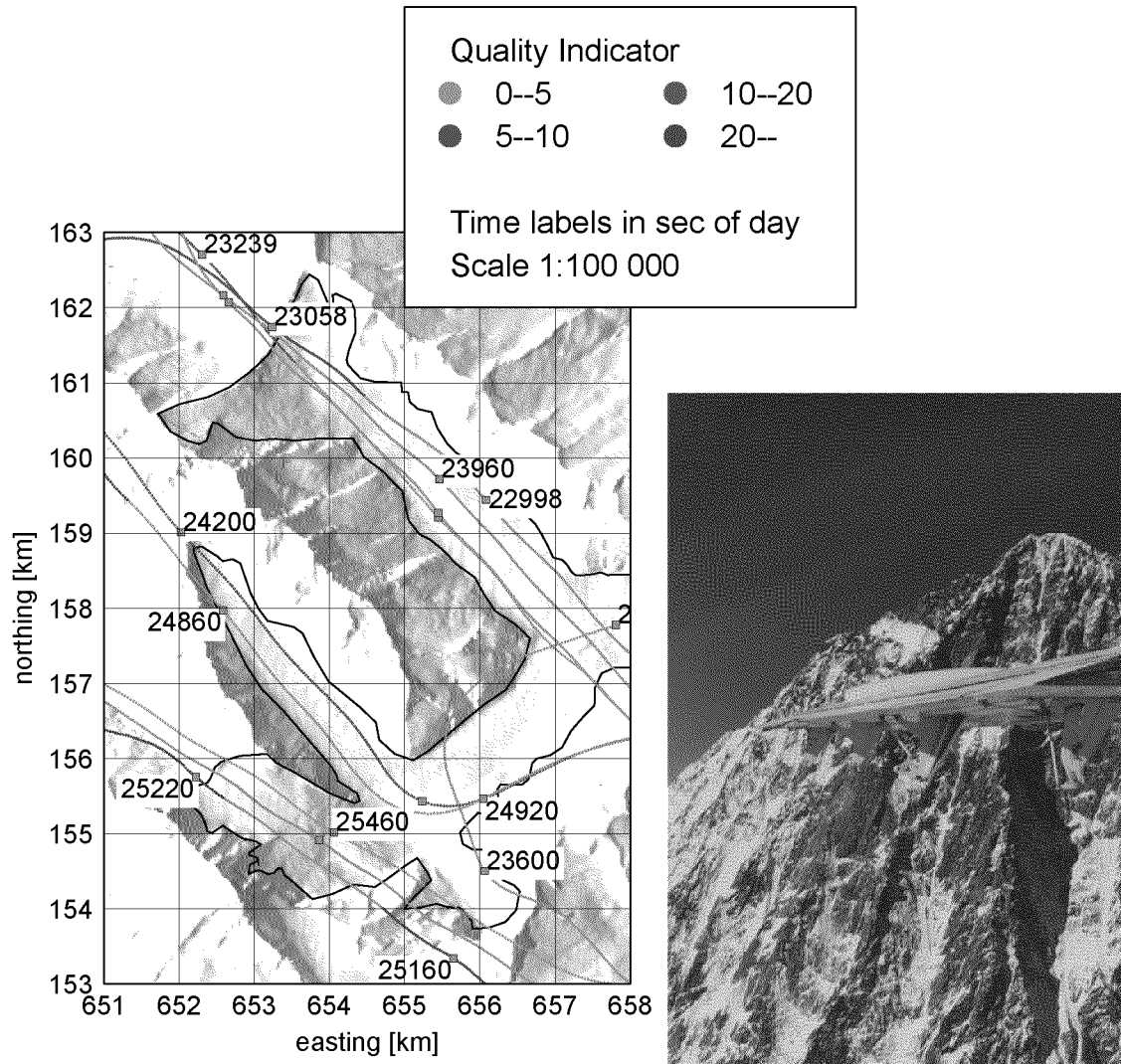
Figure 3.7.: Signal loss due to obstruction by a mountain just before second 25220 (flight 1998). The photograph illustrates this problem, which is symptomatic to the use of GPS in an alpine environment.

# 4. Attitude Determination

## 4.1.  Introduction

Apart from positioning, sensor orientation is mainly a matter of determining the platform's attitude with sufficient accuracy. Military applications spawned numerous systems based on inertial navigation technology, which unfortunately often appear to be expensive, difficult to acquire, and designed specifically for navigation rather than sensor orientation (Greenspan, 1995). Only very recently, commercial systems designed for sensor orientation have become available. First validations of such systems have been performed recently by comparing the systems' solutions with the orientation parameters of a photogrammetric bundle block adjustment (e.g. Cramer et al., 2000).

In this chapter, the coordinate systems, rotation matrix and several existing attitude determination methods are reviewed. The realization of an attitude determination system for the laser scanner orientation is described. A GPS multi-antenna system is developed to sustain the solution of a medium-cost inertial system. This solution is compared with the Applanix Positioning and Orientation System (POS), which became available during the last flight.

## 4.2.  Coordinate Systems and Rotation Matrix

The attitude of a platform is the orientation of its body frame coordinate system with respect to an extrinsic reference coordinate system. As a vector is always given related to a specific coordinate system, its transition into the representation within a different coordinate system can be expressed by a rotation matrix. In other words, the orientation of a coordinate system can be made identical to another by a rotation matrix. Coordinate systems and rotation matrices are the two basic elements in defining and estimating the attitude of a platform.

### 4.2.1.  Reference Systems for Georeferencing

When talking of a coordinate system, we think of the definitions of the origin and the directions in a theoretical manner. The realization of a system using measurements

and producing lists of coordinates is called a coordinate frame. Thus a coordinate frame is an approximative realization of the theoretical concept behind a system definition.

The reference coordinate systems usually used for platform attitude determination consist of three mutually orthogonal unit vectors $i_k$ chosen according to right hand conventions (Farrell, 1976).

## Earth fixed, geocentric coordinate system $\mathcal{G}$

This coordinate system is defined according to the world wide reference systems used in satellite geodesy. Origin is the center of mass of the earth. The orientation of the axes is defined as:

$i_1^{\mathcal{G}}$: in direction of the reference (Greenwich) meridian
$i_2^{\mathcal{G}}$: as $i_3^{\mathcal{G}} \times i_1^{\mathcal{G}}$
$i_3^{\mathcal{G}}$: in direction of the north pole

When using GPS, the conventional terrestrial reference frame (TRF) is WGS84. Yet the realization of this frame has been evolving during the past few years and minor changes had been made (NIMA, 2000). Thus, the TRF chosen for this project is CHTRF95, which is discussed more in detail in section 7.1.

## Local level coordinate system $\mathcal{L}$

The local level coordinate system is used as a reference to measure the attitude of a platform. It is a north oriented, topocentric system that is 'locally level' in geometrical sense, e.g. its $i_3$ unit vector is anti-parallel to the ellipsoid normal. One GPS antenna is selected to be the origin.

$i_1^{\mathcal{L}}$: in north direction
$i_2^{\mathcal{L}}$: in east direction
$i_3^{\mathcal{L}}$: in nadir direction (towards the earth)

Beware that the local level system is frequently used in other textbooks with a different definition: $i_3$ in zenith direction and therefore $i_2$ and $i_1$ in north and east direction respectively. As the laser system points towards nadir, it is more natural to define the system as used widely in navigation (e.g. Farrell, 1976).

## Aircraft body coordinate system $\mathcal{B}$

This coordinate system has its origin at same point as the local level system $\mathcal{L}$, but the vectors $i_k^{\mathcal{B}}$ are bound to the aircraft body:

$i_1^{\mathcal{B}}$: in flight direction along the forward fuselage

$i_2^{\mathcal{B}}$: in direction of the right wing

$i_3^{\mathcal{B}}$: in down direction toward the floor of the aircraft

In the special case where the body coordinate system is perfectly aligned with the local level coordinate system, the roll, pitch and yaw angles are zero.

## Laser hardware body coordinate system $\mathcal{S}$

This coordinate system has its origin at same point as the body system $\mathcal{B}$, but the vectors $i_k^{\mathcal{S}}$ point into slightly different directions, called the boresight misalignment. This misalignment remains constant, as the laser system is rigidly mounted on the platform. The section 5.3 on calibration deals in detail with the determination of these parameters.

## Strapdown IMU coordinate system

The attitude angles an Inertial Measuring Unit (IMU) gives as output define the rotation matrix of a body frame defined by the IMU body. This frame is misaligned with respect to the aircraft body frame realized by the GPS antenna array. As the strapdown drift errors are estimated as the orientation deviation of the IMU frame from the body frame, this eliminated drift inherently includes the frame misalignment angles.

## 4.2.2.   Rotation Matrix and Euler Angles

Assuming that two coordinate systems share the same origin, but have a different orientation, it is well known that one system can be rotated into the other by three consecutive rotations around the coordinate axes (e.g. Farrell, 1976). The three rotation angles are called Euler angles. While there are several alternative rotation sequences for representing the same rotation, not all are equally applicable to suit georeferencing airborne laser scanning data. This means that the three Euler angles which align two coordinate systems are not unique and depend on the specified rotation sequence. As all possible sequences contain singularities or discontinuities, the choice which one to use is usually made depending on the application (Farrell, 1976). If absence of singularities is needed, the rotation can also be constructed using quaternion representation.

For airborne laser scanning, it is suitable to use a Euler angle representation of the rotation matrix, as shown in Figure 4.1. The elementary rotations to compose a full
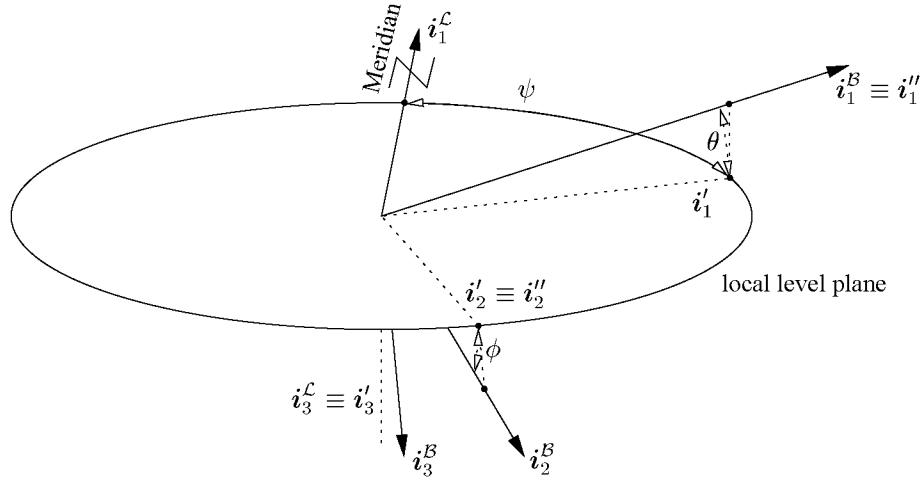
Figure 4.1.: The body frame $\mathcal{B}$ is assumed to be in an arbitrary orientation. Using three elementary rotations, the body frame can be aligned with the local level frame $\mathcal{L}$. The platform is first rotated by the roll angle around the $i_1^{\mathcal{B}}$-axis until $i_2$ lies within the local level plane becoming $i_2''$ $(R_1(-\phi))$. A second rotation around the $i_2''$-axis by the amount of the pitch angle is performed, such that $i_1$ as well gets to be within the local level plane $(R_2(-\theta))$. The rotation remaining is around the $i_3'$-axis by the amount of the yaw angle $(R_3(-\psi))$.

rotation matrix are:

$$
R_1 = \begin{pmatrix} 1 & 0 & 0 \\ 0 & \cos\vartheta_1 & \sin\vartheta_1 \\ 0 & -\sin\vartheta_1 & \cos\vartheta_1 \end{pmatrix} \quad R_2 = \begin{pmatrix} \cos\vartheta_2 & 0 & -\sin\vartheta_2 \\ 0 & 1 & 0 \\ \sin\vartheta_2 & 0 & \cos\vartheta_2 \end{pmatrix} \quad R_3 = \begin{pmatrix} \cos\vartheta_3 & \sin\vartheta_3 & 0 \\ -\sin\vartheta_3 & \cos\vartheta_3 & 0 \\ 0 & 0 & 1 \end{pmatrix}
$$

$$(4.1)$$

Thus, according to Figure 4.1, the overall attitude matrix is

$$
R_{\mathcal{L}/\mathcal{B}} = R_3(-\psi)\,R_2(-\theta)\,R_1(-\phi) \tag{4.2}
$$

$$
= \begin{pmatrix} \cos\psi\cos\theta & -\sin\psi\cos\phi + \cos\psi\sin\theta\sin\phi & \sin\psi\sin\phi + \cos\psi\sin\theta\cos\phi \\ \sin\psi\cos\theta & \cos\psi\cos\phi + \sin\psi\sin\theta\sin\phi & -\cos\psi\sin\phi + \sin\psi\sin\theta\cos\phi \\ -\sin\theta & \cos\theta\sin\phi & \cos\theta\cos\phi \end{pmatrix}
$$

$$(4.3)$$

From Equation 4.3 the Euler angles can easily be extracted from the matrix $R_{\mathcal{L}/\mathcal{B}}$

as

$$\phi = \arctan\left(\frac{r_{32}}{r_{33}}\right) \tag{4.4}$$

$$\theta = \arcsin(-r_{31}) \tag{4.5}$$

$$\psi = \arctan\left(\frac{r_{21}}{r_{11}}\right) \tag{4.6}$$

where $r_{ij}$ corresponds to the respective element of $\boldsymbol{R}_{\mathcal{L}/\mathcal{B}}$ (Equation 4.3) of the row $i$ and column $j$.

Above equations show a singularity occurring, when $\theta = \pm\frac{\pi}{2}$. In this case it becomes evident that the roll angle $\phi$ and the yaw angle $\psi$ are undefined. During a laser scanning flight, such a situation is not expected to occur.

Note that a rotation matrix $\boldsymbol{R}$ is an orthogonal matrix, i.e.

$$\boldsymbol{R}^{-1} = \boldsymbol{R}^T \quad \text{and} \quad \boldsymbol{R}\boldsymbol{R}^T = \boldsymbol{I} \tag{4.7}$$

This property is applied to all rotation matrices throughout this research. This also means that e.g. $\boldsymbol{R}_{\mathcal{L}/\mathcal{B}} = \boldsymbol{R}_{\mathcal{B}/\mathcal{L}}^T$.

## 4.3.    Attitude Determination from Multiple GPS Receivers

Attitude determination of an aircraft using GPS has been applied successfully in experiments by a number of researchers. If at least three GPS antennae are mounted on a platform in a non-collinear manner, and the differential GPS measurements are simultaneously collected, the baseline vectors between the antennae can be determined by choosing one antenna to be the reference (see section 3.2). Those vectors are given in the terrestrial reference frame, and can easily be transformed to the local level frame by using the latitude and longitude of the master antenna's position solution. As the antennae are rigidly mounted on the aircraft, their coordinates are also known in the body frame.

Thus the problem of attitude determination using GPS is formulated as follows: Given $n \geq 2$ non-collinear vectors in a local level coordinate frame as well as in a body coordinate frame, find the rotation matrix, that transforms the vectors from one system into the other.

This problem is similar to the one in spacecraft attitude determination by measuring direction vectors to fixed stars (e.g. Wahba, 1965). It is usually solved by either a singular value decomposition method (Markley, 1988), or by some type of eigenvalue decomposition (e.g. Wertz, 1978).

One drawback related to these decomposition methods is the complexity of accuracy analysis of the estimated attitude parameters (Lu, 1995). Additionally, the variance

and covariance information related to the GPS derived coordinates are not properly taken into account in the estimation process. Cohen et al. (1992) modified the solution for GPS measurements to fully take into account the measurement errors, but the body frame coordinates' errors are still left aside.

To be able to include all available variance and covariance information, Lu (1995) proposes an attitude estimation solution by an implicit least squares model. It makes use of the known antenna geometry to help ambiguity resolution. In his approach, the vectors are not explicitly calculated, but the attitude parameters are directly expressed as a function of double difference carrier phase measurements.

In the following, an approach is developed which is similar to the one used by Lu (1995), but the DGPS vectors obtained from the solution of antenna baselines in Section 3.2 are directly used instead of resorting to the ambiguities directly.

This allows a modularization of the data processing without loosing information, as mathematically speaking, the resulting attitude parameters should be equal for the baseline approach and the carrier phase measurement approach (Lu, 1995).

## 4.3.1. Approximate Solution from Two Vectors

Given a certain number of vectors $\boldsymbol{k}_i$ in the body frame $\mathcal{B}$, and the same set of vectors in the local level, north oriented frame $\mathcal{L}$, the rotation matrix $\boldsymbol{R}_{\mathcal{B}/\mathcal{L}}$ is sought, that will map $\boldsymbol{k}_i^{\mathcal{L}}$ onto $\boldsymbol{k}_i^{\mathcal{B}}$. Thus the basic equation can be written as

$$\boldsymbol{k}_i^{\mathcal{B}} = \boldsymbol{R}_{\mathcal{B}/\mathcal{L}}\boldsymbol{k}_i^{\mathcal{L}} \tag{4.8}$$
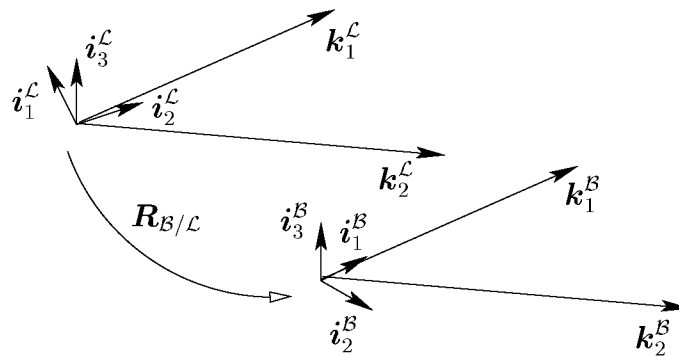


Figure 4.2.: GPS antenna vector in the local level and body frame respectively.

Let us take two arbitrary vectors (derived from three antennae's GPS coordinates) $\boldsymbol{k}_1^{\mathcal{L}}$ and $\boldsymbol{k}_2^{\mathcal{L}}$, and their representation in body frame $\boldsymbol{k}_1^{\mathcal{B}}$ and $\boldsymbol{k}_2^{\mathcal{B}}$ known from calibration measurements.

Taking the two vectors, two special coordinate frames $\mathcal{L}'$ and $\mathcal{B}'$ can be built as

$$i_1^{\mathcal{L}'} = \|k_1^{\mathcal{L}}\| \tag{4.9}$$

$$i_2^{\mathcal{L}'} = i_3^{\mathcal{L}'} \times i_1^{\mathcal{L}'} \tag{4.10}$$

$$i_3^{\mathcal{L}'} = \|k_1^{\mathcal{L}} \times k_2^{\mathcal{L}}\| \tag{4.11}$$

$$i_1^{\mathcal{B}'} = \|k_1^{\mathcal{B}}\| \tag{4.12}$$

$$i_2^{\mathcal{B}'} = i_3^{\mathcal{B}'} \times i_1^{\mathcal{B}'} \tag{4.13}$$

$$i_3^{\mathcal{B}'} = \|k_1^{\mathcal{B}} \times k_2^{\mathcal{B}}\| \tag{4.14}$$

and a third one ($\mathcal{I}$) as:

$$i_1^{\mathcal{I}} = \begin{pmatrix} 1 \\ 0 \\ 0 \end{pmatrix}, \qquad i_2^{\mathcal{I}} = \begin{pmatrix} 0 \\ 1 \\ 0 \end{pmatrix}, \qquad i_3^{\mathcal{I}} = \begin{pmatrix} 0 \\ 0 \\ 1 \end{pmatrix} \tag{4.15}$$

Thus a rotation matrix $L$ is calculated by

$$\forall i,j \in (1,2,3): \qquad l_{ij} = i_i^{\mathcal{I}} \cdot i_j^{\mathcal{L}'} \tag{4.16}$$

and the matrix $B$ analogously

$$\forall i,j \in (1,2,3): \qquad b_{ij} = i_i^{\mathcal{I}} \cdot i_j^{\mathcal{B}'} \tag{4.17}$$

The solution for the rotation matrix $R_{\mathcal{B}/\mathcal{L}}$ in equation (4.8) is therefore:

$$R_{\mathcal{B}/\mathcal{L}}^T = R_{\mathcal{L}/\mathcal{B}} = LB^T \tag{4.18}$$

The rotation matrix obtained by this direct method is subsequently used as an approximate solution for the least squares adjustment described below.

## 4.3.2. Least Squares Adjustment for One Epoch

If there are more than two vectors $k_i$ in Equation 4.8, an optimal rotation matrix can be sought by using a least squares (LSQ) adjustment. The attitude solution is calculated on a per epoch basis, independently from subsequent epochs except that they are linked trough the GPS ambiguity resolution process. The Equation (4.8) is taken as the observation equation and linearized:

$$k_i^{\mathcal{L}} - R_{\mathcal{L}/\mathcal{B}} k_i^{\mathcal{B}} = 0 \qquad = F(\vartheta) \tag{4.19}$$

$$\frac{\partial F}{\partial \vartheta} d\vartheta + \frac{\partial F}{\partial k_i} dk_i + F(\vartheta_0) = 0 \tag{4.20}$$

which, in matrix notation, becomes

$$A_i d\vartheta + B_i dk_i = w_i \quad \text{with} \quad C_i = \begin{pmatrix} C_{k_i^{\mathcal{L}}} & 0 \\ 0 & C_{k_i^{\mathcal{B}}} \end{pmatrix} \tag{4.21}$$

and with

$$B_i dk_i = \begin{pmatrix} I & -R_0 \end{pmatrix} \cdot \begin{pmatrix} dk_i^{\mathcal{L}} \\ dk_i^{\mathcal{B}} \end{pmatrix}$$

$$A_i = \left. \frac{\partial F}{\partial \vartheta} \right|_{\vartheta_0} = R_0 K_i^{\mathcal{B}}$$

$$w_i = -F(\vartheta_0) = -\left( k_i^{\mathcal{L}} - R_0 k_i^{\mathcal{B}} \right)$$

where $R_0$ is the approximate matrix $R_{\mathcal{L}/\mathcal{B}}$ calculated from two vectors (Equation 4.18), and $K_i^{\mathcal{B}}$ is a skew symmetric matrix containing the elements of $k_i^{\mathcal{B}}$ analogous to Equation A.9. The linearization and differentiation of the rotation matrix is described in detail in Appendix A.1. The index $i$ indicates vector number.

The matrix $A_i$ specifies the design matrix for the least squares estimation. The variances and covariances of the observations (in $C_{k_i^{\mathcal{L}}}$ and $C_{k_i^{\mathcal{B}}}$) form the weight matrix $P_i$ as follows:

$$P_i = \left( B_i C_i B_i^T \right)^{-1} = \left( C_{k_i^{\mathcal{L}}} + R_0 C_{k_i^{\mathcal{B}}} R_0^T \right)^{-1}$$

The variance for the vectors in the local level frame $\mathcal{L}$ is derived directly from the GPS solution accuracy, whereas for the body frame variances, values from the terrestrial lever arm measurements (Section 5.2) are used.

The vector $w$ is the absolute element. We thus get the familiar form for a LSQ adjustment (e.g. Schmid, 1977):

$$d\vartheta = \left( \sum_i A_i^T P_i A_i \right)^{-1} \cdot \sum_i A_i^T P_i w_i \tag{4.22}$$

As the observation equation (4.19) is not genuinely linear, the LSQ adjustment needs to be iterated a few times with $R_0$ improved as $= R_{\mathcal{L}/\mathcal{B}}(\vartheta_0 + d\vartheta)$.

The variances of the unknowns are given by

$$\sigma_\vartheta^2 = \sigma_0^2 q_{xx} \tag{4.23}$$

with $q_{xx}$ being the respective diagonal element of the inverse of the normal equation matrix $Q$.

$$Q = \left( \sum_i A_i^T P_i A_i \right)^{-1} \tag{4.24}$$

## 4.3.3. Impact of Antenna Configuration on Attitude Accuracy

As the GPS attitude estimation is computed using baseline vectors, its accuracy is dependent on the satellite and the antenna vector geometry. Comp (1993) finds the antenna configuration to be optimal in the sense of minimizing attitude errors, when the antennae are arranged to build orthogonal vectors. Due to the fact, that the GPS multi antennae system is used on an airplane, the locations suitable to place the antennae are very limited. This makes the optimization of the antenna configuration into strict orthogonality virtually impossible.

Another quite simple strategy for diminishing GPS attitude error is to increase the baseline length as much as possible. The attitude or pointing error $\sigma_\vartheta$ depends directly on the differential ranging error $\sigma_r$ and the baseline length $l$ according to the formula (Comp, 1993):

$$\sigma_\vartheta = \frac{\sigma_r}{l} \qquad (4.25)$$
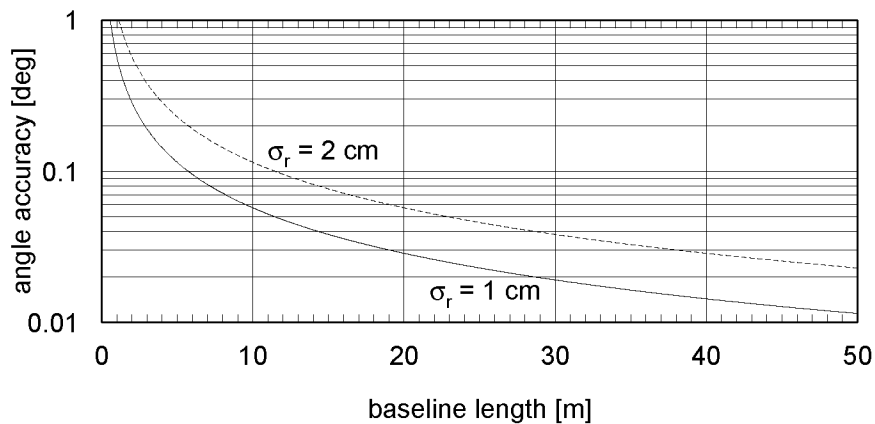


Figure 4.3.: Accuracy of GPS attitude determination as a function of baseline length.

The accuracy of baseline determination is known to be on the order of 0.01 m. Figure 4.3 shows the angle accuracy $\sigma_\vartheta$ as a function of baseline length $l$ for $\sigma_r = 0.01$ m (solid line) and $\sigma_r = 0.02$ m (dotted line). One clearly sees that in order to reach an angle accuracy of 0.01°, a baseline greater than 50 m would be needed. The realized baseline lengths on the Twin Otter are about 5–10 m, which corresponds to an expected angular accuracy of 0.05–0.1°.

The antenna configuration described in section 2.3.2 was chosen to have the vectors as orthogonal as possible, and to increase baseline length while not compromising too much of rigidity. For example Cannon and Sun (1996) mount their antennae on the wingtips, yet the wing flexure there they find to be around 0.12 m. For the laser flights, the antennae were mounted on the engines, which is a compromise between less flexing effect and shorter baseline length.

# 4.4. Combining GPS Attitude with INS Attitude

## 4.4.1. Characteristics of GPS and INS Attitude Determination

Determining attitude angles of a platform by a GPS antenna array and by INS are two fundamentally different concepts. As indicated by Equation 4.25, the GPS multi antenna array attitude can be provided only with limited accuracy due to antenna placement constraints. On the other hand, an inertial system measures directly the angular rotation rate with some sort of gyro system. For an overview of different gyro mechanisms in use refer to e.g. Merhav (1996).

The main characteristics of both concepts are listed in Table 4.1. By means of GPS

| Concept | Observable | A priori known | Type | Current problems |
|---|---|---|---|---|
| Ranging from satellites to multiple antenna array | Ranges (vectors between antennae) | Satellite positions, body frame antenna coordinates | Global, non-autonomous, medium accuracy | Stability of antenna array, limited baseline length |
| Inertial techniques | Specific force, angular velocity | Initial position, initial attitude, earth rotation rate, gravity field | Global, autonomous, accuracy dependent on time | Gyro drifts, deflection of the vertical, random walk |

Table 4.1.: Main characteristics of attitude determination by the GPS and the INS concept (modified after Škaloud, 1999).

multi antenna array attitude is given with poor accuracy and low frequency, yet it is time independent. By means of INS, attitude is given with high accuracy and frequency, but the solution is subject to drift effects, random walk and deflection of the vertical.

The integration of GPS and INS has been studied by many researchers (e.g. Schwarz and Wei, 1994; Söhne et al., 1994; Mohamed, 1999). Most approaches involve some

sort of Kalman filtering coalescing a navigation grade INS and one single GPS receiver on the moving platform.

One major drawback of Kalman filtering is its dependence on good knowledge of a priori filter statistics and on the weak observability of state vector components (Mohamed, 1999). The tuning of the input noise parameters is the main difficulty for using the filter algorithm (Bagnaschi et al., 1993).

With our setup, two independent attitude solutions are available with properties complementing each other. Thus the approach is to use the GPS attitude as an estimate of the local INS drift offset and slope, and correct the INS data locally with this drift information. This has several advantages:

- the misalignment between GPS antenna body frame and INS body frame is inherently taken care of,

- as the laser lines span over a short period of time ($\approx 60\,\text{s}$), the gyro drifts stay locally small and approximately linear (example drift: 3 deg/hr $\approx$ 0.05 deg/min),

- the estimation of the local bias involves not only past observations (as in a Kalman filter) but all observations available for the line,

- time dependent Kalman filter degradation due to GPS outage does not lag behind on re-locking the satellites.

## 4.4.2.   INS Specific Error Sources

The attitude determination using a strapdown INS is a by-product of INS position determination (e.g. Merhav, 1996). The measured rotation rates cannot just be integrated with time around the body coordinate system axes. For a strapdown system, the following relation between the Euler angle rates $\dot{\vartheta}_1, \dot{\vartheta}_2, \dot{\vartheta}_3$ and the measured rotation rates $\boldsymbol{\omega}^{\mathcal{B}}$ holds (Farrell, 1976):

$$\boldsymbol{\omega}^{\mathcal{B}} = \begin{pmatrix} \dot{\vartheta}_1 - \dot{\vartheta}_3 \sin \vartheta_2 \\ \dot{\vartheta}_2 \cos \vartheta_1 + \dot{\vartheta}_3 \cos \vartheta_2 \sin \vartheta_1 \\ \dot{\vartheta}_3 \cos \vartheta_2 \cos \vartheta_1 - \dot{\vartheta}_2 \sin \vartheta_1 \end{pmatrix} \qquad (4.26)$$

If Equation 4.26 is solved for the Euler angle rates, we get the following differential equations:

$$\begin{pmatrix} \dot{\vartheta}_1 \\ \dot{\vartheta}_2 \\ \dot{\vartheta}_3 \end{pmatrix} = \begin{pmatrix} \omega_1 + \tan \vartheta_2 (\omega_2 \sin \vartheta_1 + \omega_3 \cos \vartheta_1) \\ \omega_2 \cos \vartheta_1 - \omega_3 \sin \vartheta_1 \\ \frac{1}{\cos \vartheta_1} (\omega_2 \sin \vartheta_1 + \omega_3 \cos \vartheta_1) \end{pmatrix} \qquad (4.27)$$

The Euler angles are then updated by integrating the rates as:

$$\boldsymbol{\vartheta} = \int \dot{\boldsymbol{\vartheta}} dt \qquad (4.28)$$

Because the angle rates have to be integrated over time, the resulting angles suffer a degradation over time. Additionally, a gyro zero offset error in one single gyro sensor $\omega_i$ propagates into more than one Euler angle rate. This holds true especially for the body frame azimuth rate $\omega_3$ and the body frame pitch rate $\omega_2$.

### Drift and Random Walk

A constant zero offset of a gyro sensor produces a constant drift in the attitude angles. This offset is usually estimated as an additional state in the Kalman filter when the integration of the attitude rates is done. Such an offset is not necessarily constant, but may show sensitivity to temperature change or acceleration. How well these drift effects are mitigated depends on the system manufacturer's calibration. Inertial systems often have to be recalibrated after a certain time (Lipman, 1992).

Assume a gyro signal is contaminated with white noise. An integration of white noise does not yield a normally distributed noise, but a bias which randomly walks away. This effect is known as random walk.

The quality of Gyro sensors is thus often given in drift rate, i.e. it is defined to what extent the computed angles remain stable.

### Misalignment of GPS, INS and Laser Subsystems

As described in section 4.2.1, each subsystem defines a different realization of the body frame. These misalignments are accounted for in two different ways:

- the misalignment between the GPS and iMAR INS is inherently taken care of by the integration process described below,

- the boresight misalignment between the GPS and the laser system is estimated by a self-calibration technique described in Section 5.3,

- the misalignment between the GPS/iMAR combination and the Applanix System is estimated by comparing the respective attitude angle solutions.

## 4.4.3. Integrating GPS and INS Attitude by Local Polynomial Correction

The INS attitude drift parameters are estimated by a polynomial regression for the time window $[t_s, t_e]$ of each single laser scan line.

Instead of using ordinary polynomials of the form $a_0 + a_1 x + a_2 x^2 + \ldots$, Chebyshev polynomials are used (e.g. Bronštejn and Semendjaev, 1987, p. 752). It is well known that the ordinary polynomial basis $1, x, x^2, \ldots$ gives terribly ill-conditioned matrices. This is because the ordinary basis is far from orthogonal.

Thus the regression model is written as

$$\vartheta_{\mathrm{GPS}}(t) - \vartheta_{\mathrm{iMAR}}(t) = f(t) + e \tag{4.29}$$

and fitted by least squares, where $e$ are error misfits. The function $f(t)$ is constructed using Chebyshev polynomials (Bronštejn and Semendjaev, 1987) with the time window $[t_s, t_e]$ scaled to $[-1, 1]$:

$$f(t) = a_0 T_0 + a_1 T_1 + \ldots \tag{4.30}$$

The number of model parameters $u$, starting at one, is iteratively increased until the reduction in variance of the model residuals is not significant at the confidence level $\alpha$. The significance of the improvement in model misfit residuals squared $\left( \frac{[pee]}{n-u} \right)$ is evaluated by an $F$ test. The regression is realized in the GMT software of Wessel and Smith (1998).

The regression additionally is made robust by iteratively reweighting the data to reduce the influence of outliers. The weight is based on the Median Absolute Deviation and a formula from Huber (1964), and is 95% efficient when the model residuals have an outlier-free normal distribution. This means that the influence of outliers is reduced only slightly at each iteration; consequently the reduction in the variance is not very significant. As the procedure needs a few iterations to successfully attenuate their effect, the significance level of the $F$ test must be kept low (Wessel and Smith, 1998).

This estimated drift function is subsequently applied to the INS data to yield the combined attitude angles

$$\vartheta_{\mathrm{comb}}(t) = \vartheta_{\mathrm{iMAR}}(t) + f(t) \tag{4.31}$$

Figure 4.4 shows an example of the roll angle difference $\phi_{\mathrm{GPS}}(t) - \phi_{\mathrm{iMAR}}(t)$ for one scan line lasting about 80 s. In this case, a linear regression fits sufficiently the IMU drift effect. This means that the reduction in variance achieved by increasing the number of terms in the model is not significant at a degree of confidence of 68%. This makes sense as the remaining model misfit is smaller than the GPS attitude accuracy.

Looking at the pitch angle of the same strip, the iMAR pitch angle apparently suffers stronger drift effects (Figure 4.5). In this case, a 7 parameter polynomial was used to fit the drift effects.

The yaw angle could again be modeled using a linear approach (Figure 4.6). The magnitude of the drift corrections is up to 3° and is not constant for all scan lines. Table 4.2 gives an overview of the drift correction results.
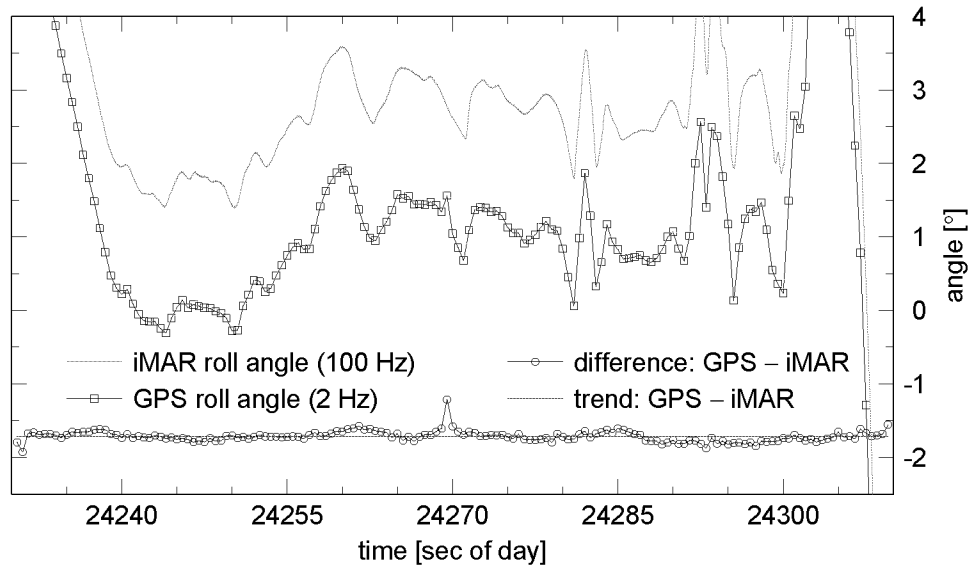
Figure 4.4.: Roll angle of GPS attitude solution and iMAR output for one laser scan line. The difference GPS minus iMAR is subject to a trend estimation.
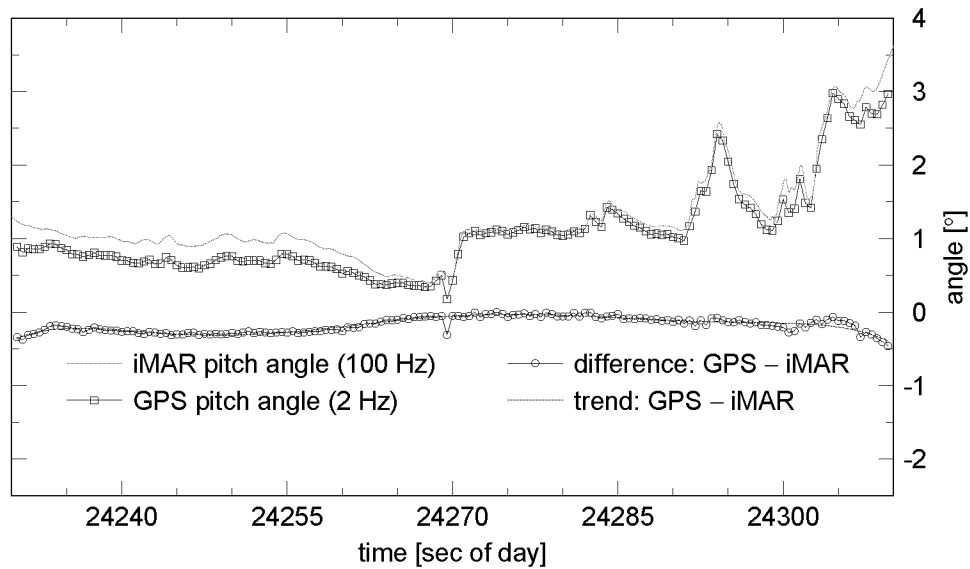


Figure 4.5.: Pitch angle of GPS attitude solution and iMAR output for one laser scan line. A 7 parameter polynomial was used to fit the drift effects.

Favey, E., 2001. *Investigation and Improvement of Airborne Laser Scanning Technique for Monitoring Surface Elevation Changes of Glaciers*. ETH Zurich, Diss. No. 14045
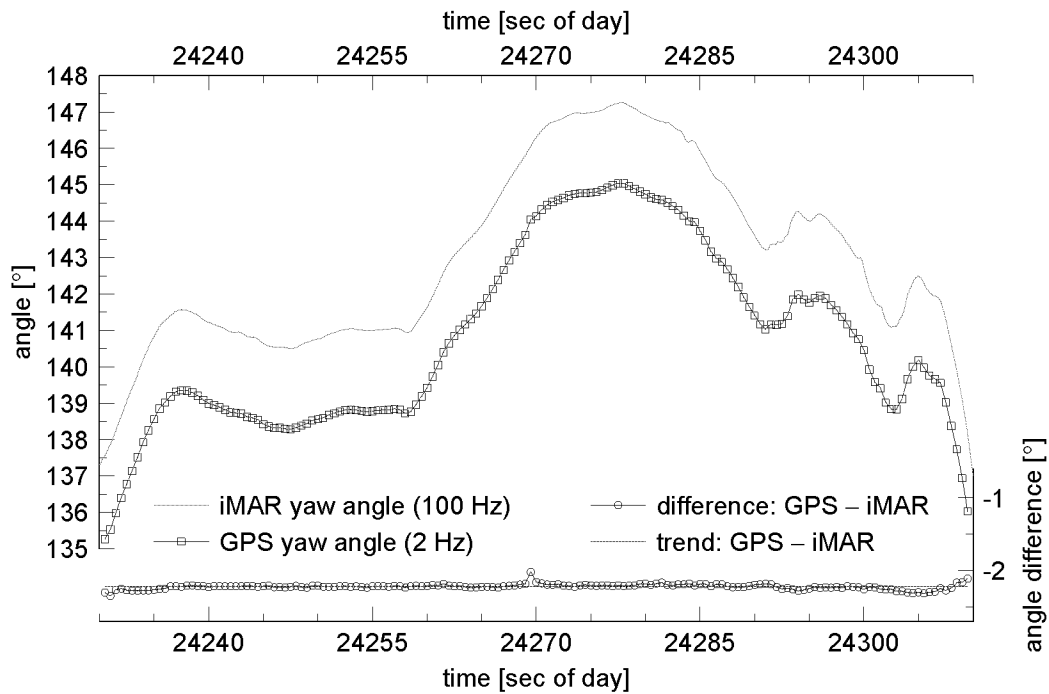
Figure 4.6.: Yaw angle of GPS attitude solution and iMAR output for one laser scan
line. The trend function is a linear fit. The outlier just before second
24270 appears in all three angular components, and is due to a bad GPS
attitude solution for that epoch.

| strip | | roll | | | pitch | | | yaw | | |
| # | $n$ | $u$ | $\tilde{a}_0$ [°] | $\sqrt{\frac{[pee]}{n-u}}$ | $u$ | $\tilde{a}_0$ [°] | $\sqrt{\frac{[pee]}{n-u}}$ | $u$ | $\tilde{a}_0$ [°] | $\sqrt{\frac{[pee]}{n-u}}$ |
|---|---|---|---|---|---|---|---|---|---|---|
| 9903 | 219 | 1 | 2.89 | 0.044 | 6 | −0.57 | 0.040 | 1 | −1.82 | 0.042 |
| 9905 | 239 | 1 | 2.73 | 0.052 | 2 | −0.65 | 0.099 | 1 | −1.90 | 0.026 |
| 9907 | 239 | 1 | 2.65 | 0.041 | 2 | −0.78 | 0.048 | 1 | −2.07 | 0.035 |
| 9904 | 159 | 1 | −1.72 | 0.064 | 7 | −0.18 | 0.033 | 1 | −2.22 | 0.030 |
| 9906 | 159 | 2 | −1.68 | 0.074 | 1 | −0.11 | 0.081 | 2 | −2.31 | 0.048 |
| 9909 | 105 | 1 | −1.65 | 0.058 | 1 | −0.96 | 0.127 | 1 | −2.68 | 0.055 |
| 9910 | 101 | 1 | −2.08 | 0.095 | 3 | −0.80 | 0.040 | 3 | −2.26 | 0.037 |
| 9911 | 101 | 3 | −2.00 | 0.038 | 3 | −1.16 | 0.040 | 1 | −2.26 | 0.049 |
| 9805 | 479 | 1 | 2.46 | 0.090 | 4 | −0.88 | 0.103 | 1 | −2.37 | 0.088 |
| 9808 | 439 | 2 | 2.46 | 0.079 | 5 | −0.82 | 0.097 | 1 | −1.99 | 0.117 |
| 9810 | 399 | 1 | 2.68 | 0.083 | 1 | −0.97 | 0.190 | 2 | −2.02 | 0.132 |
| 9809 | 443 | 5 | −1.06 | 0.140 | 4 | −0.66 | 0.386 | 2 | −2.01 | 0.198 |
| 9811 | 319 | 1 | −1.24 | 0.163 | 5 | −0.27 | 0.214 | 6 | −2.21 | 0.119 |
| 9812 | 239 | 1 | 2.64 | 0.142 | 3 | −0.66 | 0.127 | 1 | −2.17 | 0.146 |
| 9813 | 319 | 3 | −1.54 | 0.057 | 1 | −0.68 | 0.245 | 1 | −2.18 | 0.096 |
| 9814 | 319 | 3 | 2.62 | 0.061 | 2 | −0.62 | 0.103 | 2 | −1.93 | 0.100 |

Table 4.2.: Table with attitude angle offset and drift estimation. $n$ is the number of observations for that strip. $u$ stands for the number of model parameters found to be significant. $\tilde{a}_0$ denotes the mean angle offset for the respective strip, which is supplied to give an idea of the variational behavior. The third column shows the model misfit residuals squared, which is on the order of the GPS attitude accuracy.

The results for the strips of 1998 appear to be worse than those of 1999. This is on one hand due to the fact, that the 1998 flight was very turbulent because of winds up to 20 knots. On the other hand, all but one short GPS baseline of 1998 had one remaining unresolved ambiguity (cf. Table 3.1), which consequently degrades the GPS attitude solution.

## 4.4.4. Comparison of Integrated Attitude Solution with a Commercial POS Solution

As the attitude during the 1999 laser flight was determined independently by the combination GPS/iMAR and an Applanix INS/DGPS system. The results of the combined attitude determination can thus be compared with the result of the commercial Applanix solution.

The commercial solution uses an integrated INS/DGPS Kalman filter solution and high accuracy gyros with a drift on the order of $1°/h$ (manufacturer's specification sheet). The roll angle presented in Figure 4.4 from the same flight line is compared with the Applanix solution in Figure 4.7. The good coincidence can clearly be seen as well as the displacement of the two curves by the GPS and Applanix body frames' misalignment.

The two other attitude angles' comparison is shown in Figures 4.8 and 4.9. The comparison differences show a short term dynamic behavior which can occur due to various reasons:

- the polynomial approach is unable to model. On one hand this would require a higher order polynomial without a significant decrease in model misfit residuals squared; on the other hand, the magnitude of this dynamic behavior is on the order of the GPS attitude accuracy.

- the Kalman filter approach of the Applanix system might lag behind in a dynamic environment, depending on how the gain is defined.

Without knowledge of a 'true' attitude angle, it is difficult to attribute these effects to a single system.

Table 4.3 gives a statistical overview of the comparison of all scan lines of the summer 1999. The misalignment offset varies with $\pm 0.05°$, as it mainly depends on the GPS angle accuracy.

Parts of the rather high standard deviation of the order of $0.02$–$0.04°$ are due to the oscillations as seen in Figure 4.7, and due to the different dynamic response of the systems as described above.

Favey, E., 2001. *Investigation and Improvement of Airborne Laser Scanning Technique for Monitoring Surface Elevation Changes of Glaciers.* ETH Zurich, Diss. No. 14045
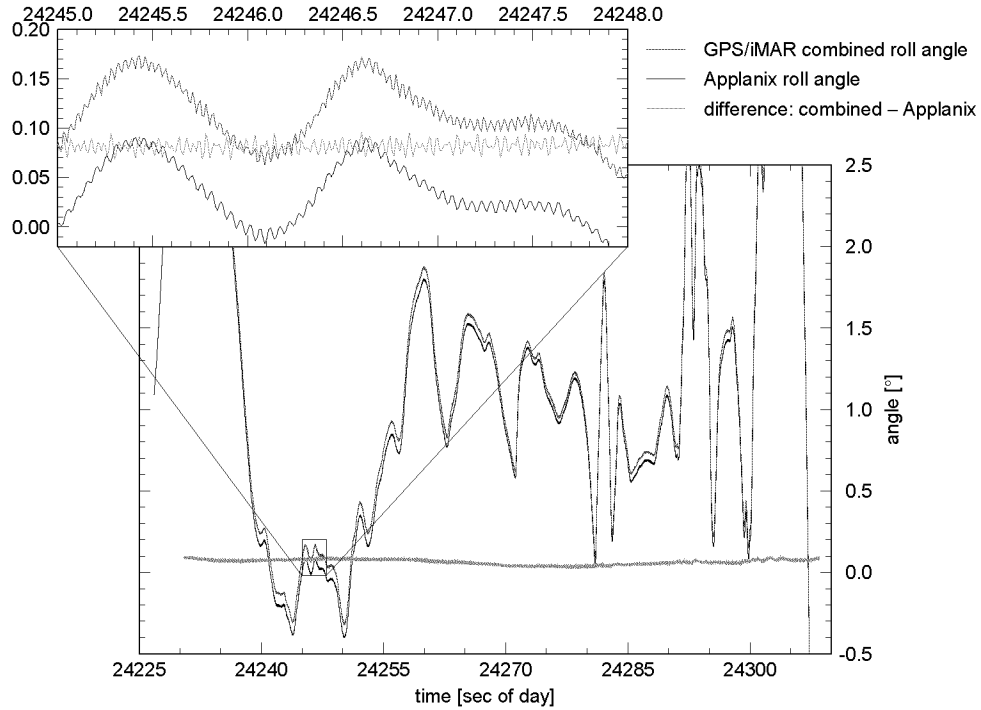
Figure 4.7.: Roll angle of GPS/iMAR combined attitude solution and Applanix solution for one laser scan line. The green line shows the difference of these two independent attitude solutions. Note the two oscillations on the combined and the Applanix roll angle respectively, and the beat on the difference.
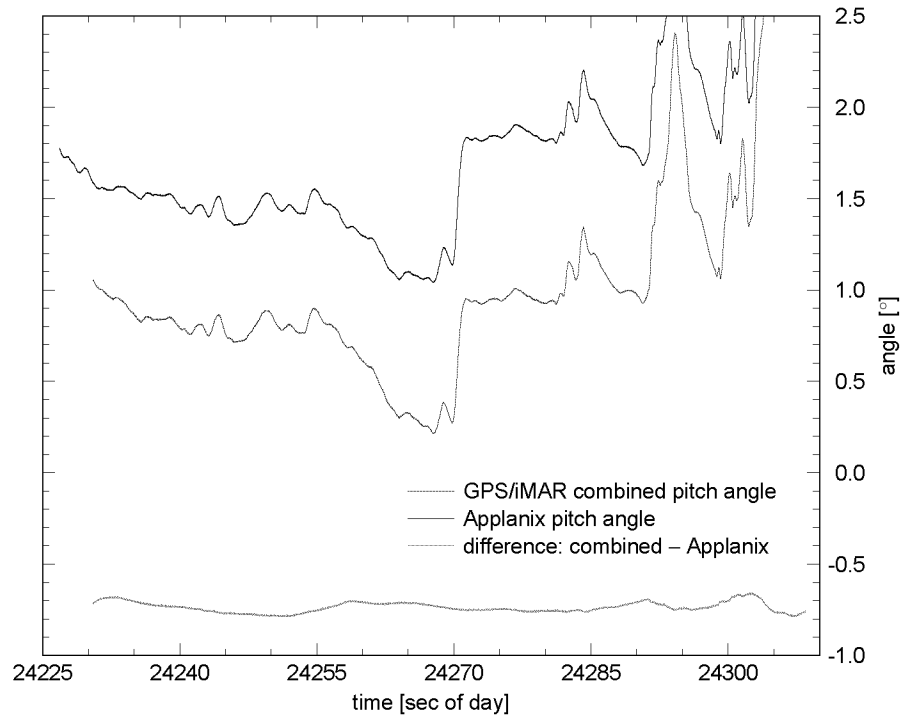
Figure 4.8.: Pitch angle of GPS/iMAR combined attitude solution and Applanix
solution for one laser scan line. The green line shows the difference of
these two independent attitude solutions. The remaining unmodelled
features in the difference are on the order of the GPS attitude accuracy.
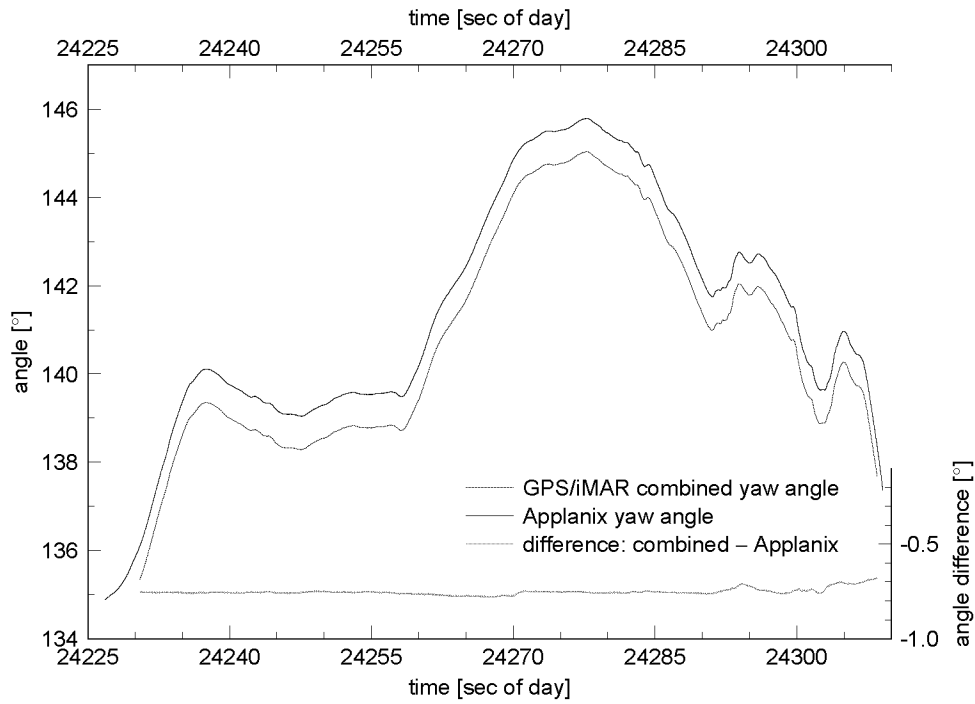
Figure 4.9.: Yaw angle of GPS/iMAR combined attitude solution and Applanix so-
lution for one laser scan line. The green line shows the difference of
these two independent attitude solutions.

Favey, E., 2001. *Investigation and Improvement of Airborne Laser Scanning Technique for Monitoring Surface Elevation Changes of Glaciers.* ETH Zurich, Diss. No. 14045

| strip # | 03 | 04 | 05 | 06 | 07 | 09 | 10 | 11 |
|---|---|---|---|---|---|---|---|---|
| observation count | 10800 | 7800 | 11800 | 7800 | 11800 | 5100 | 4900 | 4900 |

roll angle difference $\phi_{\text{comb}} - \phi_{\text{appl}}$

| strip | min | max | mean | stddev |
|---|---|---|---|---|
| 03 | 0.171 | 0.219 | 0.191 | 0.007 |
| 04 | 0.019 | 0.102 | 0.065 | 0.017 |
| 05 | −0.001 | 0.065 | 0.031 | 0.012 |
| 06 | 0.001 | 0.175 | 0.103 | 0.036 |
| 07 | −0.052 | 0.090 | 0.029 | 0.031 |
| 09 | 0.035 | 0.138 | 0.092 | 0.023 |
| 10 | 0.005 | 0.107 | 0.074 | 0.023 |
| 11 | 0.058 | 0.156 | 0.097 | 0.020 |

pitch angle difference $\theta_{\text{comb}} - \theta_{\text{appl}}$

| strip | min | max | mean | stddev |
|---|---|---|---|---|
| 03 | −0.785 | −0.543 | −0.693 | 0.047 |
| 04 | −0.789 | −0.658 | −0.736 | 0.028 |
| 05 | −0.984 | −0.485 | −0.670 | 0.113 |
| 06 | −0.879 | −0.557 | −0.731 | 0.087 |
| 07 | −0.843 | −0.608 | −0.706 | 0.050 |
| 09 | −0.914 | −0.527 | −0.752 | 0.111 |
| 10 | −0.844 | −0.651 | −0.702 | 0.035 |
| 11 | −0.838 | −0.691 | −0.745 | 0.037 |

yaw angle difference $\psi_{\text{comb}} - \psi_{\text{appl}}$

| strip | min | max | mean | stddev |
|---|---|---|---|---|
| 03 | −0.705 | −0.596 | −0.629 | 0.021 |
| 04 | −0.781 | −0.677 | −0.752 | 0.017 |
| 05 | −0.758 | −0.656 | −0.700 | 0.021 |
| 06 | −0.800 | −0.661 | −0.716 | 0.029 |
| 07 | −0.815 | −0.658 | −0.718 | 0.025 |
| 09 | −0.753 | −0.631 | −0.679 | 0.034 |
| 10 | −0.774 | −0.680 | −0.732 | 0.022 |
| 11 | −0.775 | −0.643 | −0.700 | 0.038 |

Table 4.3.: Comparison of the attitude solution of GPS/iMAR combined vs. Applanix solution. The mean values correspond to the misalignment offset between the two IMU coordinate frames.

## 4.5. Inertial System Placement Considerations

The two inertial systems from iMAR and Applanix were placed at different locations within the airplane during the same flight. The Applanix system was mounted directly on top of the scanning mirror holding frame (see Figure 2.6), whereas the iMAR system was placed at the center of mass of the airplane on the floor (Figure 2.5).

The zoomed view in Figure 4.7 shows clearly two distinct oscillations, one on the angle of the Applanix system, and one on the angle of the combined GPS/iMar solution. A Fourier transform of the dataset of Figure 4.7 is shown in Figure 4.10. The Applanix system's oscillation is at 20 Hz. This corresponds to the laser scan
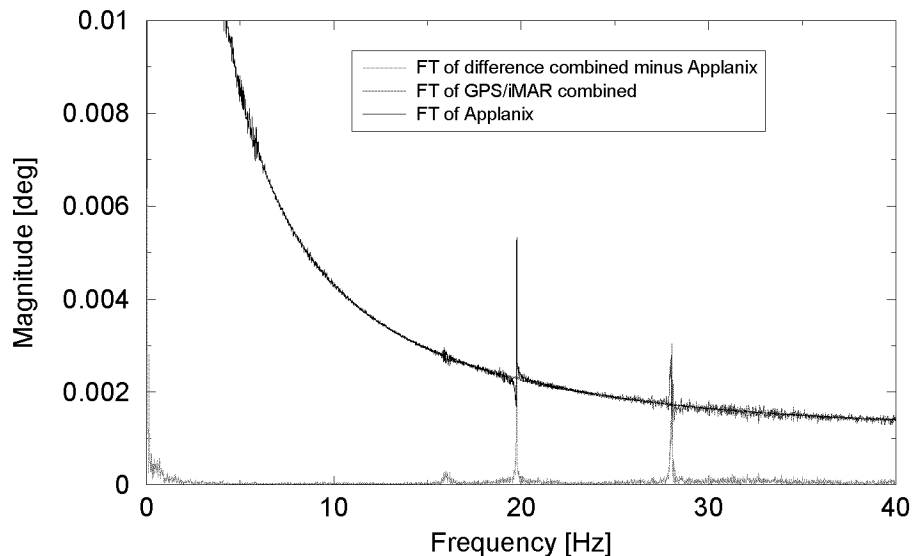


Figure 4.10.: Power spectrum of the roll angle data shown in Figure 4.7. The frequency of 20 Hz is present only in the Applanix data, whereas the frequency of 28 Hz shows up only in the combined solution.

mirror rotation rate. As the sensor is mounted right on top of the mirror, it is evident that this frequency corresponds to this cause.

The iMAR system on the other hand—mounted on the aircraft floor—does not 'see' this mirror frequency. Yet it sees a different oscillation at 28 Hz. This frequency corresponds to the aircraft propellers' rotation rate. It is yet unclear, why the Applanix system lacks this second frequency, as it is not isolated from the aircraft vibrations. The amplitude of both vibrations remains small, e.g. the magnitude of the frequencies is on the order of $0.005°$.

The differential movements between the IMU and the laser unit is rather difficult to overcome. Mounting the IMU as closely and rigidly as possible to the remote sensing hardware is advisable (Škaloud, 1999). Yet this was only possible in the

case of the Applanix system. The iMAR system's physical dimensions were too large to be included in the laser hardware body.

# 5. Acquiring Inner Orientation Parameters

## 5.1. Introduction

Critical elements in the georeferencing observation equation (2.16) are the inner orientation parameters such as

- the lever arm between the scanner point of reference and the GPS antenna phase center, and

- the misalignment rotation matrix between the scanner and the body frame (boresight misalignment).

These parameters can affect the georeferencing of the laser data systematically, yet they are not trivial to determine. They are usually assumed to remain constant during the whole flight, tough they are subject to vibrations and aircraft deformation to a small degree.

The lever arms and the position of all GPS antennae was measured with conventional methods on the ground. In a first part, the emergence of the body frame coordinates for our flight setup is described.

The second part of this chapter deals with an approach to estimate the boresight misalignment angles directly from the laser scanner data using a self-calibration technique.

## 5.2. Lever Arms and Body Frame

The laser scanner reference point is the center of the scanning mirror (Figure 2.8). The position of this reference point related to the GPS antenna phase center has to be known very accurately, as an error in this value propagates linearly into the final ground position. Using the fiducial points of the front aerial camera, an aircraft body frame was realized by terrestrial measurements, including the locations of the GPS antennae (REAR, LEICA, FWDA) on the fuselage (Geiger et al., 1997).
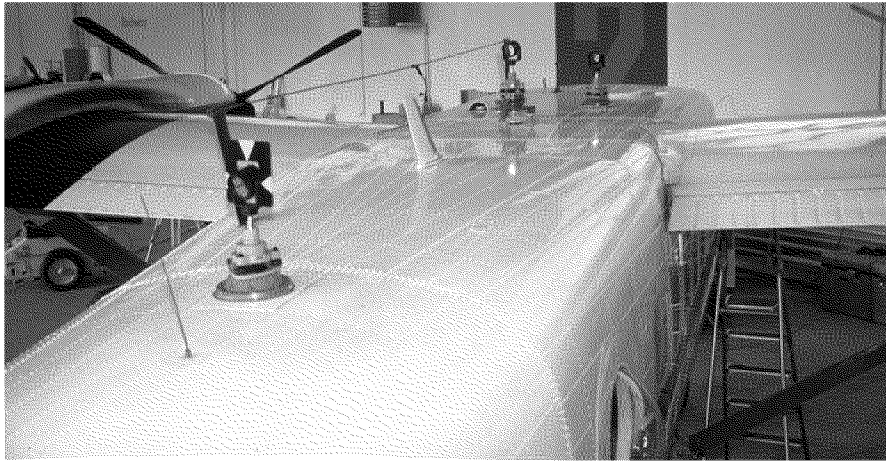
Figure 5.1.: Ground measurement of antenna positions using a theodolite.

The relation of the GPS antennae used for positioning to the aerial camera frames and fiducial marks were measured using a theodolite setup in the hangar. For this purpose, the aircraft was jacked up and levelled out (i.e. the fiducial planes of the two aerial cameras were made to be level). The coordinates of all the points of interest on and in the aircraft were adjusted with an unconstrained network using an LSQ-software for terrestrial measurements. The standard deviation from the adjustment for the 3D point coordinates is better than 1 mm.



Figure 5.2.: Jacked up aircraft during the lever arms measurements.

As the laser scanner is mounted exactly onto the same spacer as the aerial camera; the relation of the spacer screw holes to the fiducial points as well as to the scanner reference point was determined.

At the time of the terrestrial measurements, the antenna array of single frequency antennae (FRNT, LEFT, RGHT, TAIL) used solely for attitude determination were

not yet mounted on the aircraft. They were measured by placing the airplane on the taxiway and letting all GPS receivers log data simultaneously. The body frame coordinates of the single frequency receivers could then be derived from the known coordinates of the antennae measured by theodolite. This was done using a static DGPS evaluation, where the REAR, LEICA, and FWDB coordinates were used as reference.

The antenna FWDA was replaced by a different antenna FWDB, mounted at the same location in the winter of 1998. The coordinates of FWDB were derived from FWDA's coordinates by measuring its local displacement at the mount point. The lever arm between FWDB, which was connected to the Applanix system and the laser scanning mirror gets estimated by the Applanix software as a Kalman filter state. A comparison of the commercial software's solution and the terrestrially measured lever arms yielded an offset in flight direction $x^{\mathcal{B}}$ of 8.5 cm, 2 cm in $y^{\mathcal{B}}$ and 0.3 cm in the height component $z^{\mathcal{B}}$. These results are not significant according to the standard deviation of the Kalman filter estimation. Still it shows a good match within the expected 1 cm accuracy apart from the rather big offset in $x^{\mathcal{B}}$.

# 5.3.    Handling Boresight Misalignment by Self-Calibration

## 5.3.1.    Approaches to Calibrate Misalignment from Flight Data

As opposed to the lever arms, the misalignment angles between the body frame $\mathcal{B}$ and the laser frame $\mathcal{S}$ is rather difficult to measure directly. Assume a geolocation accuracy of 10 cm is wanted at a flying altitude of 700 m. Translated to a 1 m baseline (about the size of the laser scanner carrying frame), this would mean to measure its orientation respective to the aircraft frame with an accuracy of 0.1 mm.

The ScaLARS II laser scanner uses a palmer scan mechanism, which draws ellipse-like patterns to the ground (Figure 5.3). This special pattern has been exploited by Thiel and Wehr (1999) to manually determine the misalignment angles directly from the laser data itself. As the airplane moves on, the same region on earth is scanned twice, once within the forward half of the elliptical pattern, and once on the backward half. Theoretically, if the very same spot on earth was hit, or the target region is a horizontal plane both height measurements should be of the same magnitude. A pitch angle offset $d\theta$ shifts the pattern in flight direction, lifting the forward and lowering the backward scan at the center line. The pitch angle offset can be derived directly from the height difference $dh$ and the diameter $d$ of the ellipse in flight direction as:

$$d\theta = \arcsin\left(\frac{dh}{d}\right) \tag{5.1}$$
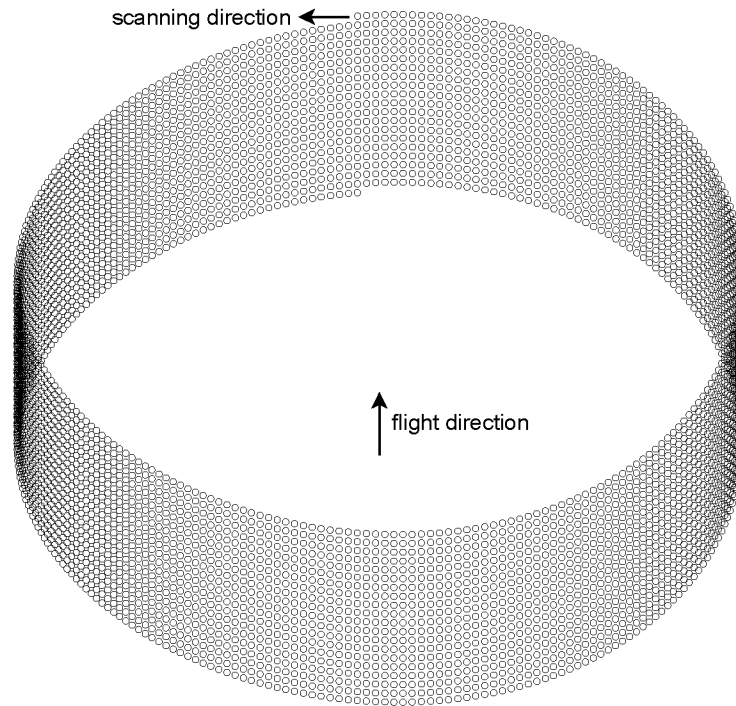
Figure 5.3.: Scan Pattern of the Palmer Scanner for 20 mirror revolutions (1 s at 20 Hz). It can be seen clearly that if the airplane translates in flight direction, the same region on earth is scanned a second time by the part of the ellipse behind the major axis. Note also the denser measurements towards the sides of the swath.

The yaw and roll angle offsets $d\psi$ and $d\phi$ are derived from horizontal displacements in the reflectance intensity data of well identifiable objects like houses, street intersections or house corners. They are calculated as

$$d\psi = \arcsin\left(\frac{dn}{2b}\right) \tag{5.2}$$

$$d\phi = \arcsin\left(\frac{do}{2r}\right) \tag{5.3}$$

where

$dn$ : observed horizontal displacement lateral to the flight direction at the center of the swath.
$b$ : semi-axis of ellipse pattern in flight direction.
$do$ : observed swath overlap displacement lateral to the flight direction. This works only, if the overlapping lines have been flown in anti-parallel direction.
$r$ : slant laser range.

This method of Thiel and Wehr (1999) has several drawbacks for the glacier case:

- the objects to match for the roll and pitch angle offsets have to be found manually,

- this method may be suitable for urban areas with many well identifiable objects in the rather coarse intensity data; yet in areas like glaciers or snow fields, it is rather difficult to identify objects in the intensity data to match,

- the roll offset angle cannot be determined with parallel lines flown in the same direction.

An approach of matching triangulated irregular network (TIN) patches of strip overlaps is followed by Maas (2000). It is a variant of the least squares matching (LSM) technique applied regularly by photogrammetrists for the establishment of correspondences between images from different viewing points, and even proposed to apply to gridded DEM laser scanner data (Kilian, 1994). Using TIN structures for matching tries to avoid the drawbacks of interpolating the measurements to a regular grid. This means that it is possible to exclude regions of occlusions by deselecting triangles identified as bridging gaps due to their longish shape as well as their steepness. Especially in flat areas, this method can only be used to determine a vertical shift parameter, as the patch contrast in the height data is too small. If reflectance intensities are available, they may complement the height data for the determination of horizontal shift parameters.

This method could be used to automate the method of Thiel and Wehr (1999) for angle offset determination. Yet its applicability to rather texture-less data (in height as well as reflectance intensity) of non urban areas needs to be further investigated.

For the method to succeed, each patch needs to provide enough contrast for the matching to work. In case described by Maas (2000), the patch centers were chosen manually, and needed to contain a uniform or orthogonal distribution of significant gradients for the match to be accepted. Additionally, his method is sensitive to noise of the laser data or insufficient sampling of the contrast features.

## 5.3.2.   Influence of Boresight Misalignment on the Laser Height

In this section, an approach is presented to estimate the boresight misalignment off-set angles directly from the laser distance measurements using a least squares (LSQ) adjustment. This self-calibration technique is based on the assumption, that laser ground points from different shots, that are close together (within a few meters) more or less have the same height, as the glacier area is rather a continuous, planar area. In this case, the plane from one scan subset $A$ should have the same characteristics as the plane derived from an adjacent scan subset $B$ covering the same area. Examples of such subsets are strip overlap areas or portions of the forward and backward scan of the palmer scanning pattern (Figure 5.3) of a selected region. The difference is then functionally modeled to be an error induced by the attitude angles.

The general approach is described by the function

$$F(\boldsymbol{l}, \boldsymbol{u}) = z_A(\boldsymbol{l}, \boldsymbol{u})\big|_{x_0, y_0} - z_B(\boldsymbol{l}, \boldsymbol{u})\big|_{x_0, y_0} = 0 \qquad (5.4)$$

where

$\boldsymbol{l}$ : Observations, like position, attitude angles
$\boldsymbol{u}$ : Unknown angle offsets for roll, pitch and yaw
$z_A$ : height, interpolated from a local subset $A$ of points
$z_B$ : height, interpolated from another local subset $B$ of points
$x_0, y_0$: location of interpolation

The subsets $A$ and $B$ are selected differently for each angle's specific offset determination needs. For the pitch angle offset, the subsets $A$ and $B$ are selected from the forward and backward scan in a way, that their current location on ground is the same. The height difference $dh$ then corresponds to Equation 5.1, where the diameter can also be viewed as $d = r_a \sin \alpha_a + r_b \sin \alpha_b$ with $r$ and $\alpha$ being the slant range and the scan angle respectively (Figure 5.4).

$$dh = (r_a \sin \alpha_a + r_b \sin \alpha_b) \sin d\theta \qquad (5.5)$$

The roll angle can be determined from the height difference from overlapping strips flown parallel in the same direction (Figure 5.4). In this case, the roll angle offset is
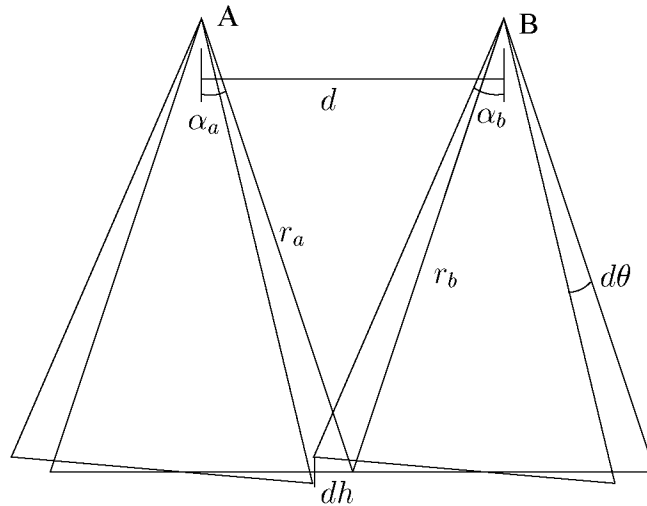
Figure 5.4.: Pitch angle determination from forward and backward scan. The sub-
              sets $A$ and $B$ are selected from the same strip and need to have a time
              lag of at least 2 seconds. This same figure also explains the roll angle
              determination from strip overlap of lines flown in parallel direction. In
              this case the subsets $A$ and $B$ need to be from different strips.

determined analogously to Equation 5.5, but $d = r_a \sin \alpha_a + r_b \sin \alpha_b$ in this case is
the distance between the strips' trajectories.

$$dh = (r_a \sin \alpha_a + r_b \sin \alpha_b) \sin d\phi \qquad (5.6)$$

Getting the yaw angle from the height data is only possible, if there are large planar
tilted areas with positive and negative slopes within the scanned region, such as a
ridge or a V-formed feature. With the scanning angle $\alpha$, the slope inclination angle
$\beta$, and the angle $\gamma$ between the azimuth of the scan direction and the azimuth of
the slope gradient (Figure 5.5) we get:

$$dh = (r_a \sin \alpha_a + r_b \sin \alpha_b) \tan \beta \cos \gamma \sin d\psi \qquad (5.7)$$

Depending on whether the slope is lateral or longitudinal to the flight direction, this
angular component is correlated either with the roll or pitch angles' offsets. If the
target is horizontal ($\beta \rightarrow 0$), the yaw angle offset obviously becomes indeterminable.

The Equations 5.5–5.7 are not used directly due to their singularity problem and
due to the fact, that they are only valid, if the angular offsets were uncorrelated.
Yet they can be used to estimate the influence of a difference $dh$ on the angular
offsets.

Favey, E., 2001. *Investigation and Improvement of Airborne Laser Scanning Technique for Monitoring Surface Elevation Changes of Glaciers*. ETH Zurich, Diss. No. 14045
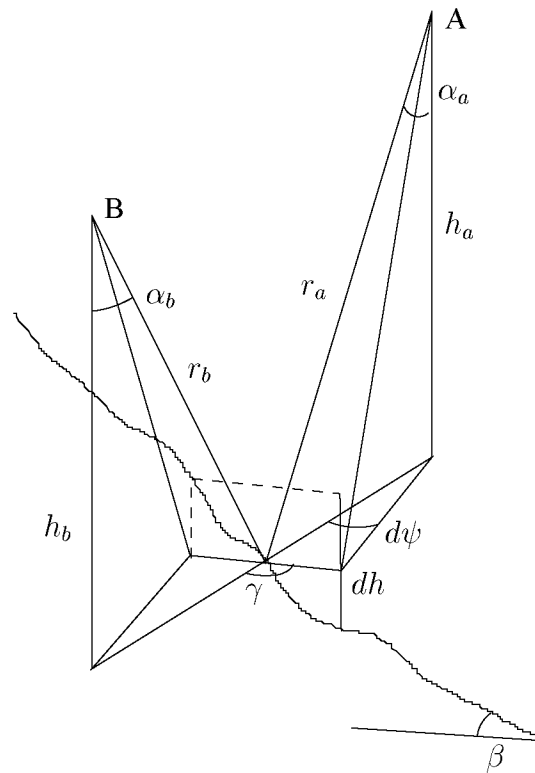
Figure 5.5.: Yaw angle determination from tilted target lateral to flight direction in strip overlap or along the flight direction from forward and backward scan. The subsets $A$ and $B$ need to be from different strips or need to have a time lag of at least 2 seconds.

Favey, E., 2001. *Investigation and Improvement of Airborne Laser Scanning Technique for Monitoring Surface Elevation Changes of Glaciers.* ETH Zurich, Diss. No. 14045

### 5.3.3.   Determination of Offset Angles Using Least-Squares Adjustment

For the LSQ adjustment, the observation equation (5.4) is linearized as

$$\frac{\partial F}{\partial \boldsymbol{u}} d\boldsymbol{u} = -F(\boldsymbol{l}, \boldsymbol{u}_0) \tag{5.8}$$

The $z_A$ and $z_B$ values are calculated as a weighted mean of the respective selected local subset points $i$. For a subset $N$ holds:

$$z_N(\boldsymbol{l}, \boldsymbol{u}) = \frac{\displaystyle\sum_{i \in N} w_i (x_i(\boldsymbol{l}, \boldsymbol{u}) - x_0, y_i(\boldsymbol{l}, \boldsymbol{u}) - y_0) \cdot z_i(\boldsymbol{l}, \boldsymbol{u})}{\displaystyle\sum_{i \in N} w_i} \tag{5.9}$$

where $w_i$ is a weight function based on the distance between the raw measurement point $(x_i, y_i)$ and the location of interpolation $(x_0, y_0)$ (cf. Section 5.4). Using the general equation for georeferencing (2.16) for a single point $i$, the relation of the subsets' height differences to the unknown parameters is determined as

$$\begin{pmatrix} x_i \\ y_i \\ z_i \end{pmatrix} (\boldsymbol{l}, \boldsymbol{u}) = \boldsymbol{x}_i^{\mathcal{G}} = \boldsymbol{a}^{\mathcal{G}} + \boldsymbol{R}_{\mathcal{G}/\mathcal{L}} \boldsymbol{R}_{\mathcal{L}/\mathcal{B}} \left( \boldsymbol{R}_{\mathcal{B}/\mathcal{S}} \cdot r \boldsymbol{s}^{\mathcal{S}} + \boldsymbol{b}^{\mathcal{B}} \right) \tag{5.10}$$

As the partial derivations to the unknown angle offsets need to be built for the linearization (Equation 5.8), they need to be calculated for each point $i$. This is realized using numerical derivation (Press et al., 1992) to each of the unknown parameters. Due to the non-linearity of the observation equation (5.4) with respect to the unknown angular offsets, the LSQ-adjustment needs to be iteratively solved.

### 5.3.4.   Results of Offset Angles Estimation

The attitude angle data of 1999 was measured using two independent sensor orientation systems. A comparison of these two attitude angle solutions is presented in chapter 4. The laser scanning data of 1999 for the region of Lauteraargletscher was georeferenced separately with both attitude solutions. These two solutions were then entered into the self-calibration procedure.

The angle offsets determined by the self-calibration technique are listed in Table 5.1. Theoretically, the differences between the misalignment offsets of the GPS/iMAR solution and those of the Applanix solution should be the same as the mean attitude angle differences listed in Table 4.3. For convenience the mean attitude angle differences of all eight strips are listed again in Table 5.1.

Due to the instability over time of the attitude angle differences between the two INS systems, the misalignment offset between those two systems can be determined only

| attitude system | roll angle [°] | | pitch angle [°] | | yaw angle [°] | |
|---|---|---|---|---|---|---|
| | $d\phi$ | $\sigma_{d\phi}$ | $d\theta$ | $\sigma_{d\theta}$ | $d\psi$ | $\sigma_{d\psi}$ |
| GPS/iMAR | −0.020 | 0.003 | 0.798 | 0.002 | 0.615 | 0.008 |
| Applanix | 0.064 | 0.003 | 0.025 | 0.001 | 0.004 | 0.007 |
| difference | −0.084 | | 0.773 | | 0.611 | |
| from Table 4.3 | −0.085 | | 0.717 | | 0.703 | |

Table 5.1.: Results of self-calibration calculations for Lauteraargletscher flight 1999. The comparison of the alignment angles between the body frame $\mathcal{B}$ realized by the GPS antennae and the Applanix strap-down IMU frame shows a good coincidence especially for the roll angle. The pitch and yaw angles show the same magnitude within 0.07–0.09°.

to about 0.1° accuracy. The results from self-calibration show a good agreement—within the noted accuracy—with the raw angle differences presented in Chapter 4.

The $\sigma$ values listed in Table 5.1 are the square root of the a posteriori variances of the unknown parameters. They hint the weaker determinability of the yaw angle misalignment. In the case of Lauteraargletscher, the strong inclinations of the scanned terrain allows the introduction of the yaw angle unknown into the adjustment.

For a target like the Dübendorf runway (Section 7.2), the determination of a yaw angle misalignment from the height data alone is not possible. The LSQ adjustment does not converge, or its matrix becomes nearly singular in such a case. For an urban area without enough height contrast, matching techniques using the reflectance intensity data as noted in Section 5.3.1 would be more suitable for determining the yaw angle offset.

| attitude system | roll angle [°] | | pitch angle [°] | | yaw angle [°] | |
|---|---|---|---|---|---|---|
| | $d\phi$ | $\sigma_{d\phi}$ | $d\theta$ | $\sigma_{d\theta}$ | $d\psi$ | $\sigma_{d\psi}$ |
| GPS/iMAR | 0.000 | 0.002 | 0.083 | 0.002 | 0.366 | 0.008 |

Table 5.2.: Result of self-calibration calculations for Lauteraargletscher flight 1998. The offset angles apparently do not remain stable between different campaigns

The offset angles determined for the 1998 flight differ from those of 1999. Even though the same equipment was used, it was unmounted after the 1998 campaign and remounted for 1999. Apparently, the offsets do not stay the same. The 1998 data is additionally degraded, as the dynamic sensitivity of the scanning mirror distorts the self-calibration results (cf. Section 7.3.2).

The $\sigma$ values are only an relative quality measure for how well those offsets can be estimated from the data supplied. They are based on the assumption that the offset

values remain constant during the whole flight. The experiences from Chapter 4 reveal, that this assumption is only true on the 0.1° level. Thus the accuracy of the self-calibration angles can only be considered with an accuracy to this level as well, if one wants to apply them for a whole flight.

Introducing the three unknowns on a per strip basis works only for the pitch angle. For the other two angles, at least one strip would need to remain locked for the LSQ adjustment to become determinable.

## 5.4.    Height Interpolation Using Weighted Mean

How to interpolate the height from the laser data for a specific location $(x_0, y_0)$ depends strongly on the needed interpolation characteristics (Geiger, 1996). Dealing with a huge amount of laser data, a local interpolation technique is needed.

There are commonly three different types of local interpolation techniques used:

**The weighted mean** is an interpolation method, where the interpolated value should be estimated 'as well as possible' in the sense of least squares.

**Osculating approximations** are interpolation methods, where a trend function like a polynomial or a Fourier model is locally fitted through the data points.

**Patched approximations** divide the local interpolation domain into finite elements, wherein the interpolation is done using a polynomial approach (e.g. TIN structures).

As already mentioned above the patched approach is rather sensitive to signal noise and rough terrain. Using a trend function on the other hand would require to define a regression model based on the terrain that is to be mapped. Using a weighted mean approach allows to define a damping effect through the weight function and is not computationally expensive. That's why this approach was chosen for the interpolation.

The weight function $w_i$ is chosen in a similar manner to collocation techniques as a function of the distance $\rho_i$ of the $i$-th data point from the location to interpolate:

$$w_i = \frac{\varepsilon^n}{\rho_i^n + \varepsilon^n} \tag{5.11}$$

$$\rho_i = \sqrt{(x_i - x_0)^2 + (y_i - y_0)^2} \tag{5.12}$$

where

$n$: exponent often set to 2, determines the steepness of the gradient in $\varepsilon$.

$\varepsilon$: damping coefficient of the same unit as $\rho$, often called correlation length, as it corresponds to the distance at which the weight $w_i = 0.5$ (Figure 5.6).

Equation 5.11 has the advantageous characteristics, that

- at the interpolation position itself with $\rho_i = 0$, the weight is $w_i = 1$, e.g. for a point located exactly at $x_i = x_0$ and $y_i = y_0$.

- the damping coefficient $\varepsilon$ can be chosen with a value whose meaning is easily apprehensible,

- it shows a similar form as a Gauss curve, i.e. with increasing distance $\rho$, the influence of a data point asymptotically approaches 0.
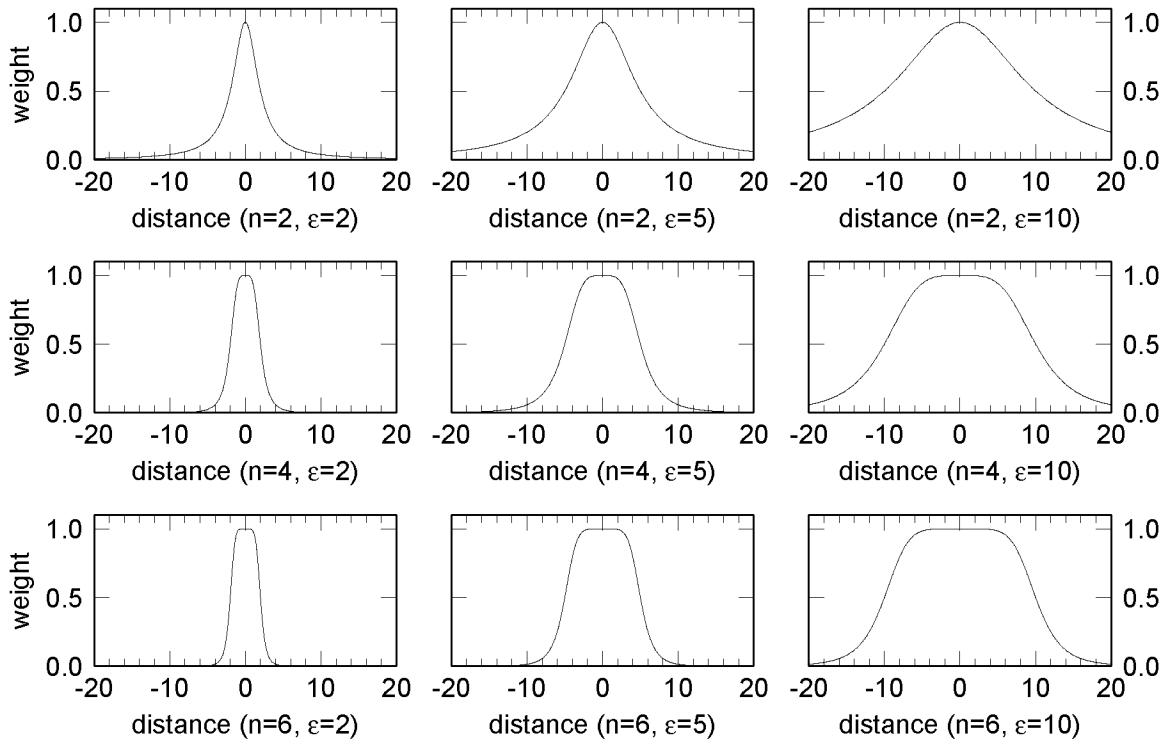


Figure 5.6.: Examples of the weight function $w$ depending on the exponent $n$ and the damping coefficient $\varepsilon$ versus the distance $\rho$.

The values of $n$ and $\varepsilon$ are chosen with respect to the footprint size $f$, the laser data point spacing $s$ and the desired damping effect of the interpolation. If the values are chosen as

$$n = 4, \quad \varepsilon \geq s \quad \text{and} \quad \varepsilon > 2f \tag{5.13}$$

then within $\rho \leq f$ the weight will stay at 1, whereas a neighboring point's influence will decline rather drastically. If a stronger damping is desired, the values could be set to

$$n = 2 \quad \text{and} \quad \varepsilon \geq 2s \tag{5.14}$$

Favey, E., 2001. *Investigation and Improvement of Airborne Laser Scanning Technique for Monitoring Surface Elevation Changes of Glaciers.* ETH Zurich, Diss. No. 14045

The size of a patch $N$ is limited to a threshold radius $R$, the points are selected as:

$$\forall i \in N : \rho_i \leq R \qquad (5.15)$$

The radius $R$ is chosen depending on the weighting function, so that $w_i \to 0$ for $\rho_i \to R$. Looking at Figure 5.6, a value like $R = 10\frac{\varepsilon}{n}$ should satisfy this need.

# 6. Results of Airborne Laser Scanning

## 6.1. Digital Surface Model Generation

### 6.1.1. Accuracy Estimate of Generated Model Derived from Contributing Measurement System Performances

The quality of the final result naturally depends on the quality of the contributing elements as shown in Section 2.5. Thus the quality of the positioning and attitude solution has to be monitored when generating the DSM.

The quality of the GPS positioning is determined by the dilution of precision (DOP) value calculated for each epoch. Figures 6.1–6.3 show the DOP values for the glacier trajectories of 1998 and 1999.

The parts of the trajectory, where the DOP gets unuseably bad were not used for the laser evaluation. This applies mainly to the strip 9812 closest to Finsteraarhorn in 1998, as well as for the beginning of strip 9811. Only the parts of those strips were used, where the DOP value was smaller than 10.

The satellite constellation in general was better during the 1999 flight. Strip number 9809, the east strip on Strahleggggletscher in 1998 was flown with 4 satellites visible only. Thus this strip's accuracy is expected to be considerably degraded, i.e. worse than 1 m position accuracy.

As an indicator of the quality of the attitude determination, the fitting RMS of the drift estimation can be used (cf. Table 4.2). Putting things together according to Equation 2.25, an accuracy estimate for each strip can be calculated. The DOP value interpreted as cm is multiplied with 2.5, as the height is determined weaker by this factor due to the satellite geometry. Thus for a DOP of 3 we set $da_3 = 0.075$ m. Table 6.1 shows the estimates for the laser strips of 1998 and 1999.

As can be derived from Table 6.1, the laser data of Strahleggggletscher of 1998 is heavily degraded. This will also have consequences for the temporal analysis of the Strahleggggletscher data.

All points are individually georeferenced using Equation 2.16. For display and temporal analysis, the points were gridded with 10 m spacing using the weighted mean
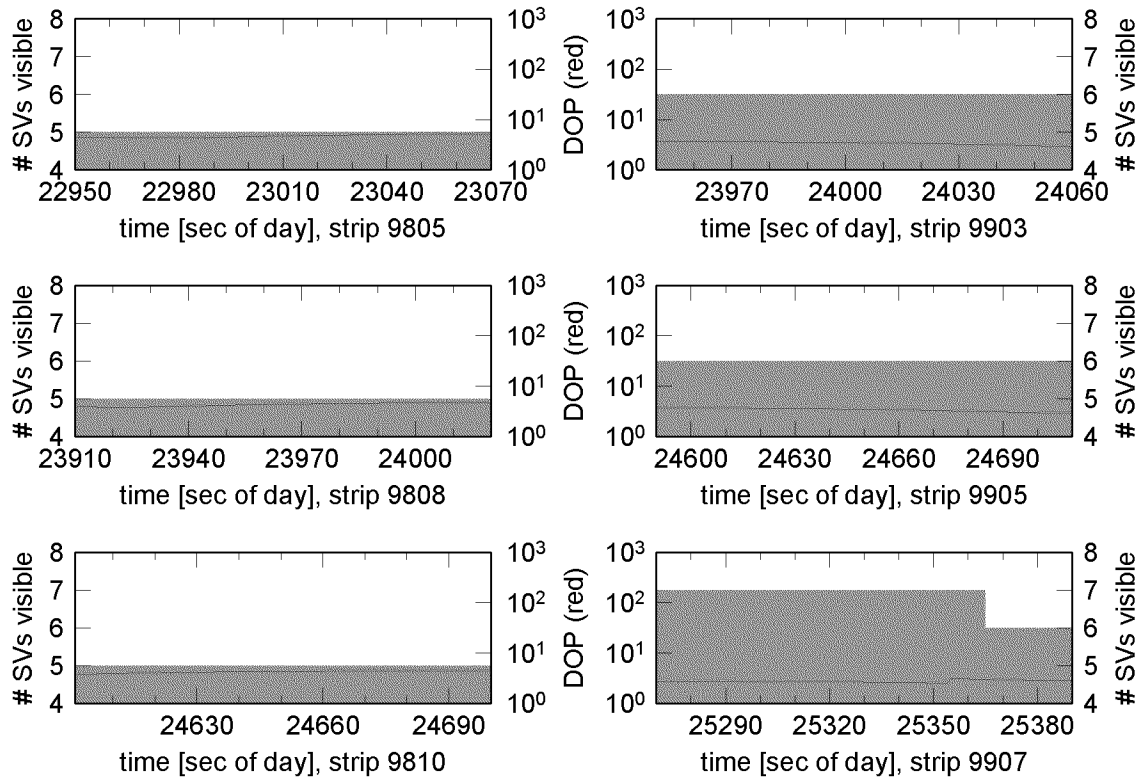
Figure 6.1.: Satellite count and DOP values for each of the laser scan strips of Lauteraargletscher in 1998 and 1999.
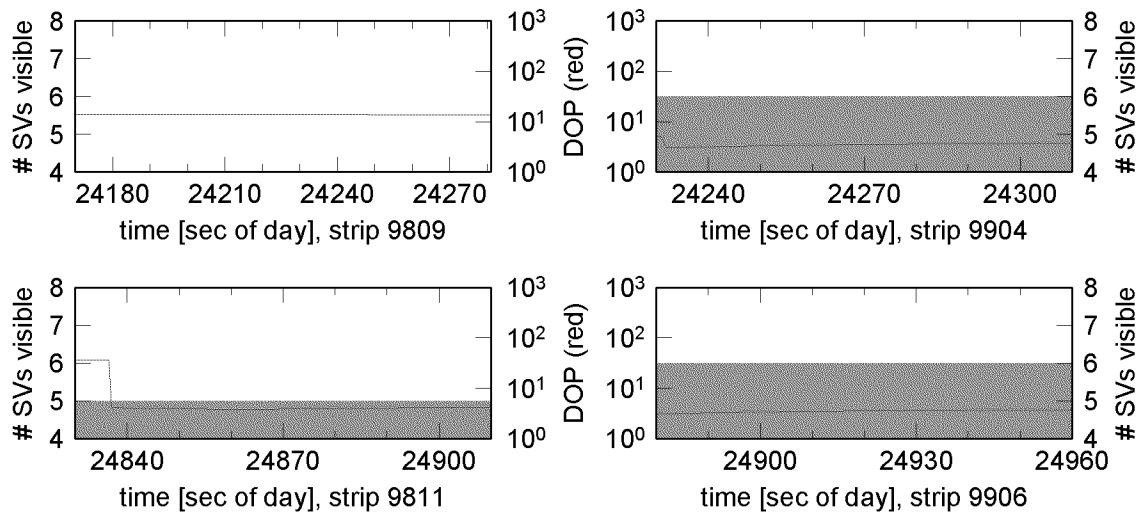
Figure 6.2.: Satellite count and DOP values for each of the laser scan strips of Strahleggletscher in 1998 and 1999.
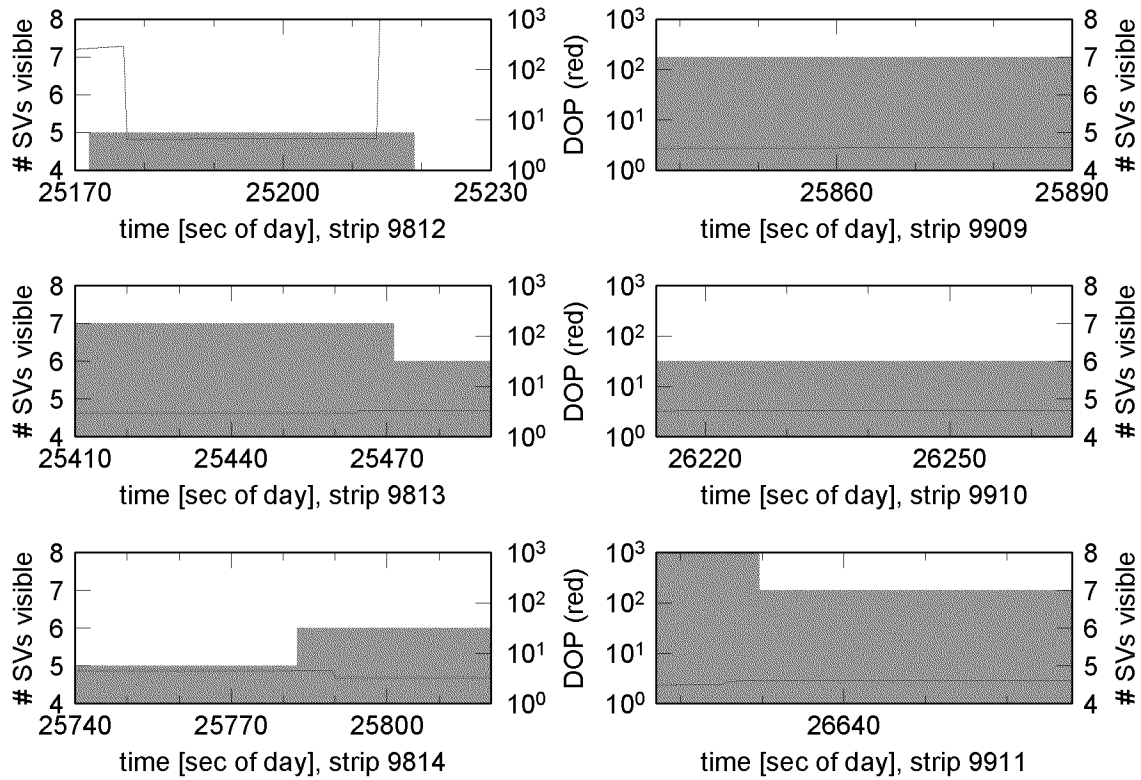
Figure 6.3.: Satellite count and DOP values for each of the laser scan strips of Finsteraarfirn in 1998 and 1999.
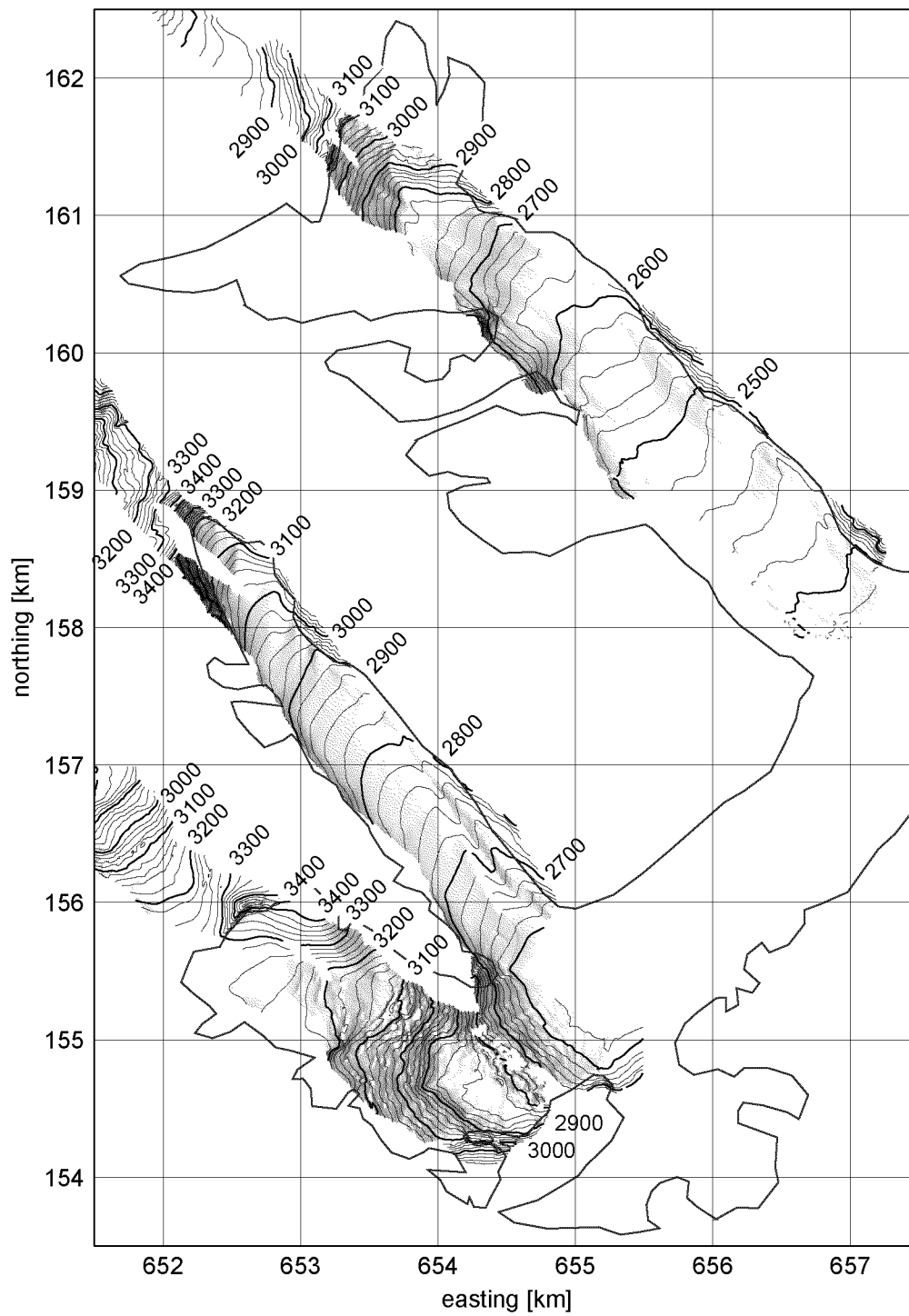
Figure 6.4.: DSM generated from laser scanning data for the year 1998. The contour interval is 20 m.
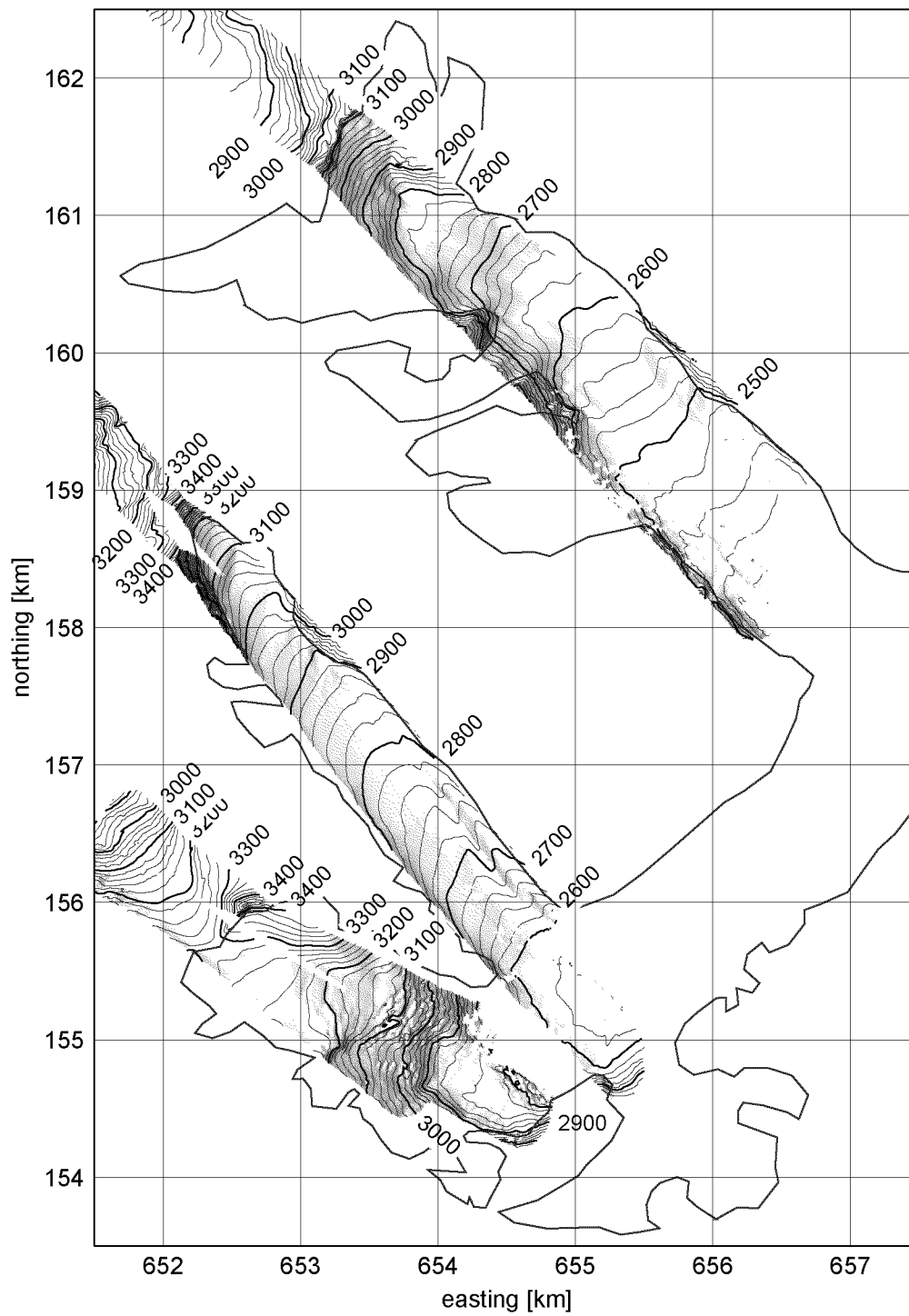
Figure 6.5.: DSM generated from laser scanning data for the year 1999. The contour interval is 20 m.

| Glacier | Strip # | DOP | $\sigma_e$ | $\sigma_{x_3}$ |
|---|---|---|---|---|
| Lauteraar-gletscher | 9805 | 5 | 0.10 | 0.54 |
| | 9808 | 4 | 0.11 | 0.57 |
| | 9810 | 4 | 0.19 | 0.94 |
| Strahlegg-gletscher | 9809 | 14 | 0.39 | 1.90 |
| | 9811 | 4 | 0.21 | 1.03 |
| Finsteraar-gletscher | 9812 | 4 | 0.15 | 0.75 |
| | 9813 | 3 | 0.25 | 1.22 |
| | 9814 | 4 | 0.10 | 0.53 |
| Lauteraar-gletscher | 9903 | 3 | 0.04 | 0.29 |
| | 9905 | 3 | 0.10 | 0.53 |
| | 9907 | 3 | 0.05 | 0.32 |
| Strahlegg-gletscher | 9904 | 4 | 0.06 | 0.37 |
| | 9906 | 4 | 0.08 | 0.45 |
| Finsteraar-gletscher | 9909 | 3 | 0.10 | 0.53 |
| | 9910 | 3 | 0.10 | 0.53 |
| | 9911 | 3 | 0.05 | 0.32 |

Table 6.1.: Accuracy estimates for each individual laser scan strip.

approach described in Section 5.4. For the temporal analysis following in the next section, the elements of the weight function (Equation 5.11) were chosen as $\varepsilon = 3\,\text{m}$ and $n = 2$. The contributing point search was limited to a radius $R = 15\,\text{m}$.

The Figures 6.4 and 6.5 show the actual coverage of the laser scanning and the resulting DSM. The data spans over more than $1000\,\text{m}$ height difference.

## 6.1.2.  Results of Blunder Detection Algorithm

The quality of the raw laser distance measurement is strongly dependent on the reflectivity of the target surface. As shown in Section 7.2.3, a low reflected signal intensity causes a higher probability of wrong ambiguity fixing.

The 'dark' parts for the laser wavelength of $810\,\text{nm}$ pose problems to the laser scanning technique, as the reflection there is much weaker than on snow and ice. This is mainly the case in the cliff regions and on debris-covered parts of the glacier or moraines.

The blunder detection algorithm described in Section 2.2.4 was applied to all of the laser scanning data. Figure 6.6 shows a visual example of the success of the blunder detection and removal algorithm. As Table 6.2 shows, the majority of the blunder can be detected and removed. This brings a considerable improvement to the accuracy of the laser scanning DSM, as the RMS of the differences of the comparison with the photogrammetric dataset indicates (cf. Section 7.3).

(a) 1 × 1 km without blunder detection

(b) 1 × 1 km after blunder detection and removal
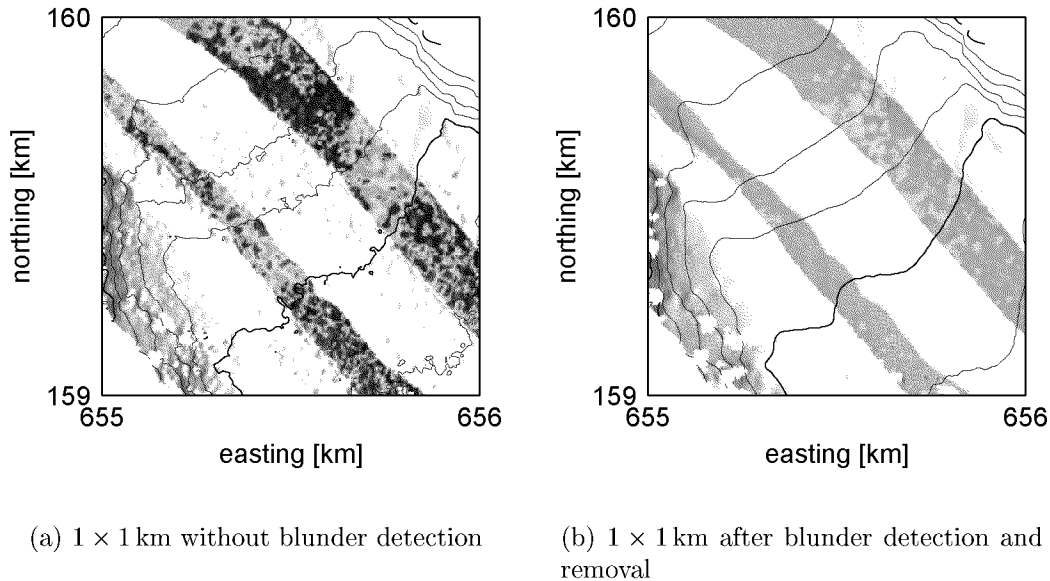
Figure 6.6.: Success of blunder detection algorithm. The colored parts are the strip overlap differences scaled the same way as in Figures 6.7–6.10.

| strip | before blunder removal | | | after blunder removal | | | # points removed |
|---|---|---|---|---|---|---|---|
| | # pts | RMS [m] | blunder % | # pts | RMS [m] | blunder % | |
| 9903 | 353829 | 3.3 | 5.7 | 336589 | 0.5 | 0.8 | 17240 |
| 9905 | 401274 | 3.9 | 7.3 | 372997 | 0.5 | 0.4 | 28277 |
| 9907 | 254312 | 4.2 | 9.0 | 234313 | 0.7 | 1.9 | 19999 |

Table 6.2.: Effect of blunder detection and removal algorithm. The RMS is calculated from the difference of each single laser ground point minus the height interpolated in bilinear manner from the Lauteraargletscher 1999 photogrammetry dataset. Threshold for blunders percentage calculation is 1.7 m. This threshold is calculated as $3\sigma$ where $\sigma^2 = \sigma_l^2 + \sigma_p^2$. A priori accuracies are assumed: for laser scanning $\sigma_l = 0.4$ m (tilted target with an inclination of 10°), and for the photogrammetric dataset $\sigma_p = 0.4$ m.

# 6.2.  Analysis of Laser Strip Overlaps

## 6.2.1.  Repeatability of Laser Scanning Data Over the Glacier Test Area

The overlap areas of adjacent laser strips were evaluated regarding repeatability. The achieved overlap percentage is compared with the flight plan and discussed.

The laser strips on the glacier were flown with a planned overlap of 30–50%. Those overlap areas contribute to the roll and yaw misalignment offset angle estimation described in Section 5.3. If the misalignment angles can be successfully estimated and corrected, the overlap areas as well as cross-overs show the repeatability of laser scanning.

Some of the flight strips could not be navigated as planned with the desired precision. This has mainly two reasons:

- The navigation system relies on receiving the differential GPS correction signal broadcast either by UHF or on medium wave radio stations. Due to the remote location of the test area, the UHF signal is not received. Even with the medium wave signal stations, there were problems. With repeated loss of the differential signal, the navigation accuracy dropped sometimes to GPS C/A code navigation accuracy of 100–300 m, as at the time of the campaigns, selective availability (SA) was turned on.

- Strong side winds carry the airplane off the desired flight track. The pilot needed to hold against the wind causing the plane to fly with a crab angle. This problem can be observed looking at the scanning strips of 1998 on Lauteraargletscher (Figure 6.7). There the winds caused the strip to be instantly displaced horizontally by the amount of half the strip width. As the airplane got into the grasp of the wind, the roll angle changed to hold against the wind.

The 1998 dataset (Figures 6.7 and 6.8) shows the much rougher flight conditions of that year compared to 1999 (Figures 6.9 and 6.10). In the four figures showing the distribution of the strip overlap differences, some more observations can be made:

- In Figures 6.7 and 6.8, local accumulations of systematic differences of the order of 1–2 m can be observed. These are located at the positions, where the laser strip coverage instantly moved 100 m sideward due to strong winds and turbulences. This effect is due to the sensitivity of the scanning mirror to dynamic forces (cf. Equation 7.4 and Figure 7.13)

- Figure 6.9 shows a good coincidence of the two overlap areas. Here the flight tracks could be flown successfully; no gaps occurred. The overlap has an average width of 100 m, which corresponds to 30%.
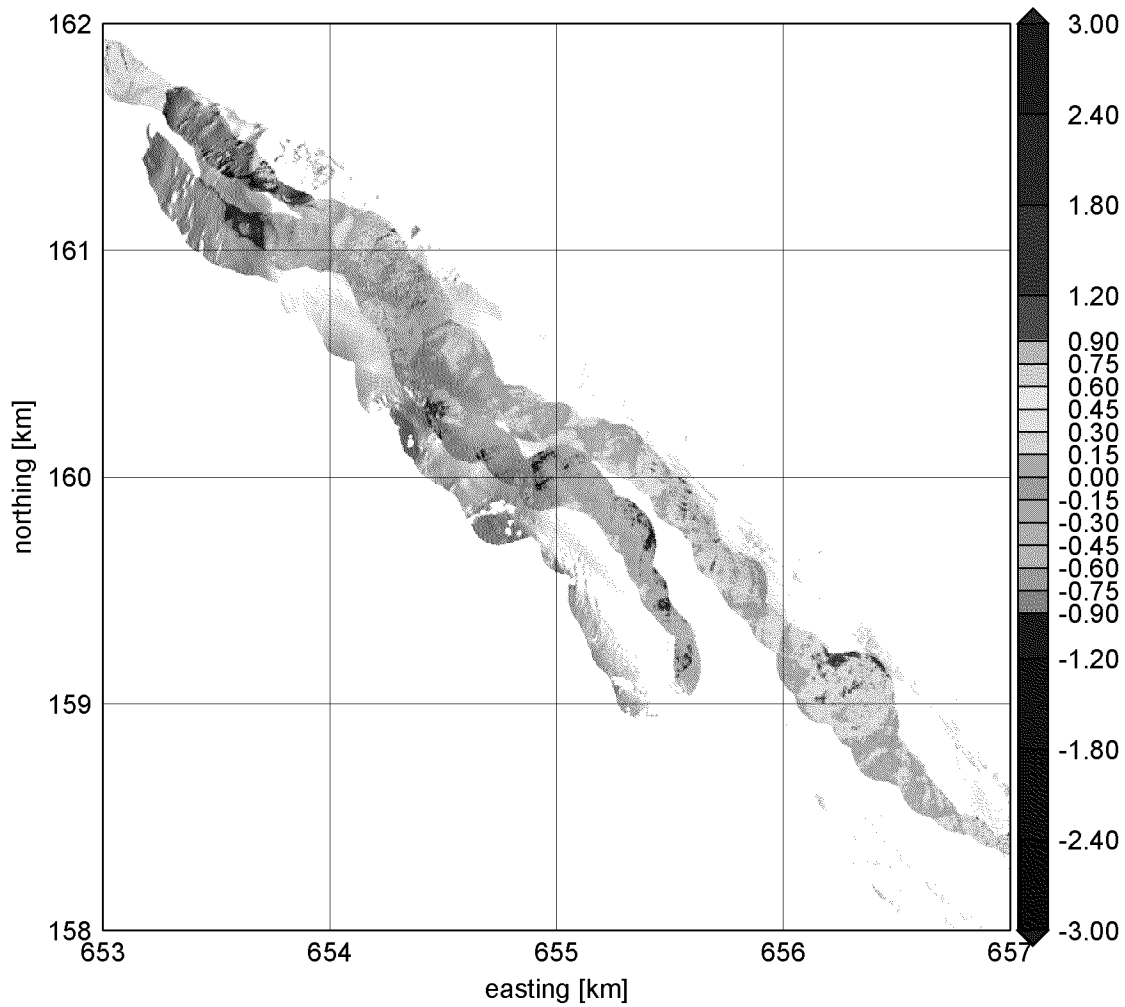
Figure 6.7.: Overlap analysis, difference of individual strips on Lauteraargletscher 1998. The differences 9810−9808 and 9808−9805 are plotted in color. The grey intensity shows the coverage of the individual strips.
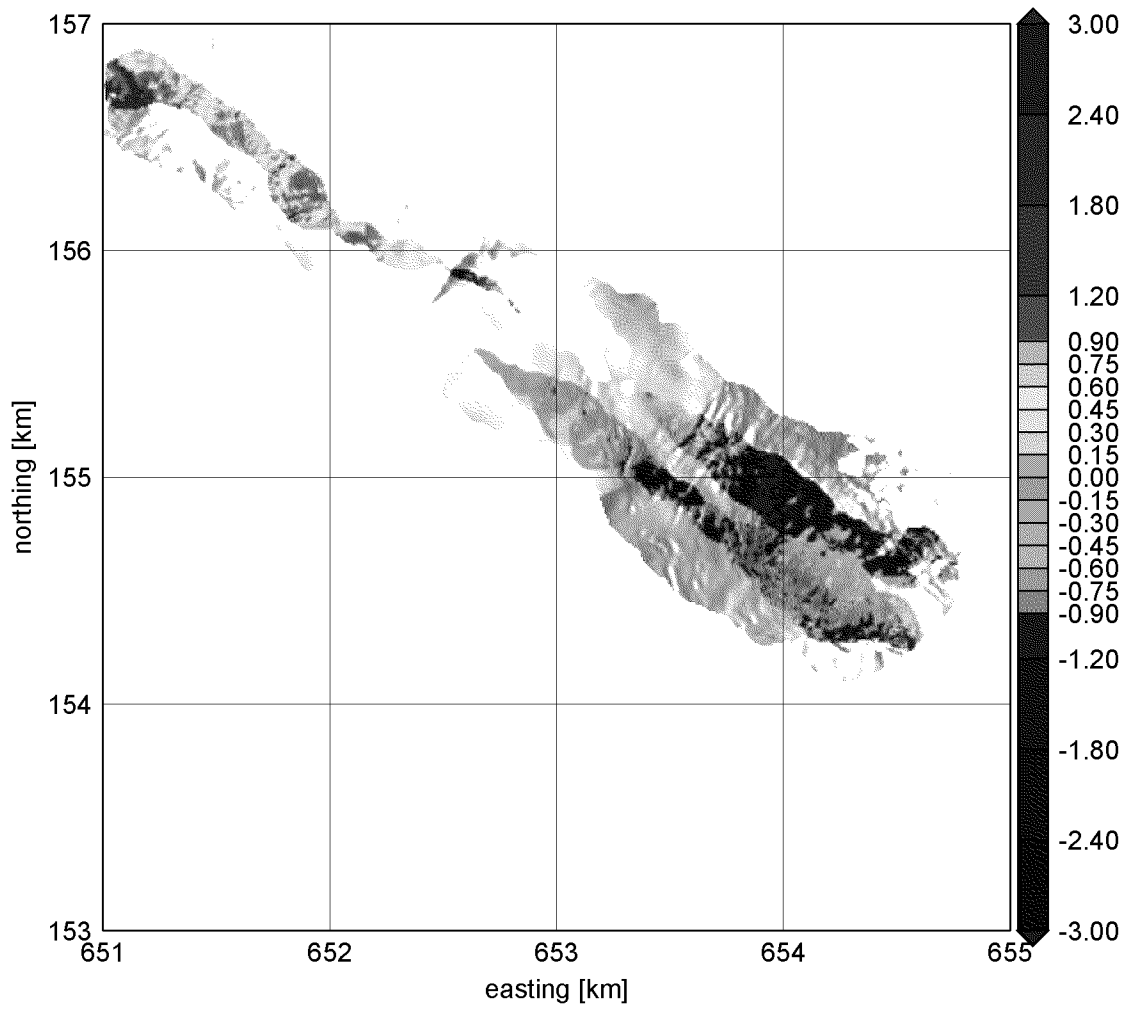
Figure 6.8.: Overlap analysis, difference of individual strips on Finsteraarfirn 1998. The differences 9814−9813 and 9813−9812 are plotted in color.

Favey, E., 2001. *Investigation and Improvement of Airborne Laser Scanning Technique for Monitoring Surface Elevation Changes of Glaciers.* ETH Zurich, Diss. No. 14045
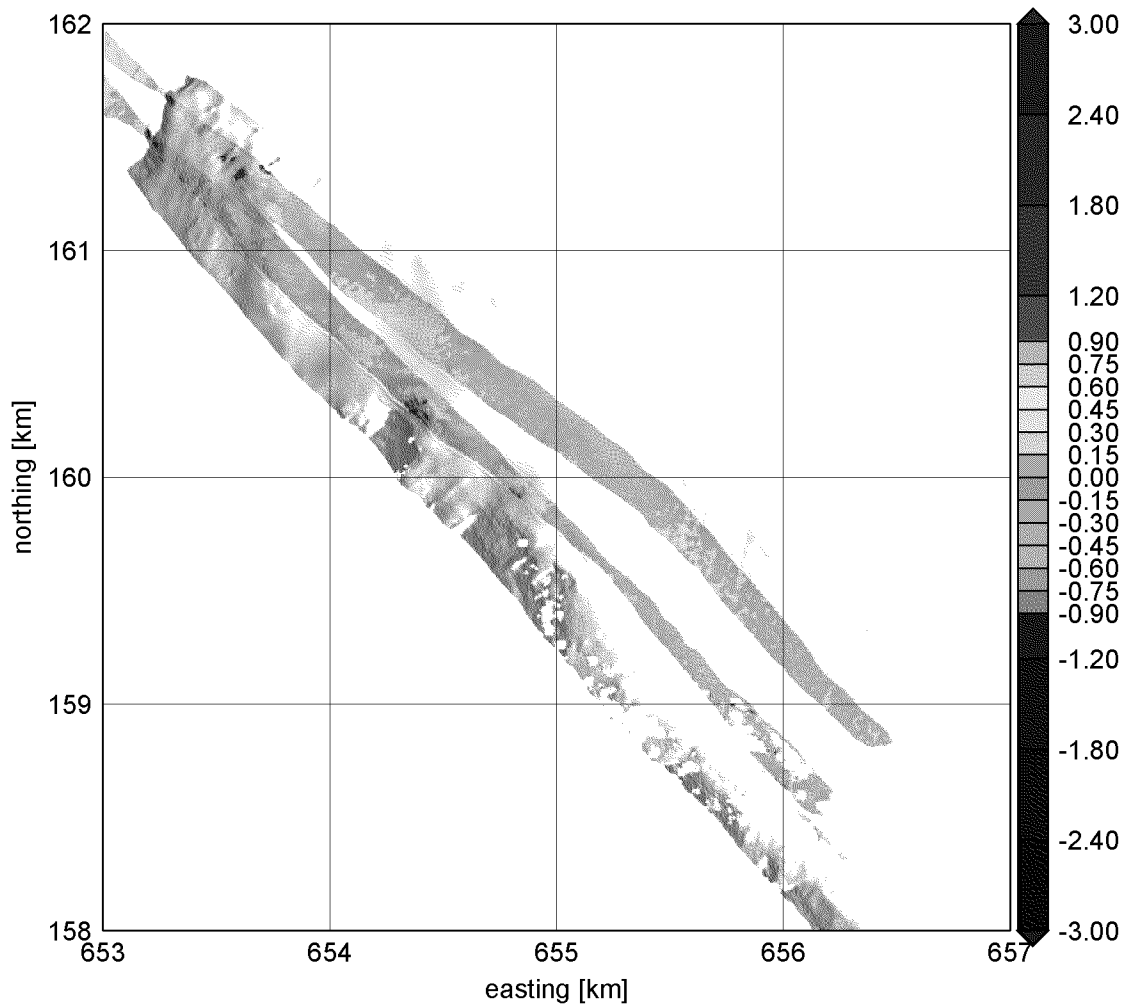
Figure 6.9.: Overlap analysis, difference of individual strips on Lauteraargletscher
1999. The differences 9907−9905 and 9905−9903 are plotted in color.
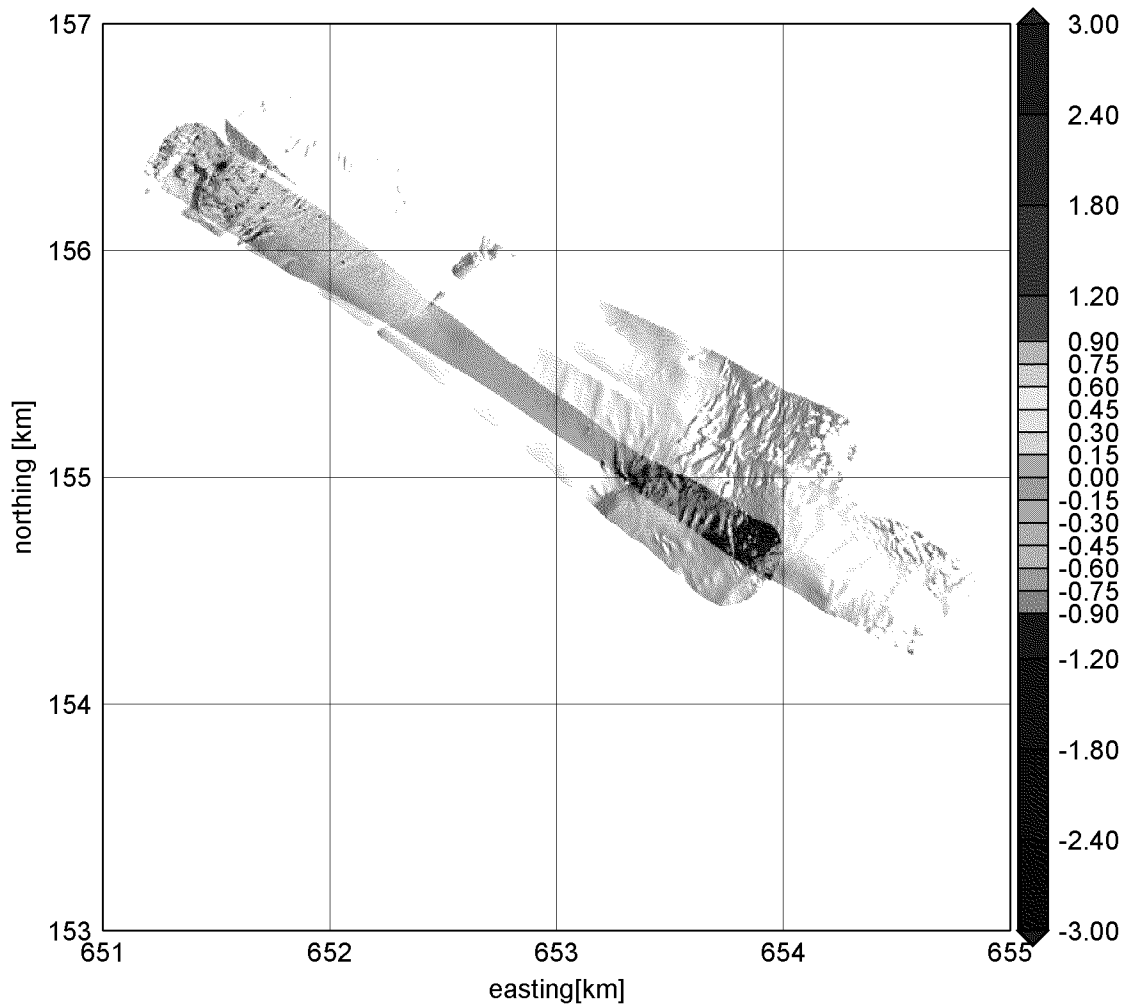
Figure 6.10.: Overlap analysis, difference of individual strips on Finsteraarfirn 1999. The differences 9911−9910 and 9910−9909 are plotted in color.

- Steep terrain slope increases the effect of horizontal positioning error onto the height difference. This can be seen in the area of Lauteraarsattel in the upper left corner of Figure 6.9 as well as in the steep ice-fall in the lower right part of Figure 6.10. System calibration according to Section 5.3 aids minimizing this effect, but it does not model it entirely.

- The center strip 9910 in Figure 6.10 begins with almost 100% overlap with the westmost strip, gradually moving into its requested path, but not reaching it altogether. This caused a gap of 20–50 m over the firn area between the center strip 9910 and the eastmost strip 9909.

The overlap differences are calculated by interpolating the height from one strip at the locations of the shots of its peer. The statistics of the strip overlap analysis are listed in Table 6.3.

| laser overlap | # pts | RMS [m] | Mean with sign [m] | Max abs. [m] | blunder[1] % |
|---|---|---|---|---|---|
| 9808−9805 | 310657 | 0.78 | 0.04 | 10.75 | 4 |
| 9810−9808 | 152271 | 0.84 | −0.17 | 8.84 | 5 |
| 9812−9814 | 101656 | 1.21 | −0.28 | 11.93 | 12 |
| 9814−9813 | 135535 | 2.06 | −0.41 | 14.84 | 30 |
| 9905−9903 | 214030 | 0.54 | 0.01 | 9.04 | 1 |
| 9907−9905 | 159648 | 0.65 | 0.05 | 8.57 | 2 |
| 9910−9909 | 8091 | 2.14 | −1.40 | 10.84 | 4 |
| 9911−9910 | 171323 | 0.96 | −0.21 | 12.99 | 7 |

[1]Threshold for blunders is 1.7 m. This threshold is calculated as $3\sigma$ where $\sigma^2 = 2\sigma_l^2$. An a priori accuracy is assumed for laser scanning: $\sigma_l = 0.4$ m (tilted target with an inclination of 10°).

Table 6.3.: Analysis of overlap information.

On Lauteraargletscher, the RMS of the overlap areas is below 1 m for 1998 and 1999. For the latter it is on the order of the expected accuracy around 0.6 m. The Finsteraarfirn strips of both years suffer from increased blunder, especially due to the steep slopes and the crevasses at either end of the strips. The maximum blunder magnitude does not exceed 15 m.

## 6.2.2.   Flight Plan and Navigational Considerations

The deviation of the realized flight strips from the planned flight trajectory leads to some thoughts concerning the navigational conditions and the aeronautical impact onto laser scanning measurements. The following aspects require special attention for laser scanner flights in an alpine environment:

**Weather aspects:** Important factors are thermal effects, wind and visibility conditions. On warm end summer days, thermal effects make a low flying height above ground dangerous. During the 1998 laser scanning flight, rather strong winds caused turbulences degrading the data quality, as strong accelerations influence the mechanical rotating parts like the scanning mirror. Of course visibility has to be clear at the flight altitude. During one mission flight, the weather forecast promised a sunny day, but arriving in the test area, local clouds were covering the desired trajectory. Fog or clouds between aircraft and target area must not occur. As the method is independent of external light sources like the sun, it could be used also during night time for flat areas. Yet, in an alpine environment, this is not advisable.

**Seasonal aspects:** The end of the ablation season is a must for mass balance determination. Weather conditions pose a certain risk on the feasibility of such measurements, e.g. the first snow may come early, thunderstorms and strong winds are likely in fall, the technique competes with photogrammetry flights ranking at higher priority (due to stronger weather dependency). These seasonal risks are common to both laser scanning and photogrammetry.

**Security aspects:** A low flying height above ground for scanning and the high mountains require a tradeoff. In order to avoid the aeronautical problems of realizing a full coverage of a glacier like Unteraargletscher by laser scanning, there are two possibilities:

1. During the planning phase of the project, the idea of using a helicopter was thought of. This would have the advantages to be able to follow the flight technically difficult terrain in a more flexible way. The height above ground could have been kept at an optimum and the coverage of the remote corners of the firn area could have been realized. Yet, using a helicopter brings along other problems and does not solve some severe ones:

   - As the flying altitude is rather high and the laser equipment heavy, a helicopter strong enough to operate up to 4000 m.a.s.l. would be needed. This increases the cost for the flight.
   - The helicopter would need to be modified for the laser scan equipment to be firmly mounted. The relation of the GPS antenna to the laser scanning hardware frame needs to be rigidly stable. The GPS antenna needs to be located at a place where the rotors do not obstruct the satellite visibility.
   - Flying at a lower altitude than the mountains will even worsen the satellite visibility. As showed in Section 3.3.3, this can lead to unusable positioning data, thus the strip there would have to be remeasured when the satellite constellation is sufficient.

- The increased vibration's and higher flight dynamic's effect on the scanning mirror technique would need to be studied. Scanning hardware usually includes some rotating element, which is sensitive to acceleration and fast rotation. The flight planning needs to regard this hardware sensitivity.

2. The ability to use a higher flying height above ground would lead to less aerotechnical problems. The obstruction of satellite visibility by surrounding terrain is less severe. A wider swath width could be realized, thus less scan strips would be needed to cover the same area.

   On the other hand, this would require a laser scanning system with the ability to measure up to at least 2000 m without loss of distance measurement quality. With the increasing flying height above ground, the requirements for the accuracy of the attitude system increases as well. Yet with the recent evolution on the laser scanning and georeferencing market, such systems with higher performance become more and more available.

**Financial aspects:** Since the weather dependency requires the laser scan equipment and personnel to be on standby for at least a 2 weeks period, most commercial laser scanning firms and aircraft operators will either charge this time at full cost, or they will not be ready to conduct the measurements due to commercial pressure.

## 6.3. Comparison of Yearly Generated DSMs and Interpretation

### 6.3.1. Computation of Surface Elevation Change

For glaciological purposes, digital surface models are only a byproduct on the way to determine mass balance. Of much greater interest are the surface elevation differences from DSMs of different epochs. To be able to build a surface elevation change distribution model, the contributing DSMs need to be referenced in the same, well defined coordinate frame. This is the main reason, why the photogrammetric control points were always kept in the same local datum, as it was established with the first few points during the 60's.

As the laser scanning data depends entirely on the GPS reference frame for positioning purposes, they were transformed to the LV95 coordinate frame, in order for future campaigns to be compatible. This way, the GPS reference station does not need to be always the same one on a control point at the target region itself, which would cost a considerable amount of time to occupy, as they are not easily accessible.
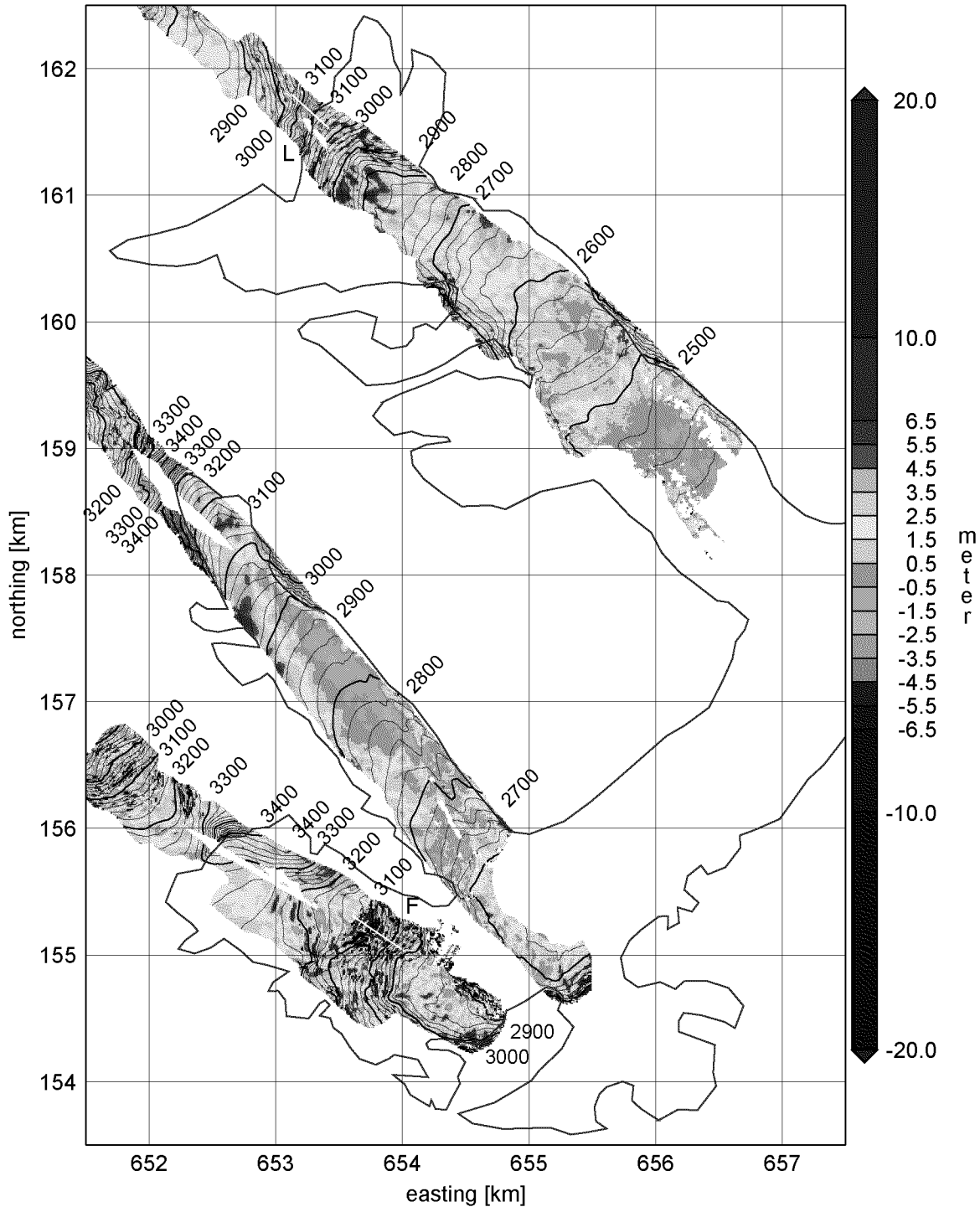
Figure 6.11.: Temporal difference of the years 1999 minus 1998 determined from the laser scan data. Note the zero difference at the saddle area of Lauteraargletscher, where the cliffs are exposed. The locations of the profiles in Figures 6.13 and 6.14 are marked as white lines and labelled L and F, respectively.
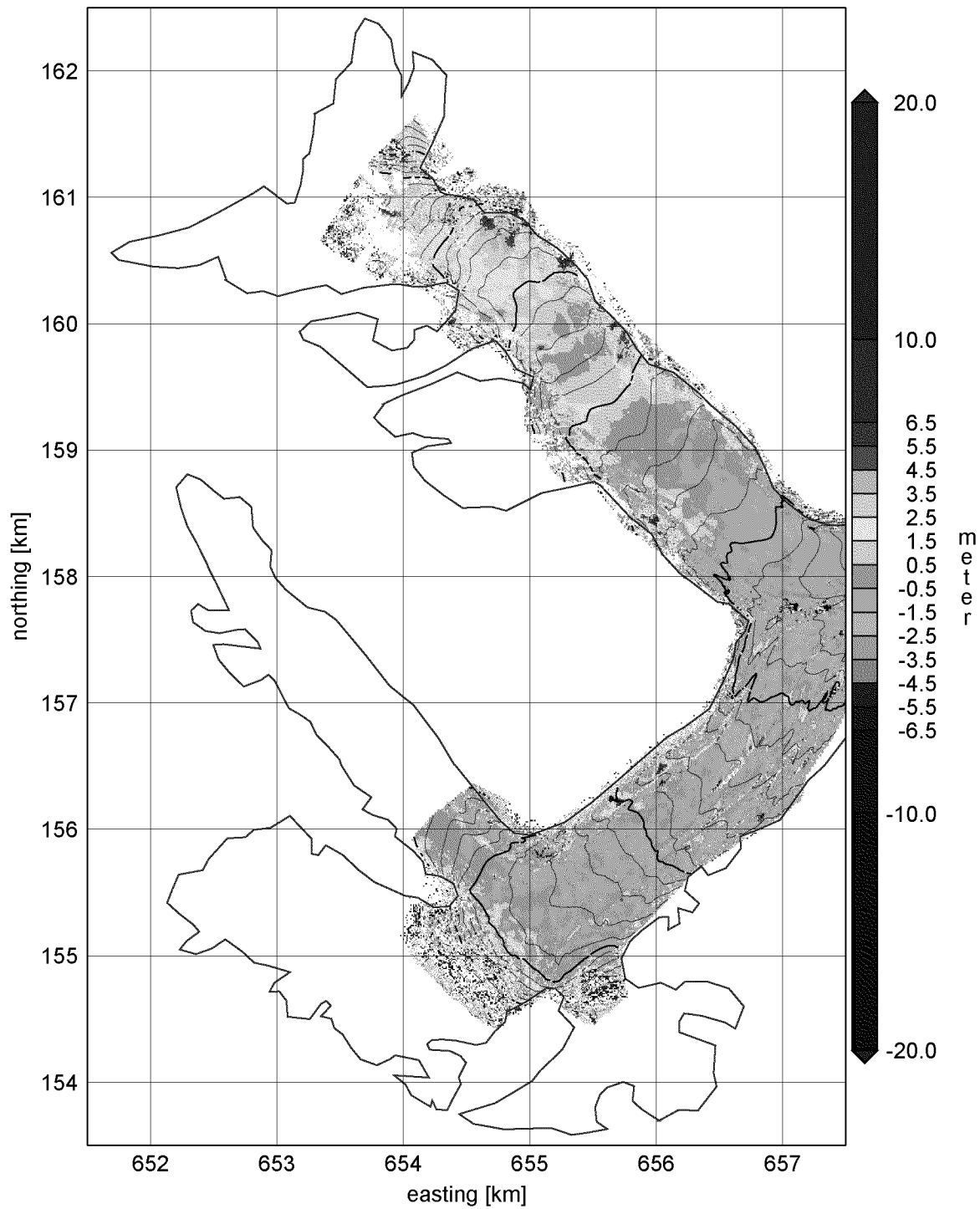
Figure 6.12.: Temporal difference of the years 1999 minus 1998 determined from the digital photogrammetry data. On Lauteraargletscher, the photogrammetric dataset and the laser dataset have much of the covered area in common.

The final product being a surface elevation change distribution model, any systematic offsets of a geodetic datum are differenced out. Thus the comparison of the surface elevation change distribution determined by photogrammetry and the one determined by laser scanning are free of any datum differences.

The differences of different epochs of data are built by subtracting the newer DSM from the older one. A visual comparison of the yearly difference distributions derived from laser scanning (Figure 6.11) with the one derived from photogrammetry (Figure 6.12) shows a good match. A detailed analysis of the differences of the surface elevation change determined by both methods is given below in Section 6.3.2. To further examine the surface elevation change derived from the laser scanning data, two profiles are extracted. Their location is indicated in Figure 6.11.

The first profile $L$ is taken from the area of Lauteraarsattel (Figure 6.13). The center of the profile is the cliff area. On the cliffs there is no significant surface elevation change. As soon as the glacier area starts, the surface elevation change increases to about 4 m.

The second profile $F$ is taken from the area at the end of Finsteraarfirn, where many wide and deep crevasses dominate the topography. The crevasses on Finsteraarfirn are moving with a velocity of about 40 m per year. Except for very few selected objects, there is not enough texture in the height in order to deduce a full horizontal velocity field. Crevasses may open up and close again over time, thus finding one to be identical to another identified the previous year is rather delicate.

## 6.3.2. Comparison of Surface Elevation Change Results from Laser Scanning and Photogrammetry

For comparison, the DSM of laser scanning and photogrammetry are double differenced as:

$$\Delta \dot{h} = (h_{\text{laser}}(1999) - h_{\text{laser}}(1998)) - (h_{\text{photo}}(1999) - h_{\text{photo}}(1998)) \tag{6.1}$$

The resulting value $\Delta \dot{h}$ is free from any systematic vertical geodetic datum offset. The accuracy of a single estimate of surface elevation change is calculated as

$$\sigma_h^2 = \sigma_h^2(t_{\text{new}}) + \sigma_h^2(t_{\text{old}}) \tag{6.2}$$

Thus for the double differenced comparison values, the a priori accuracy can be calculated as

$$\sigma_{\Delta h}^2 = 2\sigma_l^2 + 2\sigma_p^2 \tag{6.3}$$

The following a priori accuracies are assumed: for laser scanning $\sigma_l = 0.4$ m (tilted target with an inclination of $10°$), and for the photogrammetric dataset $\sigma_p = 0.4$ m. In this case, the expected accuracy $\sigma_{\Delta h}$ of the double difference values amounts to
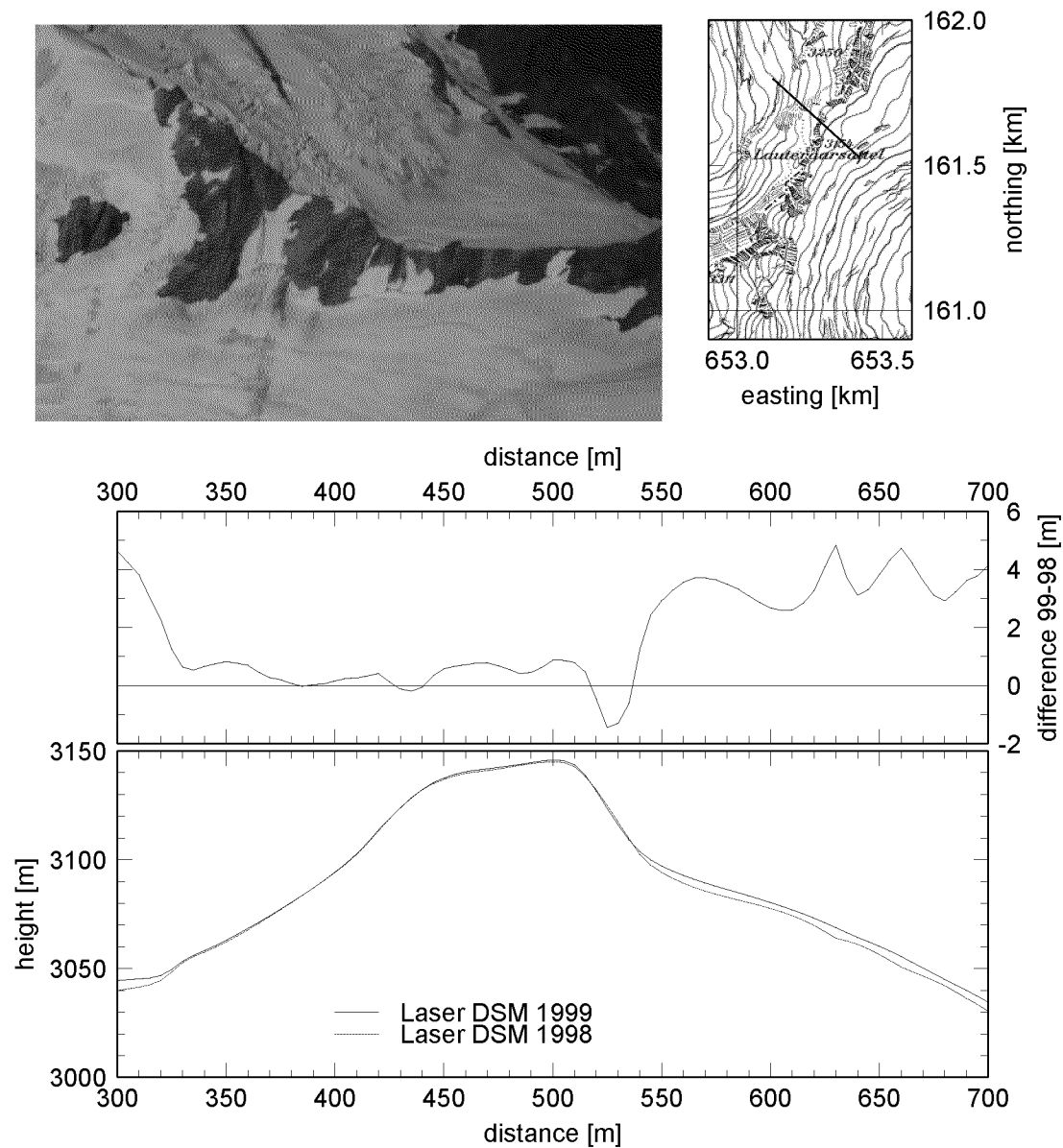
Figure 6.13.: Profile $L$ through laser data at Lauteraarsattel. Over the cliff part
(350–540) the profiles match each other, whereas on the glacier firn
(540–600) the 1999 profile is systematically higher by about 4 m.
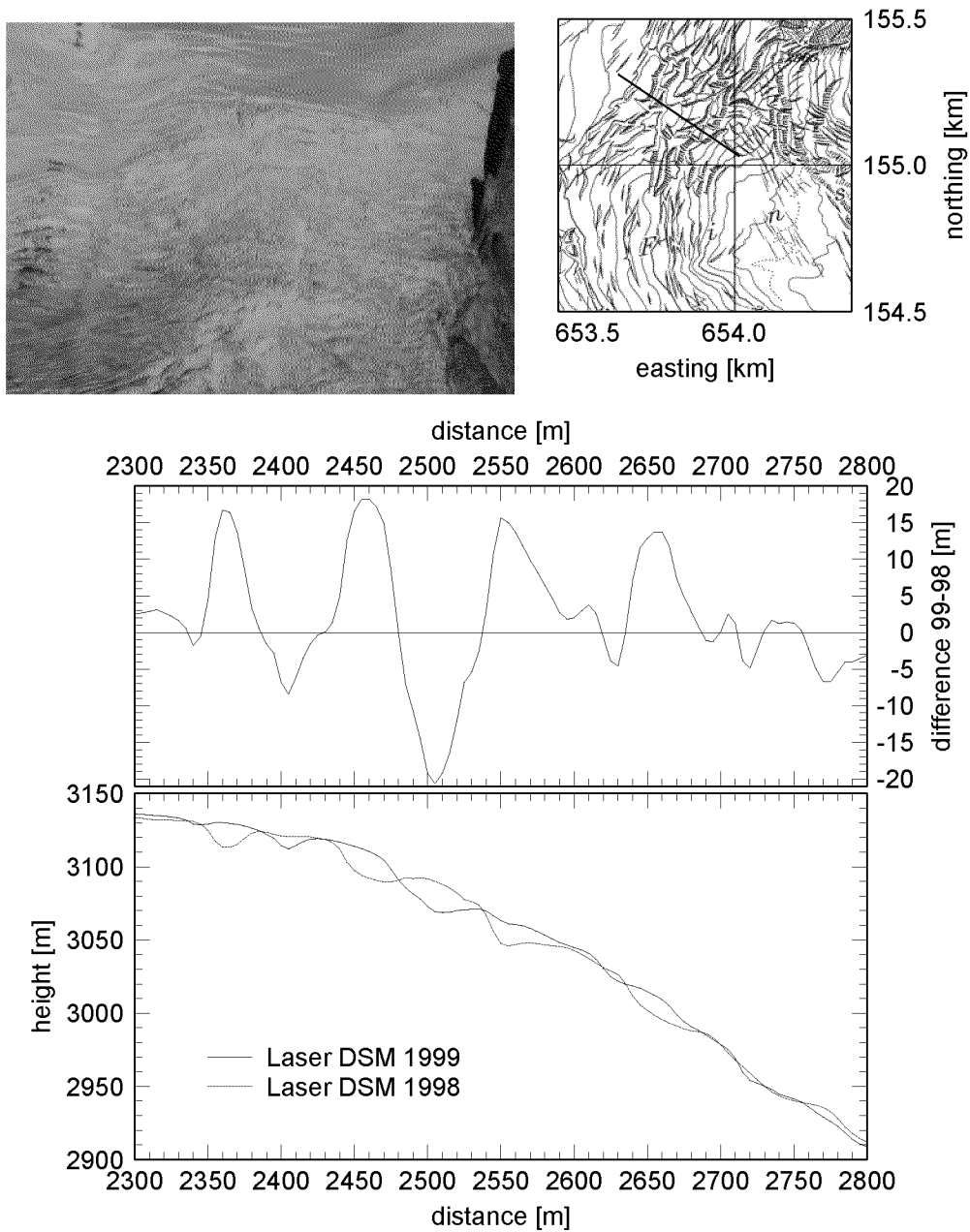
Figure 6.14.: Profile $F$ through laser data at Finsteraarfirn. Distinct features of 1998 are horizontally displaced in the 1999 profile by about 40 m (e.g. ditch from 2370 to 2410).

Favey, E., 2001. *Investigation and Improvement of Airborne Laser Scanning Technique for Monitoring Surface Elevation Changes of Glaciers.* ETH Zurich, Diss. No. 14045

| dataset | # pts | RMS [m] | Mean with sign [m] | Max abs. [m] | blunder[1] % |
|---|---|---|---|---|---|
| all points | 25461 | 0.99 | 0.10 | 33.58 | 3.5 |
| glacier points | 24896 | 0.74 | 0.07 | 15.89 | 2.7 |

[1]Threshold for blunders is 2.4 m. This threshold is calculated as $3\sigma$ where $\sigma$ is calculated as described in Equation 6.3.

Table 6.4.: Comparison of surface elevation change distribution of laser scanning and photogrammetry for the region of Lauteraargletscher.

0.8 m. The statistics in Table 6.4 show a good agreement of the surface elevation change distribution for Lauteraargletscher determined by the two totally independent methods.

Figure 6.15 shows the distribution of the double differences. Of course any quality problems in the originary data propagate also into the double differences. On Lauteraargletscher, the cliff areas show increased noise. The dynamical laser scanning mirror errors also show their patterns in the figure.

The eastmost line of Strahlegggletscher of 1998 has a reduced accuracy due to problems in the GPS positioning solution. This shows up as a systematically high double difference in the lower part of Figure 6.15. For surface elevation change calculations to be better than 1 m, this strip should not be used. The western strip on Strahlegggletscher shows a similar double difference quality as the Lauteraargletscher data.

The few sparse points on Finsteraarfirn are difficult to interpret. They show the difficulty of determining an average surface elevation change in a heavily crevassed area. Due to the steepness of the terrain, the glacier is also expected to flow even faster than the lower parts of the glacier.

## 6.3.3.    Interpretation of Surface Elevation Change Distribution

The surface elevation change distribution determined by remote sensing techniques is not yet the mass balance distribution. It serves as input data to a numerical flow model based on the kinematic boundary condition (Equation 1.2). The data from this project serves as an input to the mass balance determination calculated by Bauder (2001).

Yet the surface elevation change indicates the way, the mass balance change is heading. Figure 6.17 plots the surface elevation change estimates as a function of altitude for Lauteraargletscher. It shows the equilibrium of surface elevation change to be about at 2450 m above sea level. The higher area shows a surface elevation increase of up to 3–4 m.
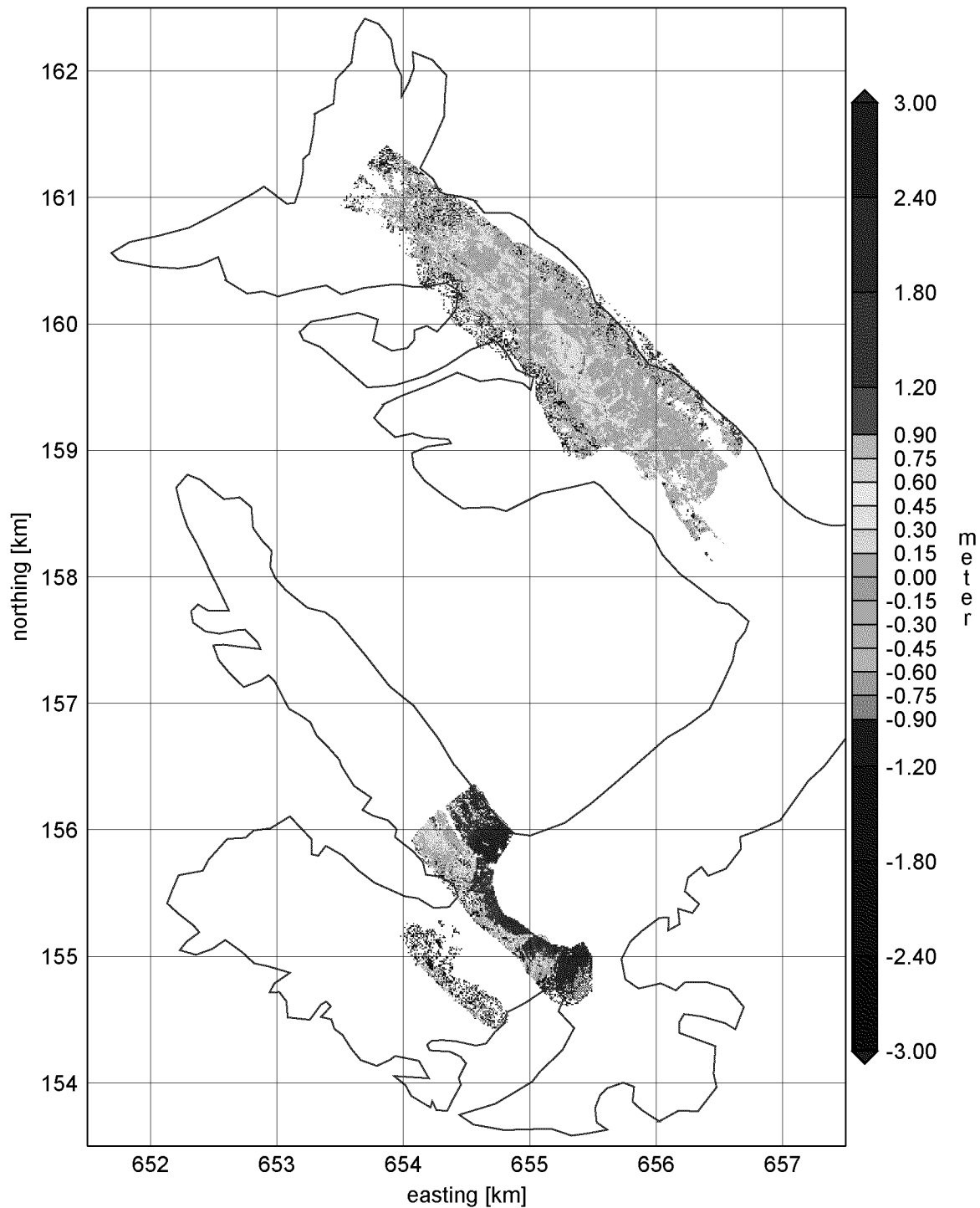
Figure 6.15.: Double difference of the temporal laser data analysis (Figure 6.11) minus the temporal photogrammetric data analysis (Figure 6.12). Note the different color scale. This reveals clearly the accuracy problems of the eastern Strahleggletscher strip of 1998. Note also the acceleration problem of the western Lauteraargletscher strip already found in the direct comparison.

The areas of Finsteraarfirn (Figure 6.16) and Strahleggggletscher (Figure 6.18) also show a positive trend with increasing height.
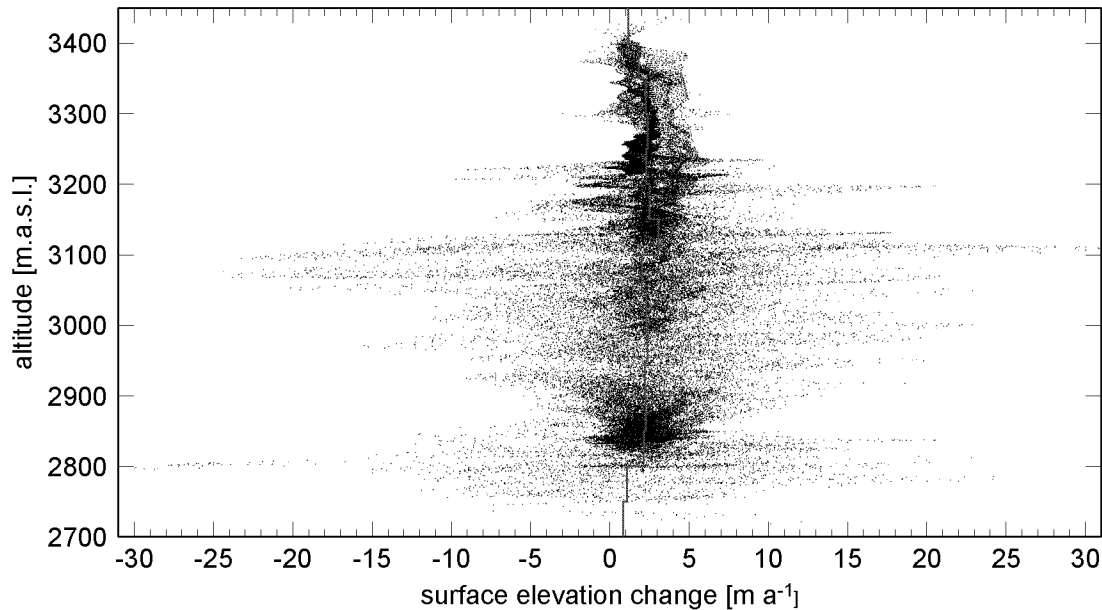


Figure 6.16.: Surface elevation change estimates from laser scan data depicted as a function of altitude for Finsteraarfirn (years 1998 to 1999). The red lines are mean values calculated for each block spanning over 50 m altitude. The heavily crevassed area (cf. Figure 6.14) causes the differences to be spread wide. Nevertheless, a positive trend is visible.

The increase of snow surface elevation in the firn parts can be explained with the high amount of snowfall during the winter 1998/99. Figure 6.19 shows the measured snow height at Grimselpass, about 13 km away from the test area in direction of the glacier tongue. This winter brought about 3 m more snow than the previous winter. It was also staying about one month longer into the summer at 2100 m.a.s.l., where the data was taken.

The regional distribution on the glacier (Figures 6.11 and 6.12) shows local accumulations surface elevation increase. Wherever such a pattern can be identified in shape and correlated with a corresponding surface elevation loss in flow direction upwards, a distinct feature can be assumed and its horizontal flow velocity deduced. An example for this is the profile $F$ analyzed in Figure 6.14.
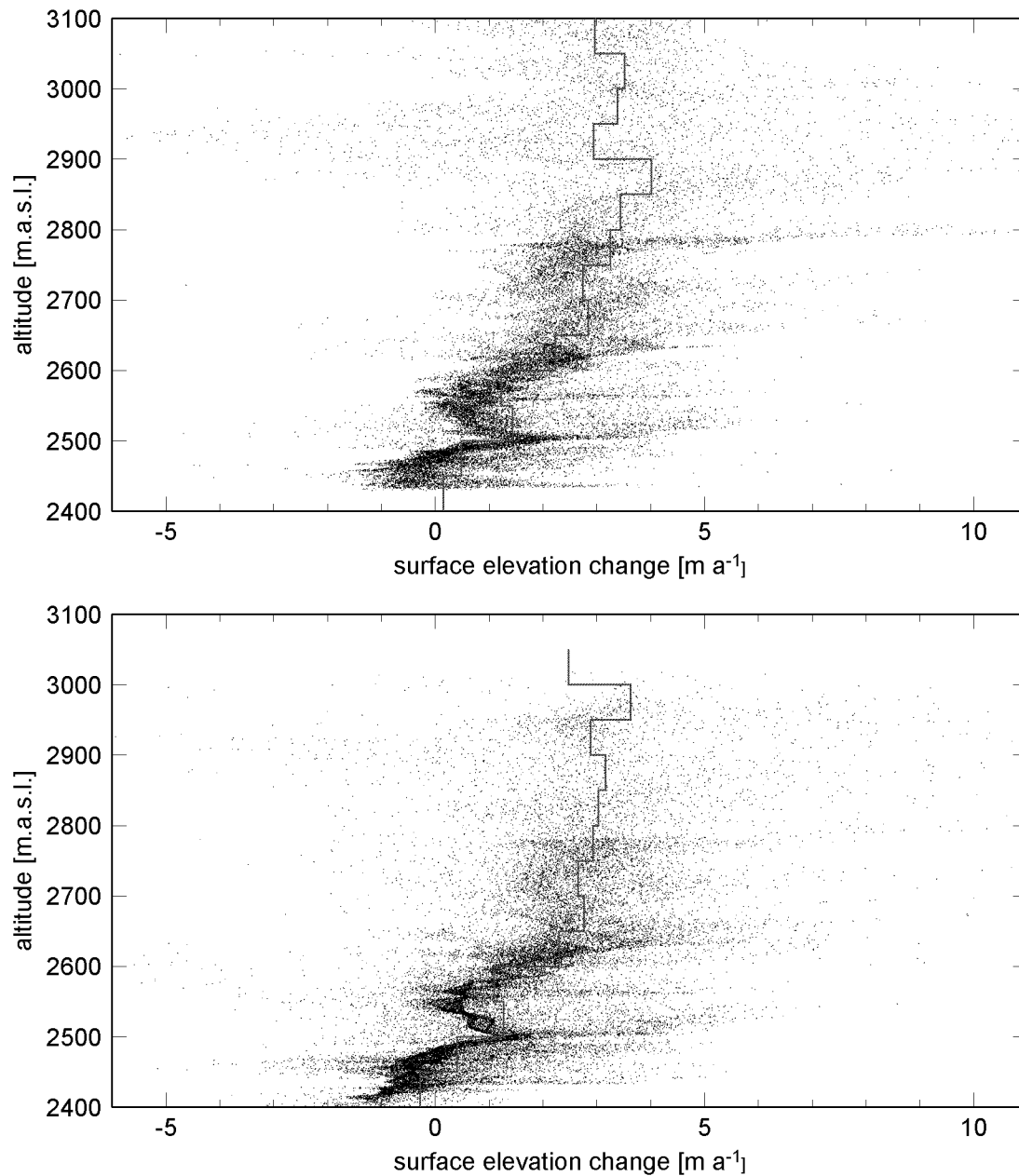
Figure 6.17.: Surface elevation change estimates from laser scan data (above) and from photogrammetry (below) depicted as a function of altitude for Lauteraargletscher (years 1998 to 1999). The red lines are mean values calculated for each block spanning over 50 m altitude. In the region above 2800 m the data is spread wide due to an increased density of crevasses.
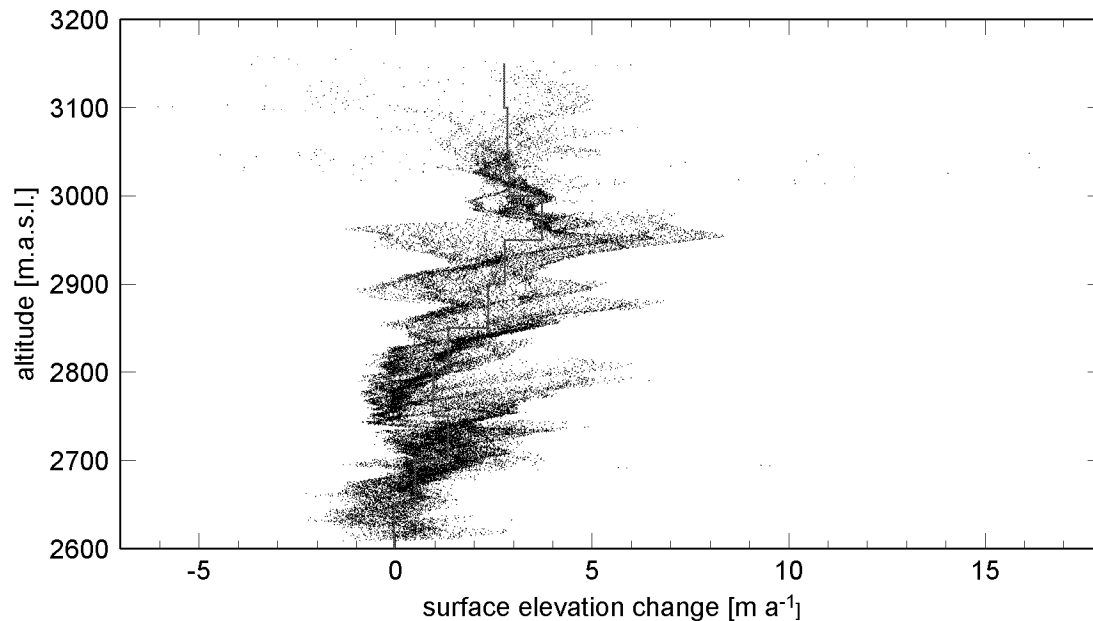
Figure 6.18.: Surface elevation change estimates from laser scan data depicted as a
              function of altitude for Strahleggggletscher (years 1998 to 1999). The
              red lines are mean values calculated for each block spanning over 50 m
              altitude. These surface elevation change estimates were calculated
              without the scan strip 9809, which had a reduced accuracy due to
              insufficient number of visible GPS satellites. Thus only the data from
              the westmost 1998 strip was used.
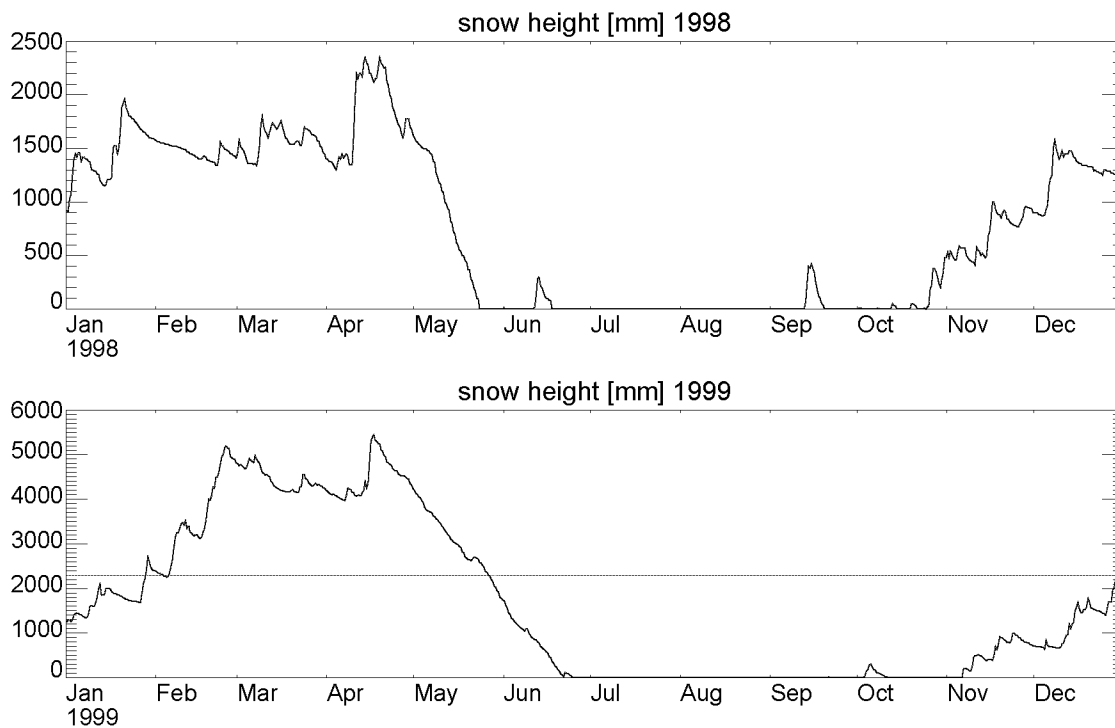
Figure 6.19.: Snow height during the years 1998 and 1999 measured at Grimselpass, 10 km away from the glacier at an altitude of 2100 m a. s. l. (data from SMA-Annalen, 1999). The red line in the lower 1999 graph denotes the maximum snow height during the year 1998. Apparently, the winter 1998/99 brought an extraordinary amount of snow staying about one month longer into the summer than the previous spring.

Favey, E., 2001. *Investigation and Improvement of Airborne Laser Scanning Technique for Monitoring Surface Elevation Changes of Glaciers.* ETH Zurich, Diss. No. 14045

# 7. Validation of Laser Scanning Data with External Information

## 7.1. Geodetic Datum and Swiss Projection

The GPS satellites operate in a coordinate frame commonly known as WGS84, which was adopted as official system for GPS measurements since 1987. Though the coordinate system has never been changed since the rise of GPS, its realization has moved on. In January 1994, the coordinate frame was given a new realization through the use of GPS measurements (NIMA, 2000). It was also oriented according to the International Terrestrial Reference Frame (ITRF) 92. In September 1996, the realization of WGS84 was again changed (now called WGS84 (G873)) as the orientation was adjusted to fit ITRF94 with $\pm 5$ cm. Both times, also some changes were made to the potential model (NIMA, 2000).

For a temporal analysis as done for Unteraargletscher, it is important to evaluate all data in one well defined reference frame. This way, the temporal changes can be attributed entirely to effects of the glacier itself, avoiding systematic effects due to a redefinition of a coordinate frame.

As a global reference frame (like the various ITRF) is affected by plate tectonic movements, its reference coordinates are not constrained but subject to small changes over the years. But for a temporal analysis of the glacier, a reference frame is sought which is not moving.

Switzerland knows two generations of reference systems. The older, called CH1903[1], is based on terrestrial triangulation measurements dating back around 100 years. The coordinates in this system came about in horizontal coordinates (through triangulation) and vertical coordinates (levelling), two entirely disjunct measuring methods. Additionally, in the vertical component, the orthometric correction has often been neglected, thus the height coordinate is called a 'practical height'. When measuring to remote areas as Unteraargletscher, levelling could not be used, thus the height coordinates in this area came about by trigonometric height determination. The relation between CH1903 and WGS84 has been determined in the past by a 7 parameter transformation—including a scale factor modeling the distortion—which

---

[1]CH stands for Confœderatio Helvetica, a synonym for Switzerland

fits best in the urban area of Switzerland. The use of this transformation is deprecated and will be accurate only to the meter level, due to distortions in the historical CH1903 (LV03) frame (Marti and Egger, 1999). Yet the photogrammetric control points are known only with coordinates corresponding to this frame.
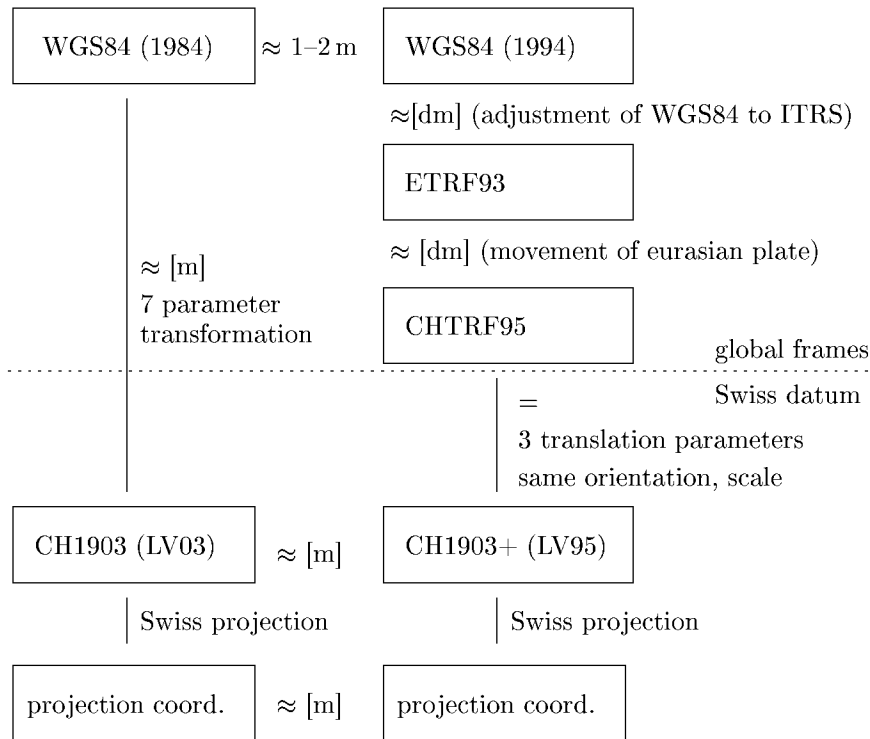


Figure 7.1.: Overview over the geodetic datum transformations. (after Marti and Egger (1999))

The new Swiss reference system is called CH1903+. Its frame (LV95) was realized using GPS measurements resulting in an unconstrained network covering Switzerland. Its relation to global reference systems is well defined by three translational parameters only. The relation to orthometric heights is determined from geoid undulations, known on the centimeter level (Marti, 1997). Figure 7.1 gives an overview of the relations between the different coordinate systems.

Dealing with GPS measurements, a reference frame, which came about in a truly three dimensional manner, such as a GPS network, is much more desirable. Differential GPS can be done in two different manners, assuming that the reference coordinates are known in the Swiss datum:

1. The reference coordinates are known in CH1903, with practical heights. They are transformed using 7 parameters into WGS84 ($\approx$ m accuracy) wherein the differential GPS evaluation is done. Subsequently the resulting coordinates are transformed back into CH1903 with the same 7 parameter translation.

Favey, E., 2001. *Investigation and Improvement of Airborne Laser Scanning Technique for Monitoring Surface Elevation Changes of Glaciers.* ETH Zurich, Diss. No. 14045
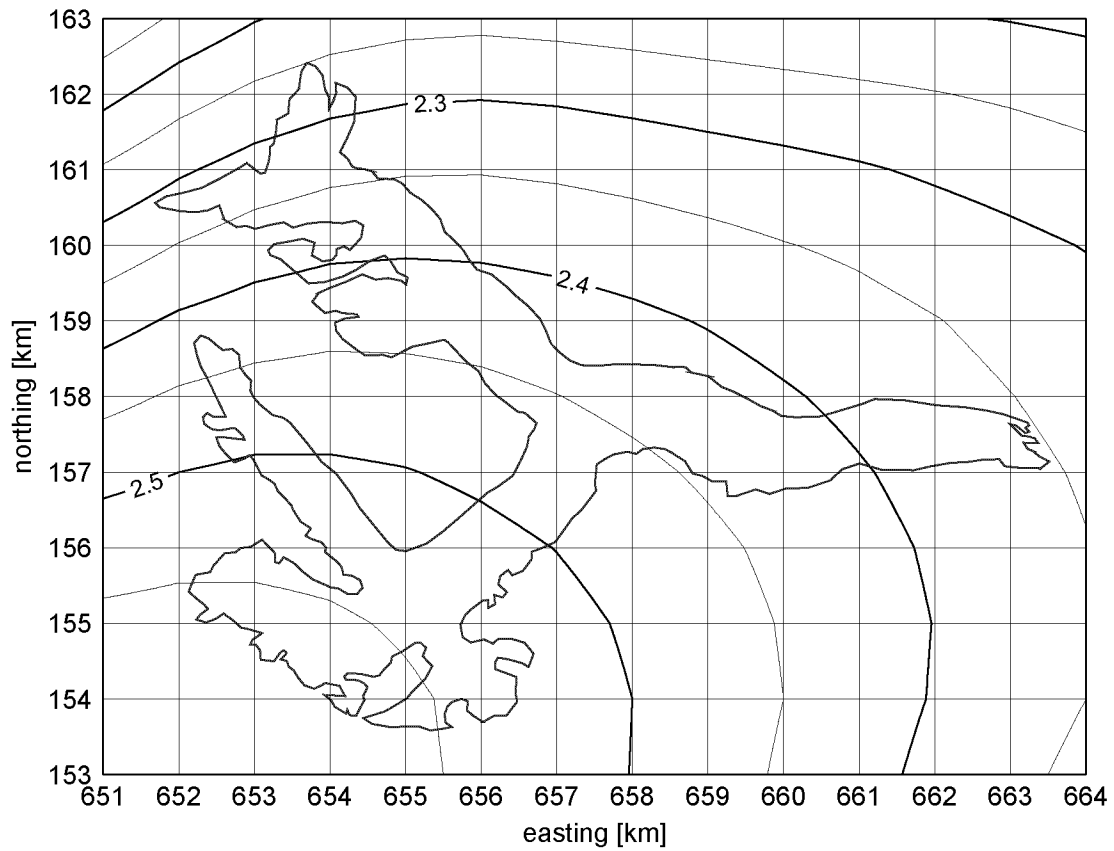
Figure 7.2.: Geoid undulations for the area of Unteraargletscher in the CH1903+
            reference system (calculated from data by Marti, 1997). The contour
            interval is 0.05 m. The contour labels are given in meter. The undulation
            at Unteraargletscher spans from 2.25 m at Lauteraarsattel to 2.6 m at
            the Finsteraarfirn.

For local campaigns with baselines of less than 10 km length, this may lead to satisfactory results. For longer baselines, systematic errors due to the imperfect modeling of the network distortion by the 7 parameter transformation degrade the overall accuracy significantly.

2. The reference coordinates are known in CH1903+, with orthometric heights and their respective geoid undulation. They are transformed using 3 translational parameters into CHTRF95, wherein the differential GPS evaluation is done. Subsequently the resulting coordinates are transformed back into CH1903+. This approach can be used also with long baselines, as no accuracy degradation is introduced by the coordinate transformation process.

For the laser scanning campaigns, baselines of 15–40 km had to be used. Thus the GPS evaluation was done entirely in CHTRF95, and subsequently transformed to CH1903+. Most important reference points—whose coordinates are known in CH1903—can easily be redetermined in CH1903+ by measuring them using GPS in conjunction with a reference station known in the CH1903+ frame. Using the coordinate sets of identical points in both systems, the relation between photogrammetrically determined DSMs and the laser DSM can be established, and the two products can be compared.



Figure 7.3.: Occupation of tripod 102 next to control point 3010 with a dual frequency GPS receiver.

In the case of Unteraargletscher, this was done on three tripods permanently installed on the encompassing cliffs (Figure 7.3). They had been used to measure the ground control points for photogrammetry by theodolite, and are still used as reference points for tracking markers on the glacier itself (Guðmundsson, 1999b). Their coordinates are known in the system CH1903 at the decimeter level. Table

| point ID + point ID | CH1903+ CH1903 difference CH1903+ minus CH1903 | | |
|---|---|---|---|
| | easting | northing | height |
| 104 + 104 | 660046.32 | 157922.94 | 2386.07 |
| | 660046.29 | 157923.17 | 2385.48 |
| | 0.03 | −0.23 | 0.59 |
| 102 + 102 | 657201.42 | 158503.71 | 2427.66 |
| | 657201.36 | 158504.00 | 2426.96 |
| | 0.06 | −0.29 | 0.70 |
| 105 + 105 | 656010.51 | 155256.97 | 2630.61 |
| | 656010.46 | 155257.37 | 2630.08 |
| | 0.05 | −0.40 | 0.53 |

Table 7.1.: Points determined in CH1903 and CH1903+.

7.1 shows, how well the two geodetic data fit. As expected, the differences are on the order of one meter. The accuracy of the values cannot be better than about one decimeter, as the CH1903 coordinates' accuracy is known to be on that order. From these results, the local translational parameters for the area of Unteraargletscher are defined with 5 cm resolution as follows:

$$\begin{pmatrix} E_{\text{CH1903+}} \\ N_{\text{CH1903+}} \\ H_{\text{CH1903+}} \end{pmatrix} = \begin{pmatrix} E_{\text{CH1903}} \\ N_{\text{CH1903}} \\ H_{\text{CH1903}} \end{pmatrix} + \begin{pmatrix} 0.05 \\ -0.30 \\ 0.60 \end{pmatrix} \tag{7.1}$$

## 7.2.   Comparison of Laser DSM with GPS Derived Ground Point Height Information

### 7.2.1.   Comparison with GPS Derived Ground Point Heights

To verify the performance of the total laser scanning system, the sensor orientation techniques described in the previous chapters is applied to laser scanner data on two lines flown in opposite direction over the runway in Dübendorf (Switzerland). The topography of the runway was measured terrestrially using GPS mounted on a car and driving up and down the runway.

The quality of the kinematic GPS reference height measurements was affected by multipath, and is on the order of 0.05 m. The primary reference station for both, the airborne as well as the ground trajectories was the permanent GPS station located on the roof of an ETHZ building, located at about 10 km away from the Dübendorf airport. A secondary reference station located on an airport taxiway was used as reference for the ground trajectory. This secondary station's position was determined using a static baseline evaluation referenced to ETHZ.

For the comparison in Table 7.2, the laser scanning height was calculated by interpolating it at the location of each GPS measurement spot using the weighted mean interpolation described in Section 5.4. A comparison of the ground GPS heights with the ones derived from airborne laser altimetry yields a systematic offset of around 0.09 m in 1998, resp. 0.18 m in 1999 (Table 7.2).

| difference $h_{gps} - h_{laser}$ | # of pts | RMS | mean | stddev | $|max|$ |
|---|---|---|---|---|---|
| westward 1998 (line 31) | 1766 | 0.37 | −0.10 | 0.36 | 5.41 |
| eastward 1998 (line 32) | 1856 | 0.35 | −0.07 | 0.34 | 5.00 |
| westward 1999 (line 27) | 2760 | 0.28 | −0.16 | 0.22 | 3.50 |
| eastward 1999 (line 28) | 2705 | 0.24 | −0.20 | 0.12 | 2.29 |

Table 7.2.: Statistics of comparison of laser DSM with GPS derived ground heights.

The flying height above ground was around 500 m. Figure 7.4 shows the difference of the laser data interpolated onto the GPS ground tracks.
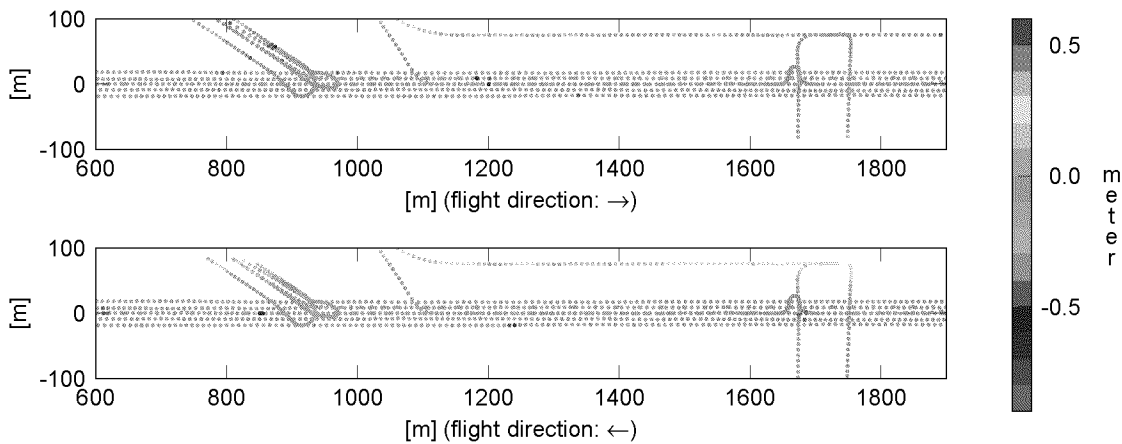


Figure 7.4.: Differences of ground and airborne derived heights at the positions of the ground receivers' locations. The plotted point values are $h_{gps} - h_{laser}$ of 1998.

According to the results in Table 7.2, one can expect the absolute accuracy of the airborne laser scanning data to be on the order of 0.3 m, as long as the reflectance

intensity is strong enough.

## 7.2.2.   Repeatability of Laser Scanning Data

The repeatability of scanned height determination can be studied on one hand by comparing the resulting DSM of the same region from different strips of the same flight, on the other hand by comparing the results from different flights, in our case one year apart from each other.

Figure 7.5 shows the repeatability result of the year 1998. The differences of the two scan strips of 1999 as well as the temporal difference of the DSM from both years is shown in Figure 7.6. The laser scan data was gridded to a regular grid with 5 m spacing using the weighted mean interpolation technique described in Section 5.4. The self-calibration technique described in Section 5.3 was applied to estimate the roll and pitch boresight misalignment angles before the final DSM was calculated. Due to the flat terrain, the yaw misalignment angle could not be determined.

In Figures 7.5 and 7.6, some interesting observations can be made:

- The coupling of the signal to noise ratio with the reflected laser intensity is clearly visible on the dark, newly paved parts of the runway (Figure 7.5). The RMS when calculated restricted to this region rises to about 15 m.

- The instant (e.g. during the very same flight) repeatability of the height measurements is good. The RMS of the difference of the two scan lines flown during the same flight is 0.37 m for 1998 and 0.11 m for 1999.

  The worse result for 1998 is clearly due to the increased blunder at the end of the runway. If the comparison is restricted to the area east of 690800 m easting, the RMS drops to 0.12 m, which is equivalent to the result of 1999.

- The temporal difference of the DSM 1999 minus the DSM 1998 (Bottom of Figure 7.6) show a systematic positive effect in the lawn surrounding the runway. At the eastern end, rectangular shapes of differences on the order of 1 meter can be detected. The temporal comparison shows the effect of different vegetation stands prevailing during the respective flight day.

## 7.2.3.   Increased Blunder Probability With Less Reflected Signal Intensity

To further analyze the blunder in the 1998 data, the interpolation was done reversely. For each laser shot, the corresponding height was interpolated from the coarsely available GPS ground heights. The resulting height difference is plotted in Figure 7.7 against the reflected signal intensity values. They range from 0 to 8191, which corresponds to the range from −83 to −31.5 dB (Hug, 1996).
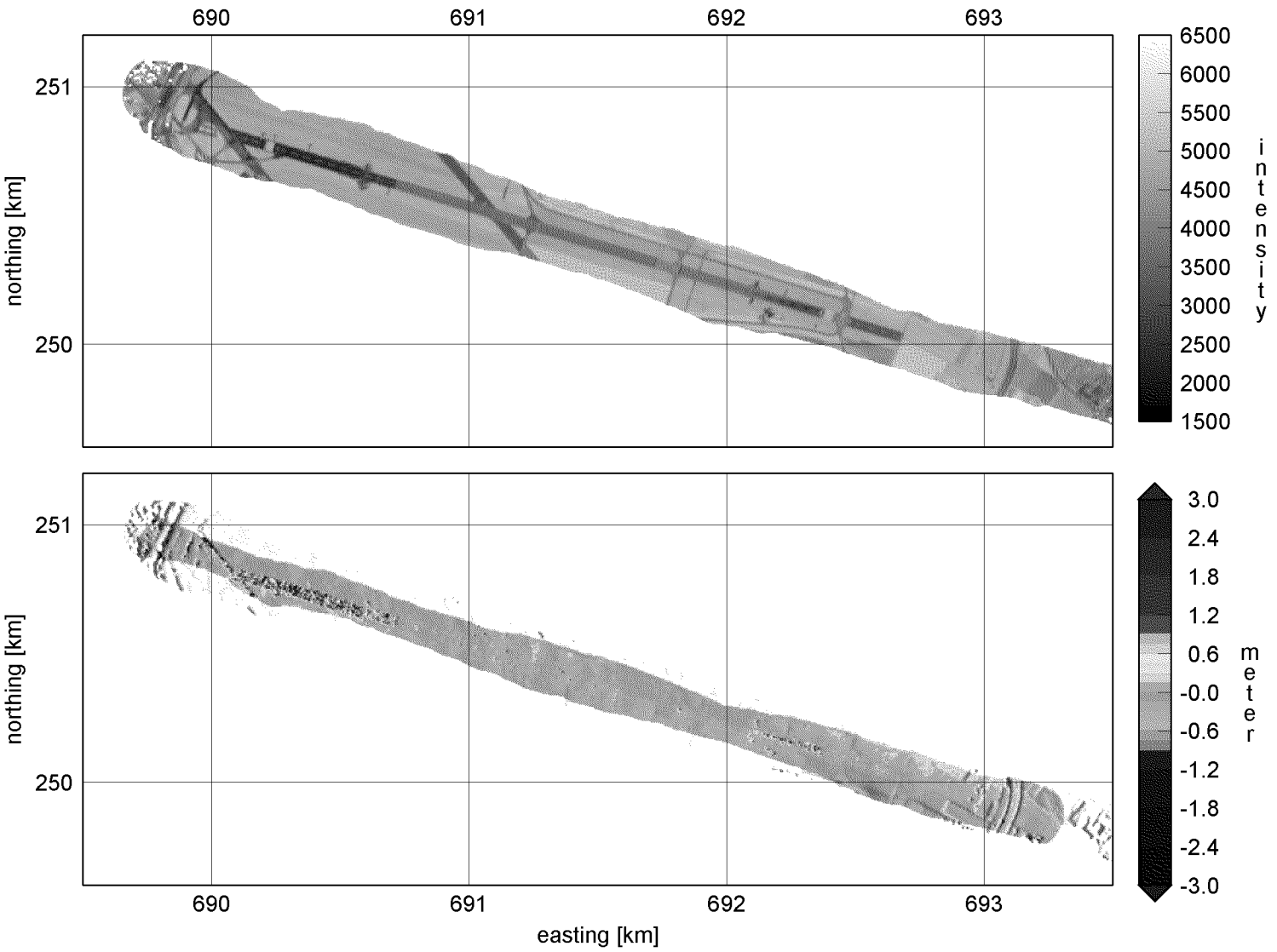
Figure 7.5.: Laser intensity plot (left) and differences of the two laser scan lines' overlap: westward minus eastward (right); (Scale 1:25 000). Note the effect of low reflectance intensity at the first 500 m at the west end of the runway (dark region in the left plot), that was asphalted just the month before the flight.
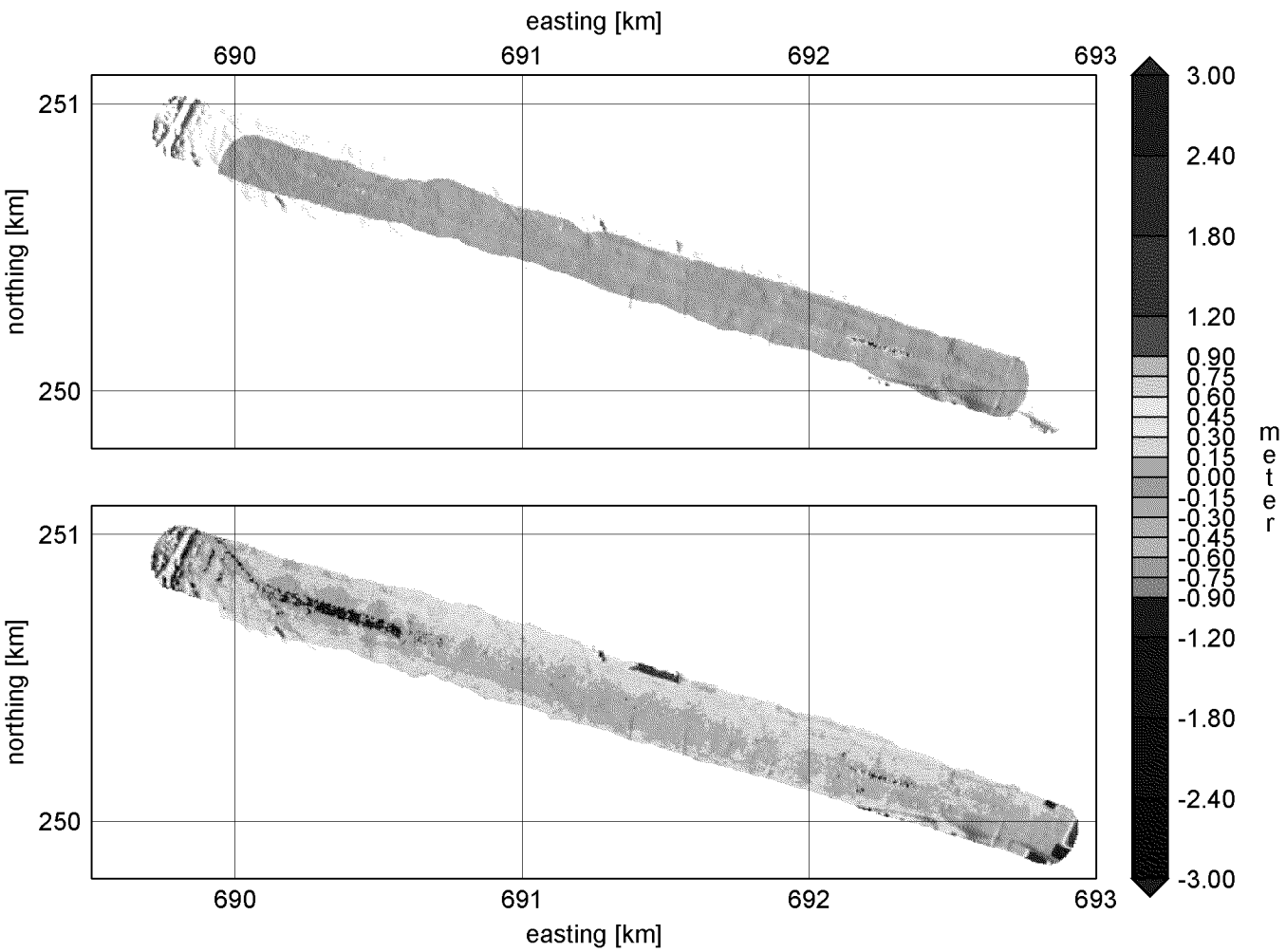
Figure 7.6.: Differences of the two laser scan lines' overlap (1999): east-west minus west-east (left) and temporal difference of the years 1999 minus 1998 (right); (Scale 1:25 000). Apparently, the black tarmac that was asphalted in 1998 does not show the intensity problems in the 1999 data. In the temporal difference plot, several observations can be made: the problems of 1998 of course abide in the difference; at the eastern end, the fields probably have different crop, and the grass height next to the runway was as well different.
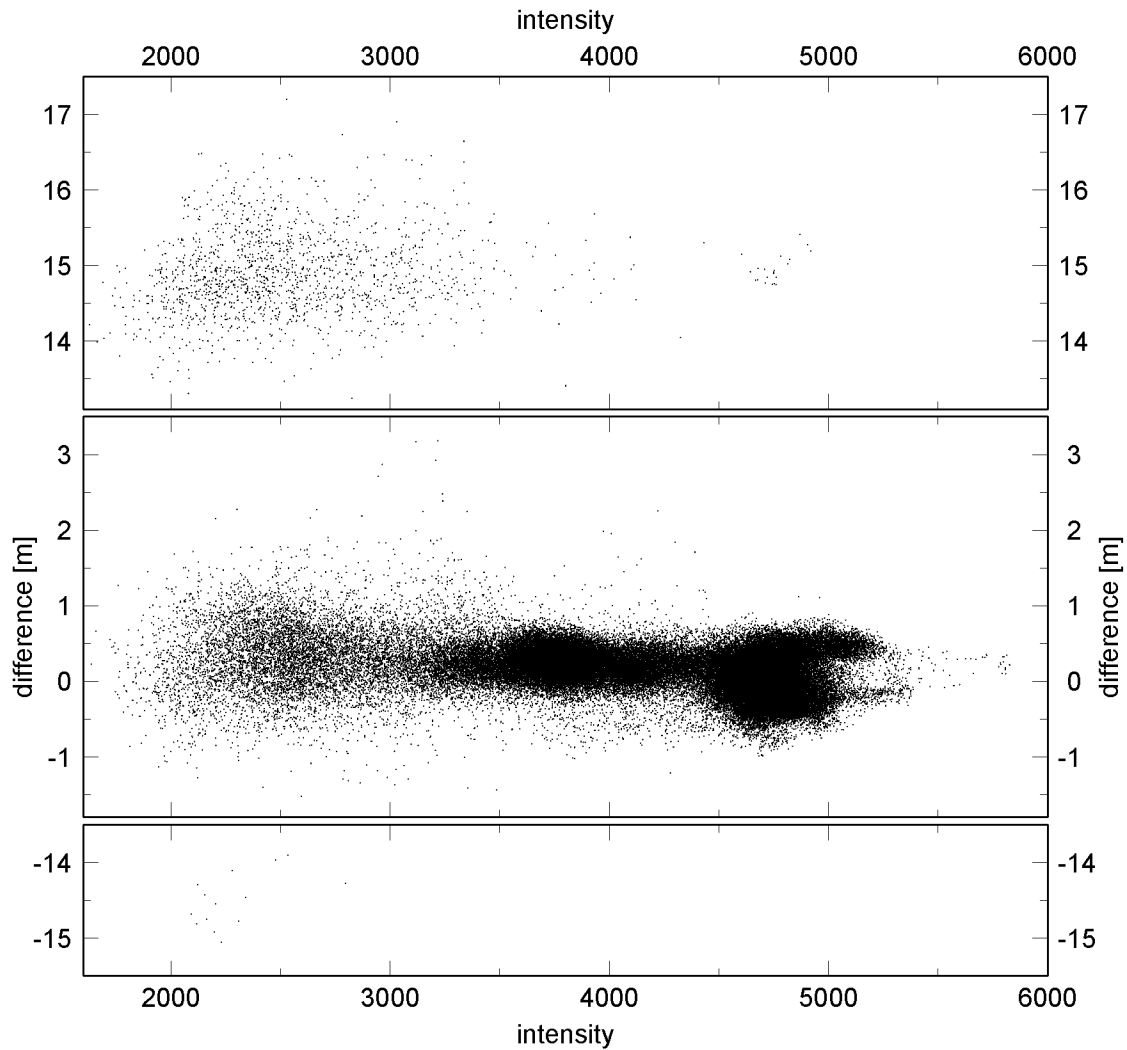
Figure 7.7.: Height difference of single laser shot height minus interpolated GPS height. This plot shows all available data for one scan strip: between −13.5−−1.8 as well as between 3.5–13.1 m there are no data points whatsoever.

Favey, E., 2001. *Investigation and Improvement of Airborne Laser Scanning Technique for Monitoring Surface Elevation Changes of Glaciers.* ETH Zurich, Diss. No. 14045

Obviously, all blunder occurring in this strip is of the magnitude of a multiple of the short modulation wavelength of 15 m. The smaller the reflected intensity gets, the higher is the percentage of blunder (Figure 7.8). Some more detailed statistics are given in Table 7.3.
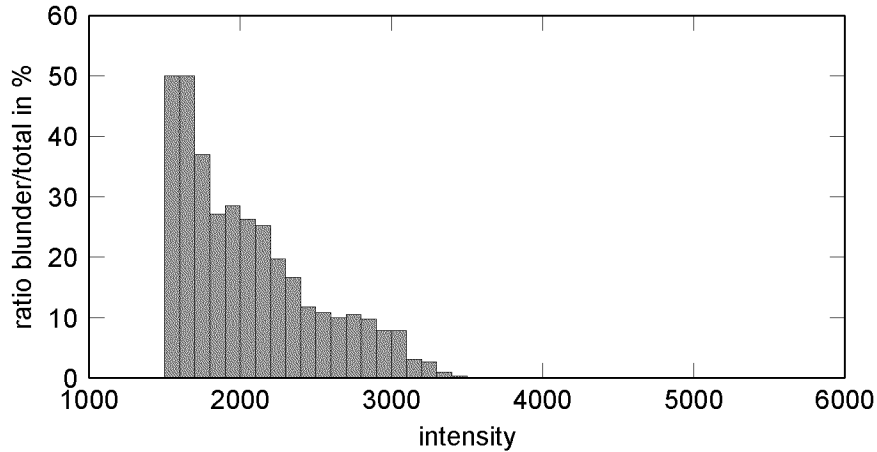


Figure 7.8.: Ratio of blunder vs. total count of measurements divided into intensity bins of width 100.

This is a natural consequence of the c/w distance measurement technique (Hug, 1996). The phase resolution of the 150 m wavelength decreases with decreasing reflected signal strength. If the resolution of the longer wavelength exceeds the higher modulation frequency's longest unambiguous range $R_{\max}$ (Equation 2.7), the determination of the phase position is no longer warranted. The shorter wavelength ambiguity can only be determined correctly, if

$$\lambda_1 \frac{\varepsilon_{\varphi_1}}{2\pi} < \frac{\lambda_2}{2} \tag{7.2}$$

where

$\varepsilon_{\varphi_1}$    : the longer wavelength's phase error due to measurement noise.
$\lambda_1, \lambda_2$: long and short wavelengths of the modulation frequencies, respectively.

This problem of the ambiguity determination is unique to the c/w method and does not occur, if the laser distance measurement is done with a pulsed laser system.

If the data would be filtered with an intensity threshold of 3100, then 89% of the blunder would be filtered out along with about 8% of data with correctly resolved ambiguities. The characteristics of this special blunder distribution led to the blunder removal techniques described in Section 2.2.4.

Objects like houses, trees, or crevasses (in the glacier case) can cause surface height structure of exactly the blunder magnitude. Blunder detection can also be coupled

| data subset | # of pts | stddev [m] | mean [m] | min [m] | max [m] |
|---|---|---|---|---|---|
| $7\,\mathrm{m} < dh$ | 1504 | 0.53 | 14.89 | 13.25 | 17.20 |
| $-7\,\mathrm{m} < dh < 7\,\mathrm{m}$ | 98302 | 0.30 | 0.14 | −1.52 | 3.18 |
| $dh < -7\,\mathrm{m}$ | 14 | 0.36 | −14.50 | −15.05 | −13.90 |

| subset with intensity | percentage of total data | blunder in % of subset |
|---|---|---|
| < 3100 | 9.3% | 14.5% |
| > 3100 | 90.7% | 0.2% |

Table 7.3.: Statistical information for the comparison depicted in Figure 7.7. The top table shows the data divided into subsets by height difference, the bottom table shows the data divided by an intensity threshold. The exact wavelength of the modulation frequency is 14.985 m. Thus the data subsets identify clearly the blunder to be a wrong ambiguity fixing of the short modulation wavelength occurring mainly at low reflectance intensity (cf. Figure 7.8).

with object detection and removal, yet it is virtually impossible to keep blunders and true objects of small size apart.

## 7.2.4.  Conclusions of Runway Results

The laser scanning data of the years 1998 and 1999 flown at 500 m over the runway of the Dübendorf airport were compared with heights determined on the ground using kinematic DGPS. The two strips flown each year were compared with its counterpart of the same year. The resulting DSM of both years were also compared.

The following conclusions can be drawn from these comparisons:

- The data need to be filtered and blunder due to wrong ambiguity fixing needs to be removed.

- The repeatability during the same flight is at the level of the laser scanner distance measurement accuracy of 15 cm.

- The absolute height accuracy (if the GPS ground measurements are taken as 'truth') is as expected on the order of 30 cm (for a flat terrain). No conclusion is drawn for the horizontal component's accuracy.

- A temporal analysis of measurements flown in different years and conclusions thereof are possible with sub-meter accuracy.

- The final result can be biased by a constant offset due to various reasons discussed in the previous chapters. These are e.g. lever arm error, GPS antenna phase center uncertainty, tropospheric mismodeling, or a remaining laser distance bias. It should be noted that especially the first two reasons hold true also for the ground GPS measurements.

## 7.3.  Comparison of Laser DSM with DSMs Derived from Photogrammetry

### 7.3.1.  Description of Available Photogrammetric DSM Data

Aerial photographs of the Unteraargletscher are taken every year at the end of the ablation season. The exact dates of the photo missions are listed in Table 7.4. The photographs of 1998 of Lauteraargletscher were measured manually with a Wild AC1 analytical plotter for comparison reasons. Based on previous experiences of using digital photogrammetry on glaciers (Baltsavias et al., 1996), the performance of three selected digital photogrammetric systems (Match-T, LHS DPW 770, and VirtuoZo) were compared with the manual results. For a detailed analysis of the matching results see Favey et al. (2000). On the other hand, both, the manually and the digitally generated DSMs were used as an independent reference for comparing the laser scanning data in a small selected area.

For the year 1999, the photographs were evaluated using the DPW 770 digital photogrammetric system. That DSM was also compared to the 1999 results of airborne laser scanning.

| year | photo flight | laser flight |
|------|--------------|--------------|
| 1998 | Sept. 9      | Aug. 26      |
| 1999 | Sept. 8      | Sep. 1       |

Table 7.4.: The dates of data acquisition.

Most of the control points in the upper part of the glacier were established in August 1997. The existing sparse set of control points was densified and extended with additional points (Meinck, 1998). Figure 7.3 shows an example of such a control point. They were measured with theodolite and adjusted in a constrained network, where old control points dating back to the 1960s were held fixed. The height accuracy of the control points is on the order of 0.1 m; the horizontal accuracy is on the order of 0.15 m.

The 1998 dataset consists of six B/W images forming a strip and covering the Lauteraargletscher (Figure 7.9). The used RC 30 camera had a focal length of 152 mm and the average image scale was 1:13 000. The overlap was ca. 60% for the inner
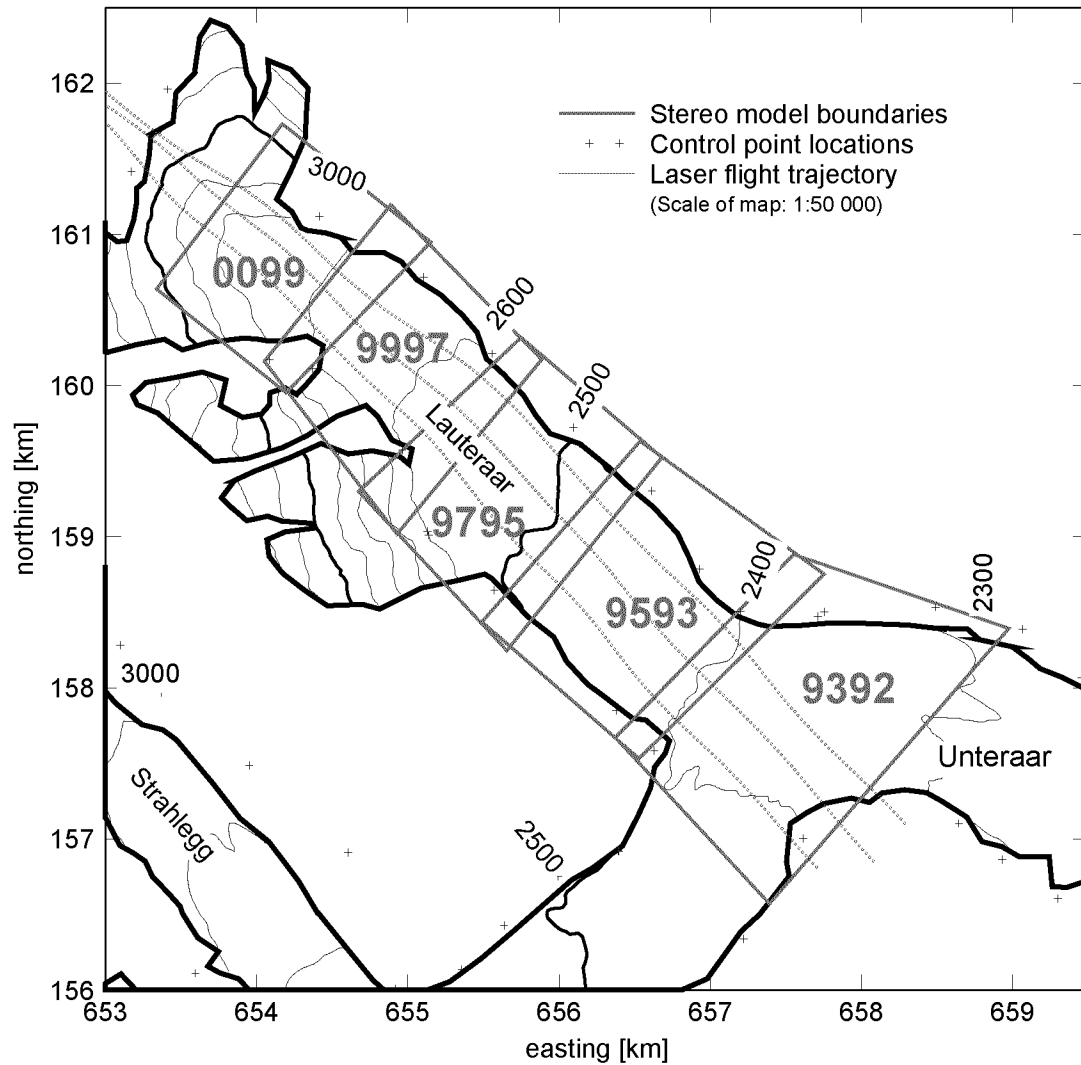
Figure 7.9.: Location of stereo models of the 1998 photogrammetric evaluation on Lauteraargletscher. The black numbers adjacent to the glacier label the contour lines. The green numbers denote the stereo model number.

| Stereopair or dataset[2] | Mean $\nabla Z$ [1][deg ] | Max $\nabla Z$ [1][deg] | $Z$-range [m] | Min $Z$ [m] | Max $Z$ [m] | # of points |
|---|---|---|---|---|---|---|
| 0099 | 23.9 | 56.2 | 442.4 | 2621.4 | 3063.8 | 538 |
| 9997 | 18.9 | 56.9 | 469.3 | 2508.2 | 2977.5 | 787 |
| 9795 | 16.8 | 56.6 | 374.6 | 2440.0 | 2814.6 | 811 |
| 9593 | 18.0 | 59.3 | 452.1 | 2354.4 | 2806.5 | 896 |
| 9392 | 12.9 | 57.3 | 414.7 | 2260.8 | 2713.3 | 1186 |
| All-DSM | 17.6 | 59.5 | 803.1 | 2260.8 | 3063.8 | 4218 |
| All-CLIF | 40.3 | 59.3 | 798.4 | 2265.5 | 3063.8 | 1458 |
| All-GLAC | 9.2 | 42.4 | 792.5 | 2260.8 | 3053.2 | 2760 |

[1]Gradient $Z$ computed from an interpolated 50 m regular grid with Sobel.

[2]Reference data for whole area (DSM), glacier only (GLAC), mountain cliffs only (CLIF).

Table 7.5.: Some data about the photogrammetric dataset.

models and 80% for the two outer ones (0099 and 9392). Table 7.5 shows the characteristics of the terrain with large height range and steep slopes for most models. Model 0099 and 9997 were at the upper glacier part where more textureless snow and ice areas exist. A manual dataset (see Table 7.5) was measured at a Wild AC1 analytical plotter. This consists of a regular grid of 50 m spacing. The estimated accuracy of the measurements was 20 and 40 cm for the inner and outer models respectively. For each model a polygon covering the measured area was defined. These polygons were also divided in areas covering only the glacier and the remaining one (mainly steep mountain cliffs, partly with shadows). This was important as for the comparison only the glacier was important.

The 1998 and 1999 images were scanned with 14 microns at a Zeiss SCAI. The digital images were not further preprocessed and directly used for the digital DSM generation with the DPW 770 system. The control and tie points to be used in the digital evaluation were measured and adjusted with ORIMA at a DPW 770 system. 26 signalized points measured with theodolite and an accuracy of 1 dm were available on Lauteraargletscher. About 70 tie points per model were measured manually. The digital DSMs were generated based on the experiences of the digital evaluations conducted with various digital systems. The 1999 images were not evaluated manually.

The digital images of both years were evaluated for the entire glacier except Finsteraarfirn and Strahleggletscher. Those areas could not be evaluated photogrammetrically. In the case of Strahleggletscher there are no appropriate images available. For the area of Finsteraarfirn, no control points were ever established due to the difficult topography.

## 7.3.2. Comparison of the 1998 Data

To be able to compare the two datasets, the height of the laser scanner data was interpolated from its unevenly distributed points at the location of the photogrammetric grid point. The interpolation was done using the weighted mean approach (Section 5.4) using a correlation length $\varepsilon = 3\,\mathrm{m}$ and an exponent $n = 2$. Table 7.6 shows a statistical analysis of the comparison with the manual reference dataset with 50 m grid spacing, as well as with the 10 m grid of the DPW 770 solution.

For comparison, the laser data was transformed to the Swiss projection system (CH1903+), the geoid undulation was subtracted, and the offset translation according to Section 7.1 was applied.

Flight planning for the laser scanning strips was done for the firn areas of the glacier. This led to a height above ground of 600 m and 1100 m in the stereo models 0099 and 9392 respectively. The received laser signal power at 1100 m flying height above ground was at the limit of S/N ratio. Thus an increased blunder frequency was to be expected, due to the low reflectance intensity especially in the lower models 9392 up to 9795. The main portion of this blunder could be successfully detected and eliminated (cf. Section 6.1). The values in Table 7.6 were calculated with the already cleaned version of the laser scanner data.

### Comparison with Manual Photogrammetry.

A comparison with manual photogrammetric measurements was made both, on a per model basis as well as all points together (Table 7.6). Figure 7.10 shows the distribution of the difference photogrammetry DSM minus laser DSM.

The signed mean values of the difference to the single models show a bias on the order of 0.6 m. The source of this bias could not be identified with certainty. A possible source is a remaining offset due to the weak determination of the local glacier datum, as the reference coordinates that were measured by theodolite do have an unclear history.

For a better analysis of the laser data quality, a second set of laser data was calculated with the additional height bias of the local datum subtracted. Thus the total translation applied was

$$\begin{pmatrix} E_{\mathrm{CH1903+}} \\ N_{\mathrm{CH1903+}} \\ H_{\mathrm{CH1903+}} \end{pmatrix} = \begin{pmatrix} E_{\mathrm{VAW}} \\ N_{\mathrm{VAW}} \\ H_{\mathrm{VAW}} \end{pmatrix} + \begin{pmatrix} 0.05 \\ -0.30 \\ 1.20 \end{pmatrix} \tag{7.3}$$

Figure 7.11 shows the distribution of the differences after this alternate translation was applied. Table 7.6 lists the statistics of both versions.

The upper half of Table 7.6 shows the results of the version, where the translation of Equation 7.1 was applied. In the lower half, the translation of Equation 7.3 was used. The following observations can be made:

| ... dataset minus laser | # pts | RMS [m] | Mean with sign [m] | Max abs. [m] | blunder[1] % |
|---|---|---|---|---|---|
| manual all 0099 | 265 | 1.37 | −0.62 | 7.49 | 12 |
| manual all 9997 | 495 | 1.32 | −0.62 | 16.04 | 8 |
| manual all 9795 | 495 | 1.10 | −0.66 | 6.23 | 7 |
| manual all 9593 | 458 | 2.18 | −0.79 | 18.05 | 7 |
| manual all 9392 | 28 | 5.09 | −2.57 | 15.05 | 23 |
| manual all | 1782 | 1.82 | −0.75 | 18.05 | 9 |
| DPW 770 | 35462 | 1.34 | −0.54 | 38.88 | 6 |
| manual glac 0099 | 241 | 1.06 | −0.69 | 4.58 | 7 |
| manual glac 9997 | 428 | 0.88 | −0.65 | 4.20 | 4 |
| manual glac 9795 | 444 | 0.93 | −0.78 | 3.83 | 3 |
| manual glac 9593 | 380 | 1.28 | −0.78 | 14.67 | 3 |
| manual glac 9392 | 24 | 1.22 | −1.11 | 1.99 | 16 |
| manual glac | 1519 | 1.04 | −0.73 | 14.67 | 4 |
| DPW 770 glac | 33269 | 1.20 | −0.61 | 16.29 | 4 |
| manual[2] all 0099 | 265 | 1.22 | −0.02 | 6.89 | 11 |
| manual[2] all 9997 | 495 | 1.17 | −0.02 | 15.44 | 7 |
| manual[2] all 9795 | 495 | 0.88 | −0.06 | 6.83 | 5 |
| manual[2] all 9593 | 458 | 2.03 | −0.19 | 18.65 | 6 |
| manual[2] all 9392 | 69 | 4.81 | −1.97 | 14.45 | 16 |
| manual[2] all | 1782 | 1.67 | −0.15 | 18.65 | 7 |
| DPW 770[2] | 35651 | 1.37 | −0.02 | 39.18 | 5 |
| manual[2] glac 0099 | 241 | 0.85 | −0.10 | 3.97 | 5 |
| manual[2] glac 9997 | 428 | 0.63 | −0.06 | 3.55 | 3 |
| manual[2] glac 9795 | 444 | 0.57 | −0.18 | 3.47 | 2 |
| manual[2] glac 9593 | 419 | 1.80 | −0.38 | 14.56 | 2 |
| manual[2] glac 9392 | 66 | 4.89 | −2.11 | 14.45 | 14 |
| manual[2] glac | 1598 | 1.46 | −0.27 | 14.56 | 3 |
| DPW 770[2] glac | 33456 | 1.18 | −0.05 | 15.39 | 3 |

[1]Threshold for blunders is 1.7 m. This threshold is calculated as $3\sigma$ where $\sigma^2 = \sigma_l^2 + \sigma_p^2$. A priori accuracies are assumed: for laser scanning $\sigma_l = 0.4$ m (tilted target with an inclination of 10°), and for the photogrammetric dataset $\sigma_p = 0.4$ m.

[2]For this second version, the heuristically determined additional systematic offset of 0.6 m between the laser and the photogrammetric solution was subtracted from the laser points.

Table 7.6.: Comparison of laser data and the photogrammetric dataset of 1998. In the upper part, a comparison of all available points was made. The lower part of the table (glac) contains only the measurements, that were within a defined glacier boundary polygon. All 'glac' points were located on the glacier.
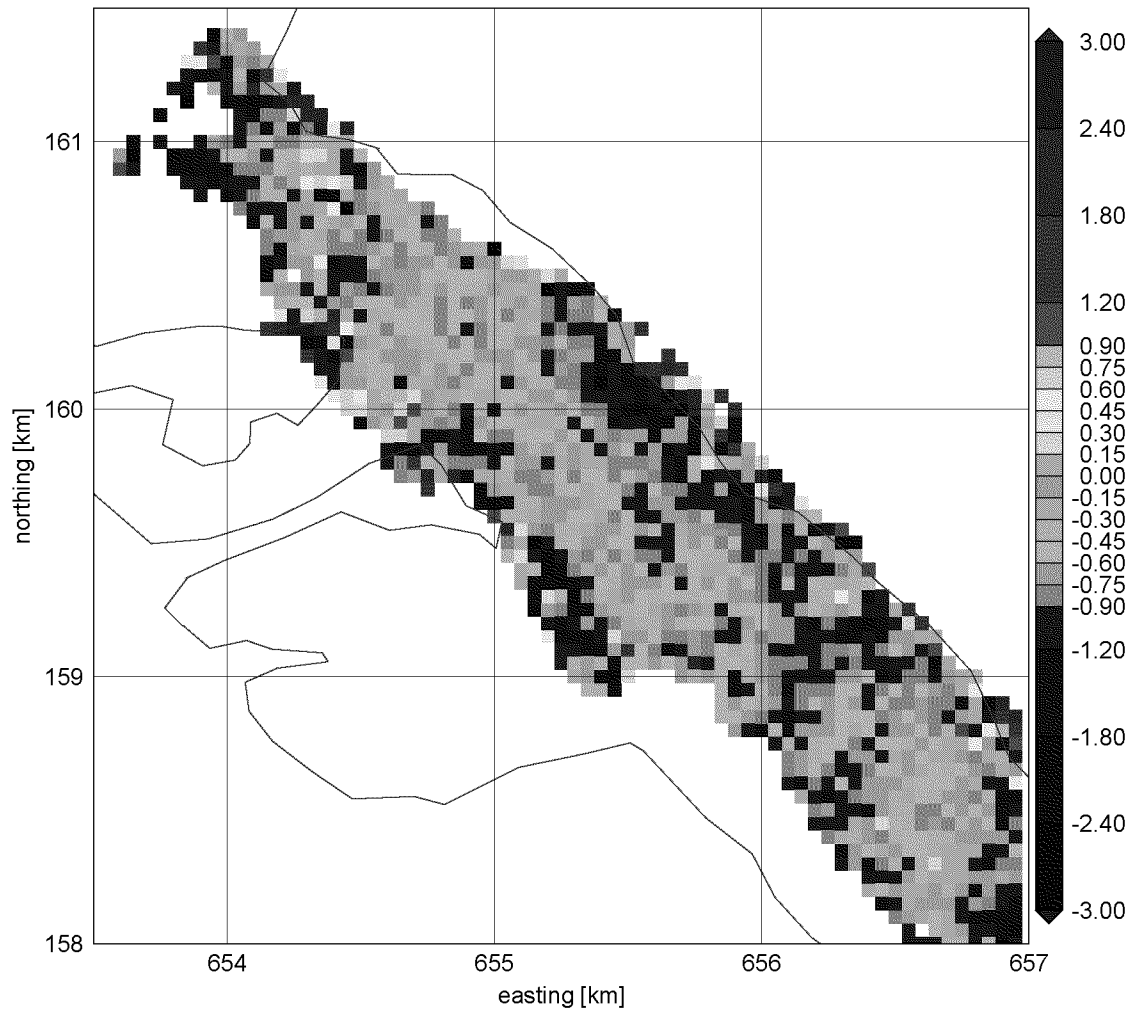
Figure 7.10.: Difference distribution of manual photogrammetry minus laser DSMs for 1998. This graph shows the strong negative systematic offset.
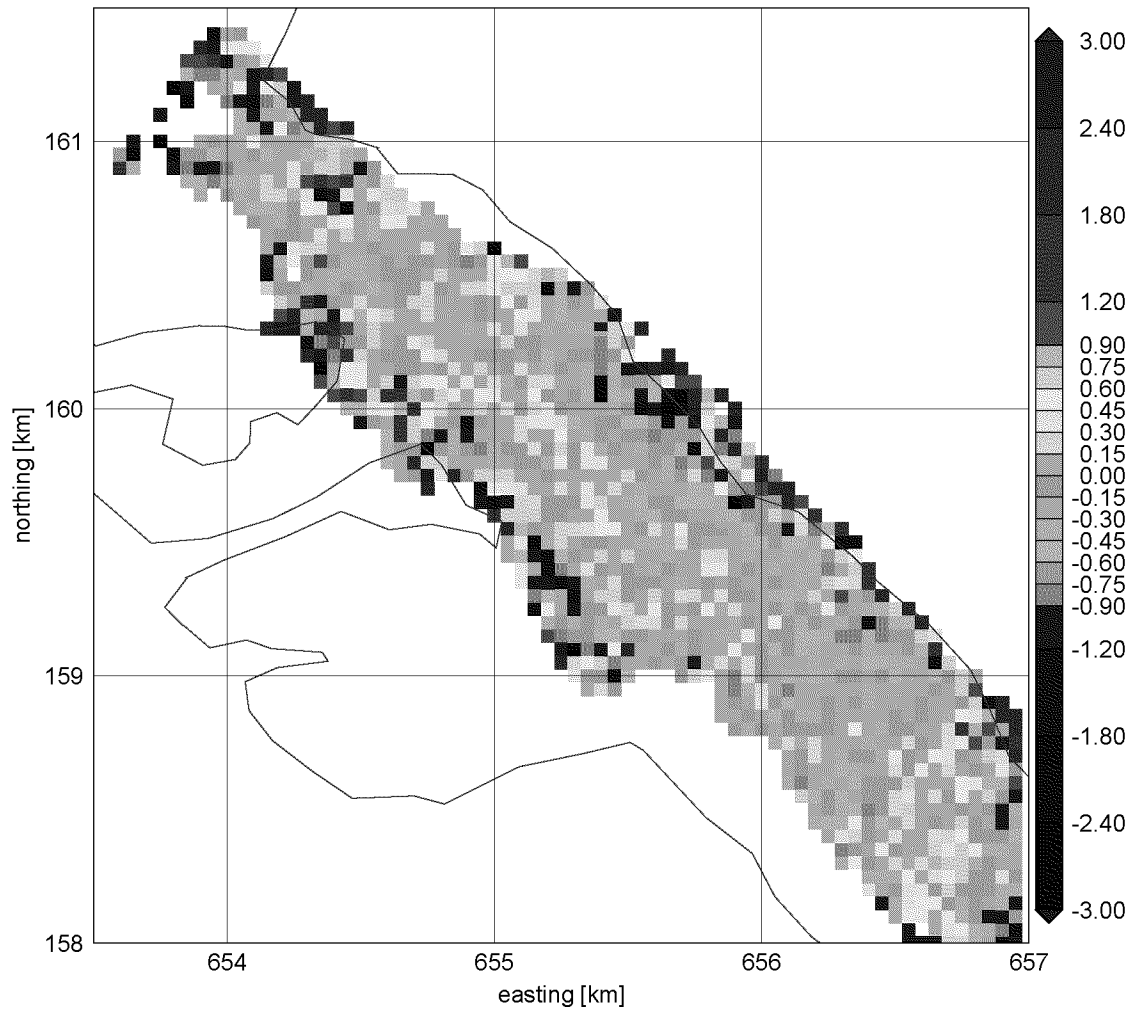
Figure 7.11.: Difference distribution of manual photogrammetry minus laser heights
for 1998. The data used for this plot consists of the laser data minus
the additional systematic offset of 0.6 m.

- The maximum absolute deviation is on the order of the smaller laser wavelength indicating that not all of the laser blunder could be removed by the technique described in Section 2.2.4. A detailed analysis of the performance of this method is given in Section 6.1.2. Note that the maximum difference does not exceed 20 m in the comparison with the manual photogrammetric data.

- In the comparison with model 9997, the maximum absolute deviation drops from 15 to 4 m, when the cliff area is not part of the statistics. Apparently, most of the undetected blunder occurs in the steep cliff areas. The statistics restricted to the glacier area show a strong decrease of the RMS as well as the blunder percentages.

- In the area of model 9392, only a few laser points were measured. This is where the laser distance measurements were at the limit of the possible measuring range. The laser scanner was always already turned on earlier on the strip. Thus this area contains the first received signals with a high blunder rate.

- The second version's comparison restricted to the glacier area shows an RMS below 1 m for the models 0099, 9997, and 9795. In the lower two models, remaining blunder cause a worse result.

Looking at the RMS values, one should keep in mind, that these contain the error components of both, the laser scanning technique, as well as the photogrammetry method. Both methods are entirely independent of each other, with each having its own error budget. This includes exterior orientation, inner orientation, lever arm, GPS and attitude errors and the noise of the laser distance measurements.

**Comparison with Digital Photogrammetry.**

The dataset from digital photogrammetry was available as a 10 m grid. Figure 7.12 thus gives a much finer distribution of the differences. The absolute maximum difference in Table 7.6 amounts to about 40 m in the case of digital photogrammetry, which is due to problems of the photogrammetric matching algorithm (Favey et al., 2000).

The RMS on the glacier amounts to 1.2 m for the whole comparison. The laser scanning's contribution to this rather high RMS value are errors from the dynamic sensitivity of the scanning mirror's inclination. According to Hug (1996), this inclination angle can deviate up to $0.1°$ due to dynamic forces onto the scanning mirror. The maximal error induced onto the ground point position for an inclination angle deviation of $0.1°$ is calculated as:

$$dx_1^{\mathcal{B}} = 2.46 \cdot 10^{-3} \cdot r$$
$$dx_2^{\mathcal{B}} = 3.38 \cdot 10^{-3} \cdot r \qquad (7.4)$$
$$dx_3^{\mathcal{B}} = 0.84 \cdot 10^{-3} \cdot r$$
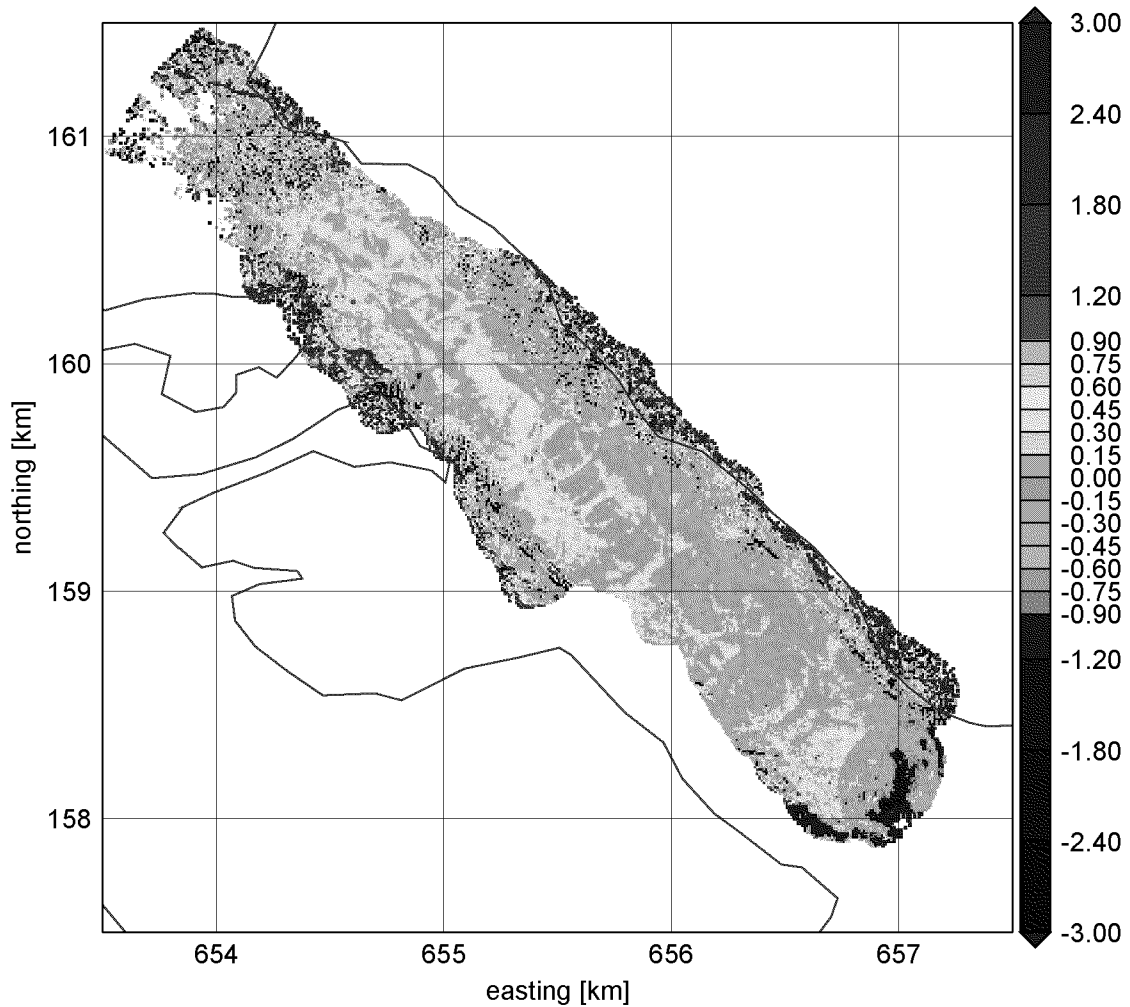
Figure 7.12.: Difference distribution of digital photogrammetry minus laser heights for 1998. Increased noisy differences can be found in the uppermost kilometer at the upper left corner as well as along the steep cliff areas. Most of the remaining glacier area shows smoother differences with systematic effects related to the laser scan pattern.

Favey, E., 2001. *Investigation and Improvement of Airborne Laser Scanning Technique for Monitoring Surface Elevation Changes of Glaciers.* ETH Zurich, Diss. No. 14045

where $r$ is the slant laser range. This shows, that even on a flat terrain, acceleration effects due to strong turbulences can produce an error of almost 1 m .

Figure 7.13 describes the flight conditions prevailing throughout the 1998 laser scan flight. Yet this day was the only slot during a two week's period, when the weather conditions allowed to conduct measurement flights in the mountains.
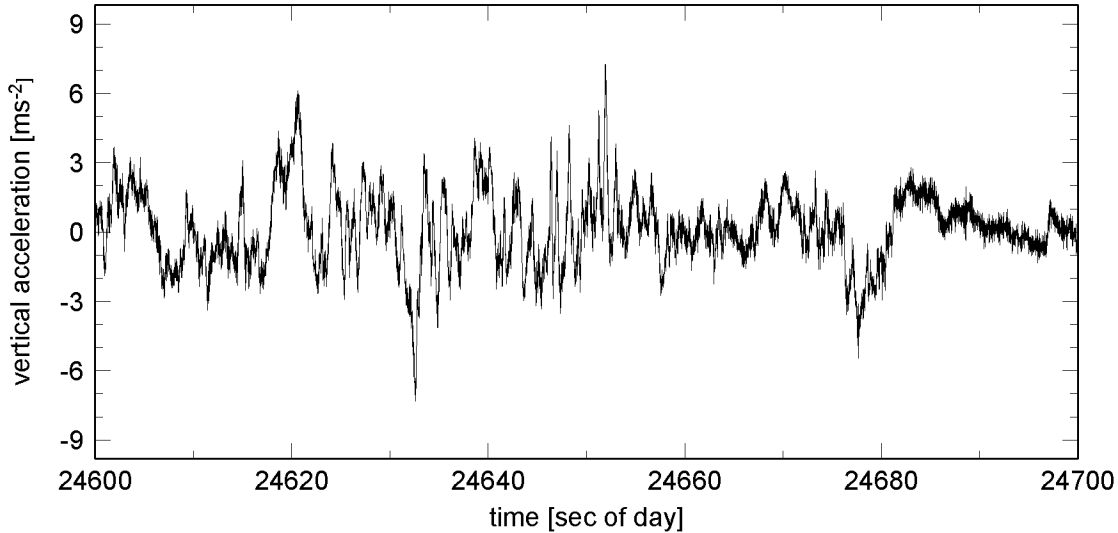


Figure 7.13.: INS acceleration data of the laser strip 9810 (the westmost Lauteraar-strip of 1998). The maximum accelerations on this strip range from $-7.3$ to $7.2$ ms$^{-2}$. Strong winds caused heavy turbulences while flying within the mountains. As soon as the plane was over the Grindelwald area, where all mountains are more than 1 km below flight altitude, the turbulences ceased immediately (from second 24690 onwards).

## 7.3.3.    Comparison of the 1999 Data

The comparison of the 1999 laser data was undertaken the same way as for 1998. The two upper lines of Table 7.7 were calculated with the translational parameters of Equation 7.1, showing the same systematic offset as the comparison statistics of 1998. The statistics of the two bottom lines were thus calculated using Equation 7.3.

The 1999 dataset obviously suffer less from blunder. Restricting the comparison to the glacier area only, shows a good RMS result. The RMS of the differences is on the order of 0.6 m, even though also in this dataset, not all of the 15 m blunder—due to the problem described in Section 7.2.3—could be removed. This corresponds to the theoretical accuracy expected. It is calculated as

$$\sigma = \sqrt{\sigma_l^2 + \sigma_p^2} \qquad (7.5)$$

| laser minus ... dataset | # pts | RMS [m] | Mean with sign [m] | Max abs. [m] | blunder[1] % |
|---|---|---|---|---|---|
| DPW 770 all | 33723 | 1.26 | −0.63 | 32.39 | 3 |
| DPW 770 glac | 32306 | 0.90 | −0.60 | 17.14 | 2 |
| DPW $770^2$ all | 33723 | 1.10 | −0.03 | 31.79 | 3 |
| DPW $770^2$ glac | 32306 | 0.67 | 0.0 | 16.54 | 2 |

[1]Threshold for blunders is 1.7 m. This threshold is calculated as $3\sigma$ where $\sigma^2 = \sigma_l^2 + \sigma_p^2$. A priori accuracies are assumed: for laser scanning $\sigma_l = 0.4$ m (tilted target with an inclination of 10°), and for the photogrammetric dataset $\sigma_p = 0.4$ m.

[2]For this second version, the heuristically determined additional systematic offset of 0.6 m between the laser and the photogrammetric solution was subtracted from the laser points.

Table 7.7.: Comparison of laser data and the photogrammetric dataset of 1999.

where

$\sigma$ : theoretical accuracy to be achieved by evaluating differences. Using the values described below, we get $\sigma = 0.56$ m.

$\sigma_l$ : a priori accuracy of airborne laser scanning, calculated after Equation 2.27. Using also Equation 2.24 and inserting a terrain slope of 10°, $\sigma_l$ is set to 0.4 m

$\sigma_p$ : a priori accuracy of photogrammetry at the current image scale, as described in Section 7.3.1. This value is set to $\sigma_p = 0.4$ m.

The difference distribution depicted in Figure 7.14 shows systematic effects in a laser strip specific pattern. These patterns are related to the differing laser point density at center line and at the strip periphery (cf. Figure 5.3).

The cliff areas are confirmed to be problematic as already seen in the 1998 comparison. Yet, the 1999 data does not show the flight dynamical problems that dominate the 1998 laser dataset.

## 7.3.4. Conclusions of Comparison with Photogrammetry

From the comparison of the acquired airborne laser scanning data with two photogrammetric DSMs of 1998 and 1999, the following thoughts evolve:

- The RMS resulting from the differences is in an absolute sense, i.e. it contains the errors and noise of both methods.

- The geodetic datum transformation described in Section 7.1 does not fully model the systematic offset observed between photogrammetry and laser scanning. A detailed analysis of the coordinate history of the old control points
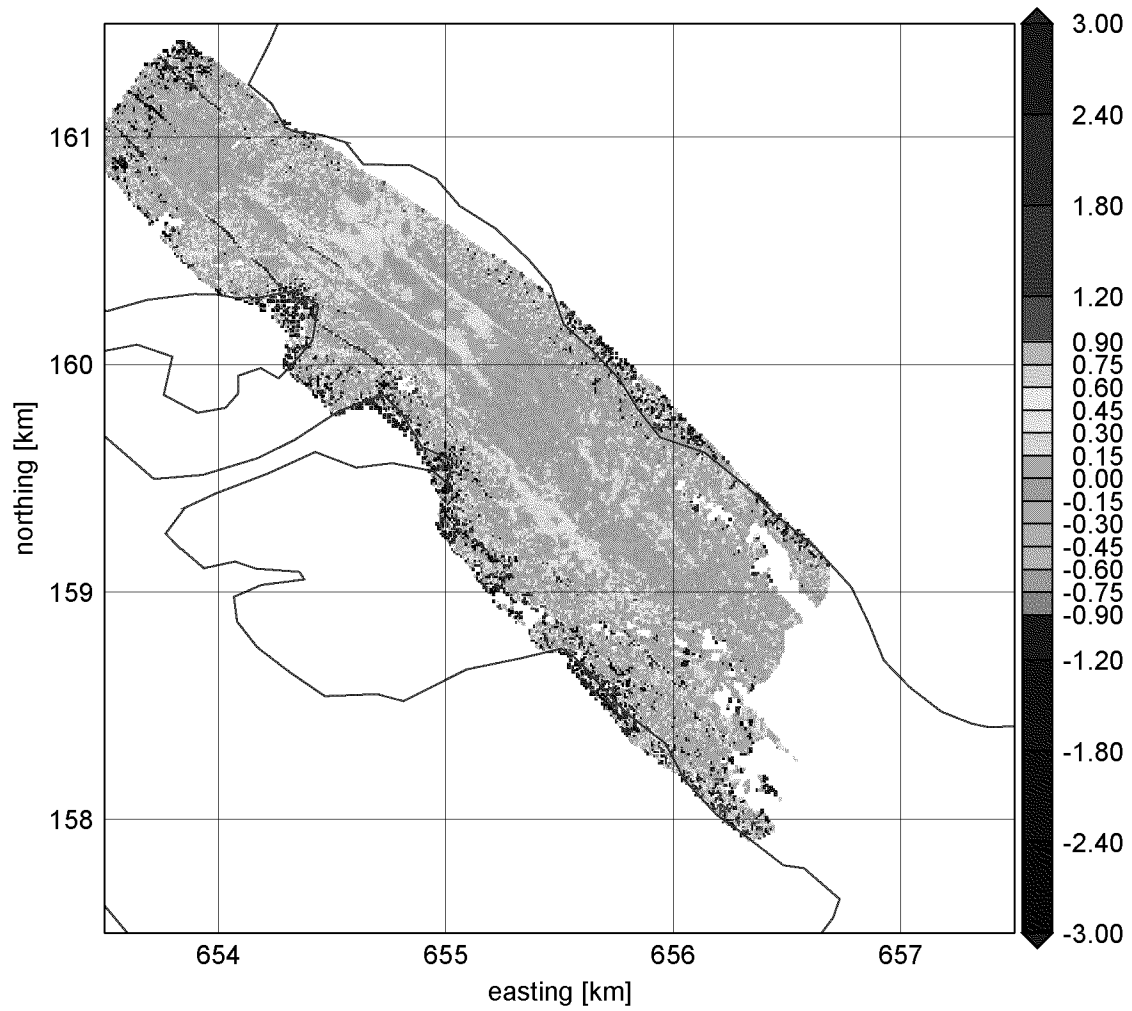
Figure 7.14.: Difference distribution of digital photogrammetry minus laser heights for 1999.

would be needed, as well as the remeasurement of the entire control point network within the LV95 coordinate frame. Yet, for a temporal analysis as described in Section 6.3, this relation is not needed to be known.

- The comparison results of 1998 were worse than expected due to problems with the flight dynamical sensitivity of the scanning mirror.

- Some 15 m blunder remains undetected, mainly in the cliff areas.

- The RMS for 1999 of 0.6 m meets accuracy expectations.

- Cliff areas pose problems to both methods. The laser scanning method has an increased $\sigma$ due to the greater horizontal uncertainty propagating into the height accuracy, as the surface slope increases.

- For the laser scanner, system calibration is more complicated and has a much stronger influence on the accuracy. On the other hand with photogrammetry, processing of the data takes more time, is more complicated and needs more specialized hardware (film development, scanner, digital photogrammetric system).

- Since photogrammetric film cameras usually do not have INS, ground control points, which are difficult and costly to establish and maintain, especially in mountainous regions, are needed. Most of the previously mentioned disadvantages will however disappear with digital photogrammetric cameras currently entering the market. Yet system calibration and dependency on GPS and INS accuracy will then show similar complications and influences as with laser scanning.

While comparing photogrammetry and laser scanning, one has to keep in mind, that the glacier is a constantly changing target. In the region of Lauteraargletscher, it has flow velocities amounting to over 40 m per year (Guðmundsson and Bauder, 1999), which is more than 1 dm per day. For the 15 days difference in 1998 between the laser data measurements and the date, when the photographs were taken, the horizontal displacement of the glacier thus amounts to about 1.6 m.

# 8. Summary and Conclusion

## 8.1. Conclusions

Airborne laser scanning is a powerful tool for the determination of digital surface models and surface elevation change distribution of glaciers. It can be used without any ground control points which are difficult to establish and maintain in a remote alpine environment. The estimates of surface elevation changes are needed with an accuracy of about 0.3–0.5 m to serve as input data for numerical flow models and mass balance determination (Guðmundsson and Bauder, 1999). Since surface roughnesses are on the same order, a better accuracy DSM will hardly result in better estimates of changes in surface altitude.

This work assesses the feasibility of determining the surface elevation change using airborne laser scanning. In cooperation with the Institute of Navigation, University of Stuttgart, their ScaLARS laser scanning system was installed on board the aircraft of the Swiss Federal Office of Topography. It was integrated with a georeferencing system, composed of high-precision kinematic GPS positioning and an attitude determination system. Measurements were realized using the Unteraargletscher as test area.

The key problem consists in bringing together all necessary elements for georeferencing the laser data, where the quality of each contributing part has to be monitored regarding accuracy and systematic effects. Each of the elements in the basic equation of georeferencing was individually scrutinized. Improvements to mitigate identified errors were proposed and successfully applied.

There are several obstacles in using the technique for glaciological purposes. A low flying-height above ground imposes aeronautical difficulties. Measuring in a mountainous environment depends on good weather conditions to a much greater extent than in urban projects. The GPS satellite visibility is often reduced due to obstruction by the topography. These are problems typical to a mountainous environment.

The laser scanning system operates with the continuous wave technique, modulating the laser light with two frequencies. As these modulation frequencies are used for the distance measurements, their ambiguities need to be solved in order to obtain a correct ground height. When the reflected signal intensity is low, the probability

increases that the ambiguity is resolved to a wrong integer. This problem was successfully addressed using a blunder detection algorithm.

The laser scanning mirror showed to be sensitive to aircraft accelerations originating from turbulent flight dynamics. This effect degraded the 1998 dataset along with a reduced GPS satellite visibility due to obstruction. The 1999 dataset did not show these problems.

The generation of digital surface models was successfully completed. The digital surface models of the firn parts of Unteraargletscher derived from the airborne laser scanning measurements of the years 1998 and 1999 were used to estimate the surface elevation change distribution of these areas. The accuracy of the surface elevation change distribution achieved amounts to 0.5 m.

Comparisons with various sources of ground truth were made to study the overall performance of the laser scanning system in general, and specifically for the glaciological application. These comparisons approved the overall laser scanning system to be performing within the postulated specification. Laser scanning measurements over a runway yielded a repeatability RMS of 0.15 m. The RMS of the comparison with known ground heights was 0.3 m. Comparisons with photogrammetric DSMs of the glacier area showed an RMS of 0.6 m, given favorable flight conditions and good satellite visibility.

The areas covered by airborne laser scanning are located between 2500 and 3400 m above sea level. For the period 1998–1999, a surface elevation increase of 2–4 m was measured. This positive change was related to the immense amount of snowfall during the winter 98/99.

The quality of the final DSMs and their temporal analysis depend on the performance of each subsystem contributing to the georeferencing of the laser scanning data. The following main conclusions are drawn for each element individually:

**Laser scanning system:** Its performance was analyzed and an approach for detecting and removing blunder was implemented. The received power dependency of the blunder occurring in steps of 15 m is unique to the continuous wave technique used for distance measurements by the ScaLARS system. A pulsed laser system's accuracy depends the same way on the signal to noise ratio of the received signal, but it will not show this stepwise behavior. These steps are the reason for the blunder in the laser scanning data. The effect of the wrong distance measurements could successfully be mitigated.

The sensitivity of the scanning mirror to the dynamic behavior of the aircraft must be taken into account by choosing smooth flight conditions. This means that wind and turbulence conditions are as much to be regarded in flight planning as other weather aspects like visibility, clouds and fog.

**Attitude solution:** The attitude solution was realized using an inertial measurement unit. A separate attitude solution with lower accuracy using a GPS

multi-antenna array was sucessfully developed and used to control and correct IMU drift and offset errors. The combination of the GPS and the INS attitude shows an accuracy of 0.03°. The attitude solution revealed to be sensitive to vibration effects. The error effects can be diminished, provided the inertial system can be placed as close to the scanning unit as possible, and the entire frame can be shielded against vibrations.

The short term variations in the INS angle error behavior would require modifications to the angle calculation software of the manufacturer, which was not available as source code. Yet the impact of these errors remaining unmodeled by the offset and drift estimation approach is rather small.

The main impact of an incorrect attitude solution is a degraded horizontal accuracy of 1 m or more. This affects the height solution mainly on a topography with steep slopes such as the cliffs surrounding the glacier. By using an better inertial system hardware, this accuracy can be improved. A system with better accuracy figures was tested by Škaloud (1999), who found the orientation accuracy of his system to be better by one order of magnitude.

**Kinematic GPS positioning:** High-precision GPS positioning in kinematic mode was applied for the trajectory solution. The key problem here is the ability of fixing the carrier phase ambiguities. This ability decreases with increased baseline length and height difference relative to the reference station. Error sources like cycle slips, tropospheric refraction, interference, multipath, and antenna phase center variations were identified and appropriately corrected.

Each cycle slip introduces a new unknown ambiguity rendering a weaker determinability. Too many unknown ambiguities that span just over a short amount of time degrade the positioning solution, as the number of unsolved ambiguities increases. The loss of the GPS satellite signals cannot be corrected in postprocessing. Care needs to be taken not to loose the carrier phase lock during turns between the strips. The obstruction potential of the topography in the proximity of the target area needs to be carefully considered during the flight planning.

Introducing path delay values from a 4D-troposphere model does not appear to help resolve more ambiguities. The improvement by getting a less biased height result compared to using a standard atmosphere model is nevertheless considerable.

Radio Frequency Interference (RFI) threatens airborne laser scanning and the use of GPS for precise positioning in general within the proximity of radio stations. The locations of such interfering stations must be taken into account for the flight planning. The harmful influence of RFI onto GPS measurements is a serious issue not only limited to direct georeferencing. If GPS is to be used for airborne precise navigation (Scaramuzza, 1998), the RFI problem needs to be solved, in particular. This however is rather a political, than a technical problem, as the frequencies would need to be reserved for positioning use only.

The existing software approach for kinematic GPS positioning was extended to provide the vectors of the GPS multi-antenna array needed for attitude solution. As the baselines are short, usually all ambiguities can be solved without problem.

**Inner orientation:** The elements of inner orientation were determined and applied. A self-calibration procedure for determining boresight misalignment angles was elaborated. The misalignment angles were found to remain stable for the duration of the entire flight.

In summary, it can be stated that airborne laser scanning for surface elevation change detection is a feasible method complementing the photogrammetric approach.Photographs have the advantage, that they can additionally be used to measure horizontal velocities, using images of different years. Laser scanning is advantageous when used for areas without ground control points or textureless firn areas.

## 8.2.   Recommendations

Ongoing research in DGPS trajectory determination will have a major impact onto the georeferencing of airborne laser scanner data. Attention should be given to atmospheric modeling, multipath and antenna phase center variations of an antenna mounted on a conducting surface, and ambiguity determination improvements over longer baselines by using INS data.

Real-time ambiguity resolution techniques could help identify bad sequences of data already during the measurement flight and introduce the ability to react upon those. The problem to using such methods is the reception of the differential correction signal during the flight. The ASCOT navigation system used for the realization of the laser scan flights is equipped with a differential signal receiver. During the laser scanning flight over the target area, the differential signal was repeatedly lost which lead to problems navigating the strips as planned.

Alternatives to the in-flight calibration of the orientation misalignment angles should be investigated, as the calibration approaches from the laser scanning data suffer from error effects by other hardware parts, such as the sensitivity of the scanning mirror to flight dynamics. In order to keep these error effects isolated from each other, the misalignment angles should be determined within a static mode. On the other hand, the sensitivity of the scanning system to flight dynamics should be investigated and modeled.

The scanning mirror itself has been observed to produce an oscillation of the angle measurements on the order of 0.01–0.02°. This coupling and its effect onto the laser beam direction should be further studied for the specific system used.

The DSMs acquired in the years 1998 and 1999 may serve for comparisons with future DSMs of the Unteraargletscher. To derive surface elevation changes, a future DSM needs to be georeferenced in the same geodetic datum.

# 8.3.   Acknowledgements

I thank all the people who contributed to the successful completion of this work. These are in alphabetical order:

E. Baltsavias, Chair of Photogrammetry and Remote Sensing, ETH Zürich
A. Bauder, Laboratory for Hydraulics, Hydrology and Glaciology, ETH Zürich
M. Baumberger, Swiss Air Force Staff, Dübendorf
H. Bösch, Laboratory for Hydraulics, Hydrology and Glaciology, ETH Zürich
M. Brun, Allnav, Terra Vermessungen AG
B. Bürki, Geodesy and Geodynamics Lab, ETH Zürich
M. Cerniar, Kägi Vermessungen AG
M. Cocard, Geodesy and Geodynamics Lab, ETH Zürich
M. Escher, Swiss Air Force Pilot, Dübendorf
H. Gautschi, Swiss Federal Office of Topography
A. Geiger, Geodesy and Geodynamics Lab, ETH Zürich
A. Grün, Chair of Photogrammetry and Remote Sensing, ETH Zürich
G. Gugger, Swiss Air Force Pilot, Dübendorf
H. Guðmundsson, Lab. for Hydraulics, Hydrology and Glaciology, ETH Zürich
R. Hübscher, Swiss Federal Office of Topography
H.-G. Kahle, Geodesy and Geodynamics Lab, ETH Zürich
A. Kleusberg, Institute of Navigation, University of Stuttgart
U. Marti, Swiss Federal Office of Topography
E. Meier, Remote Sensing Laboratory, University of Zürich
M. Pateraki, Chair of Photogrammetry and Remote Sensing, ETH Zürich
J. Schäffer, iMAR GmbH, St. Ingbert, Germany
O. Schiele, Institute of Navigation, University of Stuttgart
A. Schlatter, Swiss Federal Office of Topography
B. Sierk, National Oceanic and Atmospheric Administration, USA
M. Thomas, Institute of Navigation, University of Stuttgart
M. Troller, Geodesy and Geodynamics Lab, ETH Zürich
E. von Hinüber, iMAR GmbH, St. Ingbert, Germany
A. Wehr, Institute of Navigation, University of Stuttgart
A. Wiget, Swiss Federal Office of Topography
U. Wild, Swiss Federal Office of Topography

My thanks go also to the aircraft mechanics and geodesy students, who helped realize the measurement campaigns. Last but not least, I would like to thank my wife Karin for all her support throughout this work.

This work was supported by the Swiss National Science Foundation grant number 21-47095.96. The Institute of Navigation, University of Stuttgart, is thankfully acknowledged for providing their laser scanning system to the project. The inertial system was made available to this project by iMAR GmbH, St. Ingbert, Germany.

# Bibliography

Aðalgeirsdóttir, G., Echelmeyer, K. A., and Harrison, W. D. (1998). Elevation and volume changes on the Harding Icefield, Alaska. *J. Glaciol.*, 44(148):570–582.

Axelsson, P. (2000). DEM generation from laser scanner data using adaptive TIN models. In *Int'l Archives of Photogrammetry and Remote Sensing, XIXth ISPRS Congress, Amsterdam*, volume XXXIII (B4), pages 110–117.

Bagnaschi, L., Klingelé, E., White, T., and Gatta, S. (1993). Vibrations Analysis for Airborne Gravimetry. Technical report, Institut für Geodäsie und Photogrammetrie, ETH Zürich, Bericht Nr. 223. ISBN 3-906513-37-8, 29 pages.

Baltsavias, E. P., Li, H., Mason, S., Stefanidis, A., and Sinning, M. (1996). Comparison of Two Digital Photogrammetric Systems with Emphasis on DTM Generation: Case Study Glacier Measurement. In *IAPRS*, volume 31, Part B4, pages 104–109. Paper presented at the 18th ISPRS Congress, 9–14 July, Vienna, Austria.

Barrel, H. and Sears, J. E. (1939). The refraction and dispersion of air for the visible spectrum. *Phil. Trans. Royal Soc. London*, A238:6–62.

Bauder, A. (2001). *Bestimmung der Massenbilanz von Gletschern mit Fernerkundungsmethoden und Fliessmodellierungen*. PhD thesis, ETH Zürich. in prep.

Bauder, A. and Guðmundsson, G. H. (1996). Mass balance of a section of Unteraarglacier determined with the use of photogrammetric methods. *Eos Trans. AGU*, 77(46):F194. Fall Meet. Suppl.

Blomenhofer, H. and Hein, G. W. (1995). Tropospheric Effects in DGPS and their Removal During Precision Approach and Automatic Landing. In *International Symposium on Precision Approach and Automatic Landing, 21–24 February 1995, Braunschweig, Germany*. Deutsche Gesellschaft für Ortung und Navigation.

Braasch, M. (1994). Isolation of GPS Multipath and Receiver Tracking Errors. *J. of The Institute of Navigation*, 41(4):415–434.

Bronštejn, I. N. and Semendjaev, K. A. (1987). *Taschenbuch der Mathematik*. Verlag Harri Deutsch, Thun und Frankfurt/Main. 840 p.

Cannon, M. E. and Sun, H. (1996). Experimental assessment of a non-dedicated GPS receiver system for airborne attitude determination. *ISPRS J. Photogram. Rem. Sensing*, 51:99–108.

Chen, J. and Funk, M. (1990). Mass balance of Rhonegletscher during 1882/83–1986/87. *J. Glaciol.*, 36(123):199–209.

Cocard, M. (1995). *High Precision GPS Processing in kinematic mode.*, volume 52. Schweizerische Geodätische Kommission (ed.), geodätisch-geophysikalische arbeiten in der schweiz edition. 139 p.

Cocard, M., Eckert, V., Geiger, A., Bürki, B., and Neiniger, B. (1992). 3D modeling of atmospheric parameters for automatic path delay corrections. In Munck, J. D. and Spoelstra, T., editors, *Proceedings Symposium Refraction of Transatmospheric Signals in Geodesy, The Hague*, volume 36, pages 175–178. Netherlands Geodetic Commission, Publ. on Geodesy, News Series.

Cocard, M., Geiger, A., Kahle, H.-G., Veis, G., and Milas, P. (1997). Regional sea surface determination by using Airborne Laser techniques. In *Annales Geophysicae. XXII General Assembly of EGS*, volume 5 of *Part I Suppl. I*, page C191.

Cohen, C. E., Cobb, H. S., and Parkinson, B. W. (1992). Two Studies of High Performance Attitude Determination Using GPS: Generalizing Wahba's Problem for High Output Rates and Evaluation of Static Accuracy Using a Theodolite. In *Proceedings of ION GPS-92 : Fifth International Technical Meeting of the Satellite Division of the Institute of Navigation : Albuquerque, New Mexico, September 16-18*, pages 1197–1203.

Cohen, C. E. and Parkinson, B. W. (1991). Mitigating multipath error in GPS based attitude determination. In *Guidance and Control 1991, Keystone, Colorado, USA, Advances in the Astronautical Sciences*, volume 74, pages 53–68. American Astronautical Society.

Cohen, C. E. and Parkinson, B. W. (1992). Aircraft Applications of GPS-Based Attitude Determination. In *Proceedings of ION GPS-92 : Fifth International Technical Meeting of the Satellite Division of the Institute of Navigation : Albuquerque, New Mexico, September 16-18*, pages 775–782.

Colombo, O. L. (2000). Ionospheric Tomography Helps Resolve GPS Ambiguities 'On The Fly' at Distances of Hundreds of Kilometers During Increased Geomagnetic Activity. In *IEEE Position, Location and Navigation Symposium, San Diego, March 13-16*, pages 15–21.

Comp, C. J. (1993). Optimal Antenna Configuration for GPS Based Attitude Determination. In *Proceedings of the ION GPS-93, Sixth Internatl. Tech. Meeting of The Satellite Division of The Institute of Navigation, Salt Lake City, Utah, Sept. 22-24*, pages 773–779.

Cramer, M., Stallmann, D., and Haala, N. (2000). Direct georeferencing using GPS/inertial exterior orientation for photogrammetric applications. In *Int'l Archives of Photogrammetry and Remote Sensing, XIXth ISPRS Congress, Amsterdam*, volume XXXIII (B3), pages 198–205.

Danuser, G. (1992). Zeitübertragung und Synchronisation mit GPS: Anwendung in der Ueberwachung verteilter Systeme. Technical report, Institut für Geodäsie und Photogrammetrie, ETH Zürich, Bericht Nr. 196. 72 p.

Echelmeyer, K. A., Harrison, W. D., Larsen, C. F., Sapiano, J., Mitchell, J. E., DeMallie, J., Rabus, B., Aðalgeirsdóttir, G., and Sombardier, L. (1996). Airborne surface profiling of glaciers: a case-study in Alaska. *J. Glaciol.*, 42(142):538–547.

Euler, H.-J. and Hill, C. D. (1995). Attitude determination: exploiting all information for optimal ambiguity resolution. In *Institute of Navigation GPS 95*, pages 1751–1757, Palm Springs, California, U.S.A.

Farrell, J. L. (1976). *Integrated Aircraft Navigation*. Academic Press, New York, London.

Favey, E., Geiger, A., Gudmundsson, G. H., and Wehr, A. (1999). Evaluating the potential of an airborne laser scanning system for measuring volume changes of glaciers. *Geografiska Annaler*, 81A(4):555–561.

Favey, E., Pateraki, M., Baltsavias, E. P., Bauder, A., and Bösch, H. (2000). Surface Modelling for Alpine Glacier Monitoring by Airborne Laser Scanning and Digital Photogrammetry. In *Int'l Archives of Photogrammetry and Remote Sensing, XIXth ISPRS Congress, Amsterdam*, volume XXXIII (B4), pages 269–277.

Favey, E. and Schlatter, A. (1998). Geoidbestimmung am Lac Léman. Technical report, Institut für Geodäsie und Photogrammetrie, ETH Zürich, Bericht Nr. 282. 130 p.

Funk, M., Morelli, R., and Stahel, W. (1997). Mass balance of Griesgletscher 1961–1994: different methods of determination. *Zeitschrift für Gletscherkunde und Glazialgeologie*, 33(1):41–55.

Garvin, J. B. and Williams, R. S. (1993). Geodetic airborne laser altimetry of Breidamerkurjökull and Skeidarárjökull, Iceland, and Jakobshavns Isbræ, West Greenland. *Ann. Glaciol.*, 17:379–385.

Geiger, A. (1987). Einfluss richtungsabhängiger Fehler bei Satellitenmessungen. Technical Report 130, Institute of Geodesy and Photogrammetry, ETHZ, Zürich. 40 p.

Geiger, A. (1988). Simulating Disturbances in GPS by Continuous Satellite Distribution. *Journal of Surveying Engineering*, 114(4):182–194.

Geiger, A. (1996). Verzerrungs-Analyse, Interpolation and Approximation. Technical report, Institut für Geodäsie und Photogrammetrie, ETH Zürich, Bericht Nr. 254. ISBN 3-906513-75-0, 1/96, pages 48.

Geiger, A., Cocard, M., Peter, Y., and Kahle, H.-G. (1994). Precise DGPS and Self Calibrating Laser Altimetry for Airborne Marine Geoid Determination and Detection of Glacial Fluctuation. In *Proceedings of ION GPS-94, 7th International Technical Meeting of The Satellite Division of The Institute of Navigation, Part 1, Salt Lake City, Utah, September 20–23*, pages 471–476.

Geiger, A., Schlatter, A., Cerniar, M., and Favey, E. (1997). Einmessung V+D-Flugzeug. Internal report to V+D. 10 p.

Goldfarb, J. M. and Schwarz, K. P. (1985). Kinematic positioning with an INS—differential GPS. In *First International Symposium on Precise Positioning with the Global Positioning System*, volume 2, pages 757–772.

Greenspan, R. (1995). Inertial Navigation Technology from 1970–1995. *J. of The Institute of Navigation*, 42(1):165–185.

Grün, A., Cocard, M., and Kahle, H.-G. (1993). Photogrammetry and kinematic GPS results of a high accuracy test. *Photogrammetric Engineering and Remote Sensing*, 59(11):1643 – 1650.

Gubler, H. (1998). Physik von Schnee. Lecture Notes, ETH Zürich.

Guðmundsson, G. H. (1999a). Measurements of temporal variations in vertical and longitudinal strain rates associated with a short-term speed-up event on Unteraargletscher, Bernese Alps, Switzerland. *J. Glaciol.* submitted.

Guðmundsson, G. H. (1999b). A three-dimensional numerical model of the confluence area of Unteraargletscher, Bernese Alps, Switzerland. *J. Glaciol.*, 45(150):219–230.

Guðmundsson, G. H. and Bauder, A. (1999). Towards an indirect determination of the mass-balance distribution of glaciers using the kinematic boundary condition. *Geogr. Ann.*, 81A(4):575–584.

Guðmundsson, G. H., Bauder, A., Lüthi, M., Fischer, U. H., and Funk, M. (1999). Estimating rates of basal motion and internal ice deformation from continuous tilt measurements. *Ann. Glaciol.*, 28. in press.

Guðmundsson, G. H., Iken, A., and Funk, M. (1997). Measurements of ice deformation at the confluence area of Unteraargletscher, Bernese Alps, Switzerland. *J. Glaciol.*, 43(145):548–556.

Haala, N. and Brenner, C. (1999). Extraction of buildings and trees in urban environments. *ISPRS Journal of Photogrammetry & Remote Sensing*, 54(2–3):130–137.

Hatch, R. (1990). *Kinematic systems in geodesy, surveying and remote sensing.*, chapter Instantaneous Ambiguity Resolution, pages 299–308. K. P. Schwarz and G. Lachapelle (eds.), Springer, New York, Berlin, Heidelberg.

Höflinger, W. (1993). Entwicklung von 3D Meteo-Modellen zur Korrektion der troposphärischen Refraktion bei GPS-Messungen. Technical Report 216, Institute of Geodesy and Photogrammetry, ETHZ, Zürich. IGP-Bericht.

Huber, P. J. (1964). Robust estimation of a location parameter. *Ann. Math. Stat.*, 35(1):73–101.

Hug, C. (1996). *Entwicklung und Erprobung eines abbildenden Laseraltimeters für den Flugeinsatz unter Verwendung des Mehrfrequenz-Phasenvergleichsverfahrens.* PhD thesis, Universität Stuttgart, Deutsche Geodätische Kommission, München. Reihe C, Heft Nr. 457, 122 p.

Jóhannesson, T., Raymond, C. F., and Waddington, E. D. (1989). Time-scale for adjustment of glaciers to changes in mass balance. *J. Glaciol.*, 35(121):355–369.

Kennett, M. and Eiken, T. (1997). Airborne measurement of glacier surface elevation by scanning laser altimeter. *Ann. Glaciol.*, 24:293–296.

Kerr, T. (1994). Use of GPS/INS in the Design of Airborne Multisensor Data Collection Missions (for Tuning NN-based ATR algorithms). In *Proceedings of 7th Int. Techn. Meeting of Institute of Navigation (ION) GPS*, pages 1173–1188.

Kilian, J. (1994). Calibration Methods for Airborne Laser Systems. In *ISPRS Commission I Symposium*. ISPRS.

Klingelé, E., Cocard, M., Kahle, H.-G., and Halliday, M. (1997). Kinematic GPS as a source for airborne gravity reduction: The airborne gravity survey of Switzerland. *J. Geophysical Research*, 102(B4):7705–7715.

Krabill, W., Thomas, R., Jezek, K., Kuivinen, K., and Manizade, S. (1995). Greenland ice sheet thickness changes measured by laser altimetry. *Geophys. Res. Lett.*, 22(17):2341–2344.

Krabill, W. B. and Martin, C. F. (1987). Aircraft positioning using Global Positioning System carrier phase data. *Navigation: J. Inst. Navig.*, 34(1):1–21.

Kraus, K. and Pfeifer, N. (1998). Determination of terrain models in wooded areas with airborne laser scanner data. *ISPRS J. Photogram. Rem. Sensing*, 53(4):193–203.

Kruse, L. P. (2000). *Spatial and Temporal Distribution of Atmospheric Water Vapor using Space Geodetic Techniques.* PhD thesis, Swiss Federal Institute of Technology, ETH Zürich. 125 p.

Lindenberger, J. (1993). *Laser-Profilmessungen zur topographischen Geländeaufnahme*. PhD thesis, Universität Stuttgart, Deutsche Geodätische Kommission, München. Reihe C, Heft Nr. 400.

Lipman, J. S. (1992). Trade-Offs in the Implementation if Integrated GPS Inertial Systems. In *Proceedings of ION GPS-92 : Fifth International Technical Meeting of the Satellite Division of the Institute of Navigation : Albuquerque, New Mexico, September 16-18*, pages 1125–1133.

Lipp, A. and Gu, X. (1994). Cycle-Slip Detection and Repair in Integrated Navigation Systems. In *Proceedings of IEEE PLANS, Las Vegas, 11–15 April*, pages 681–688.

Lipp, A., Stolz, R., Discher, C., and Tiemeyer, B. (2000). Effects of Aircraft Surfaces on GPS Signal Reception. In *Proceedings of GNSS 2000, Edinbourgh, May 1–4*. on CD-rom.

Lu, G. (1995). Development of a GPS Multi-Antenna System for Attitude Determination. Technical Report 20073, University of Calgary, Dept. of Geomatics Engineering. 185 p.

Maas, H.-G. (2000). Least-squares matching with airborne laserscanning data in a TIN structure. In *Int'l Archives of Photogrammetry and Remote Sensing, XIXth ISPRS Congress, Amsterdam*, volume XXXIII (B3), pages 548–555.

Maas, H.-G. and Vosselman, G. (1999). Two algorithms for extracting building models from raw laser altimetry data. *ISPRS Journal of Photogrammetry & Remote Sensing*, 54(2–3):153–163.

Markley, F. L. (1988). Attitude Determination Using Vector Observations and the Singular Value Decomposition. *The Journal of the Astronautical Sciences*, 36(3):245–258.

Marti, U. (1997). *Geoid der Schweiz 1997*, volume 56. Schweizerische Geodätische Kommission (ed.), Geodätisch-geophysikalische Arbeiten in der Schweiz edition. 140 p.

Marti, U. and Egger, D. (1999). Bezugssysteme in der Praxis—Geodätische Bezugssysteme und Koordinatentransformationen für den GPS-Anwender. Technical Report 99-20, Swiss Federal Office of Topography.

Meier, M. F. (1984). Contribution of small glaciers to global sea level. *Science*, 226(4681):1418–21.

Meinck, M. (1998). Untersuchungen zum Fliessverhalten von Gletschern. Diplomarbeit, FH für Vermessungswesen, Hochschule für Technik und Wirtschaft Dresden. 90 p.

Merhav, S. (1996). *Aerospace Sensor Systems and Applications*. Springer Verlag, Berlin. 454 p.

Mohamed, A. H. (1999). *Optimizing the Estimation Procedure in INS/GPS Integration for Kinematic Applications*. PhD thesis, Dept. of Geomatics Engineering, Univ. of Calgary, Canada. 212 p.

NIMA (2000). Department of Defense World Geodetic System 1984—Its Definition and Relationships with Local Geodetic Systems. Technical Report 8350.2, National Imagery and Mapping Agency, USA. Third Edition, 172 p.

O'Brien, H. W. and Munis, R. H. (1975). Red and near-infrared spectral reflectance of snow. Technical Report 332, Cold Regions Research And Engineering Laboratory, Corps of Engineers, U.S. Army.

Oerlemans, J. (1994). Quantifying global warming from the retreat of glaciers. *Science*, 264(5156):243–245.

Oerlemans, J. and Fortuin, J. P. F. (1992). Sensitivity of glaciers and small ice caps to greenhouse warming. *Science*, 258(5079):115–117.

Østrem, G. and Brugman, M. (1991). Glacier mass-balance measurements — a manual for field and office work. Technical report, National Hydrology Research Institute of Norway. Science Report No. 4.

Østrem, G. and Haakensen, N. (1999). Map comparison or traditional mass-balance measurements: which method is better. *Geogr. Ann.*, 81A(4):703–711.

Press, W. H., Teukolsky, S. A., Vetterling, W. T., and Flannery, B. P. (1992). *Numerical Recipes in C—The Art of Scientific Computing*. Cambridge University Press, Cambridge, UK.

Rasmussen, L. A. (1988). Bed topography and mass-balance distribution of Colombia Glacier, Alaska, U.S.A, determined from sequential aerial photography. *J. Glaciol.*, 34(117):208–216.

Reynaud, L., Vallon, M., and Letréguilly, A. (1986). Mass-balance measurements: problems and two new methods of determining variations. *J. Glaciol.*, 32(112):446–454.

Saastamoinen, J. (1973). Contributions to the Theory of Atmospheric Refraction / Introduction to Practical Computation of Astronomical Refraction. Bulletin géodésique Nrs 105, 106, 107, pp.50.

Santerre, R. and Beutler, G. (1993). A proposed GPS method with multi-antennae and single receiver. *Bulletin Géodésique*, 67:210–223.

Sapiano, J. J., Harrison, W. D., and Echelmeyer, K. A. (1998). Elevation, volume and terminus changes of nine glaciers in North America. *J. Glaciol.*, 44(146):119–135.

Scaramuzza, M. (1998). *Systematic Investigations of Error and System-Modelling of Satellite Based Flight Approaches and Landings in Switzerland*, volume 58. Schweizerische Geodätische Kommission (ed.), Geodätisch-geophysikalische Arbeiten in der Schweiz edition. 155 p.

Schmid, H. H. (1977). Ein allgemeiner Ausgleichungs-Algorithmus für die numerische Auswertung in der Photogrammetrie. Technical Report 22, Institute of Geodesy and Photogrammetry, ETH Zürich.

Schwarz, K.-P., El-Mowafy, A., and Wei, M. (1992). Testing a GPS Attitude System in Kinematic Mode. In *Proceedings of ION GPS-92 : Fifth International Technical Meeting of the Satellite Division of the Institute of Navigation : Albuquerque, New Mexico, September 16-18*, pages 801–809.

Schwarz, K. P. and Wei, M. (1994). Aided Versus Embedded—A Comparison of Two Approaches to GPS/INS Integration. In *Proceedings of IEEE PLANS, Las Vegas, 11–15 April*, pages 314–322.

Schwitter, M. P. and Raymond, C. F. (1993). Changes in the longitudinal profiles of glaciers during advance and retreat. *J. Glaciol.*, 39(133):582–590.

Seeber, G. (1993). *Satellite geodesy: foundations, methods and applications.* de Gruyter, Berlin, New York. 531 p.

Škaloud, J. (1995). Strapdown INS Orientation Accuracy with GPS Aiding. Master's thesis, Dept. of Geomatics Engineering, Univ. of Calgary, Canada. 89 p.

Škaloud, J. (1999). *Optimizing Georeferencing of Airborne Survey Systems by INS/DGPS.* PhD thesis, Dept. of Geomatics Engingeering, Univ. of Calgary, Canada. 160 p.

SMA-Annalen (1864–1999). *Annalen der Schweizerischen Meteorologischen Anstalt.* Zürich.

Söhne, W. (1996). *Ein hybrides System in der Geodäsie; Einsatz des NAVSTAR GPS mit dem Strapdown-Inertial-Navigationssystem LASERNAV II für kinematische Punktbestimmung und Orientierung.* PhD thesis, Technische Hochschule Darmstadt, Deutsche Geodätische Kommission, München. Reihe C, Heft Nr. 463.

Söhne, W., Heinze, O., and Groten, E. (1994). Integrated INS/GPS System for High Precision Navigation Applications. In *Proceedings of IEEE PLANS, Las Vegas, 11–15 April*, pages 310–313.

Teunissen, P. J. G. (1994). A New Method for Fast Carrier Phase Ambiguity Estimation. In *Proceedings of IEEE PLANS, Las Vegas, 11–15 April*, pages 562–573.

Thiel, K.-H. and Wehr, A. (1999). Calibration Procedures of the Imaging Laser Altimeter and Data Processing. In *Joint Workshop of ISPRS WGs I/1,I/3, and IV/4: Sensors and Mapping from Space, Univ. Hannover*, volume 18. on CD-Rom.

Thomas, M. (2000). Personal communication. Institute of Navigation, University of Stuttgart.

Thomas, R., Krabill, W., Frederick, E., and Jezek, K. (1995). Thickening of Jakobshavns Isbræ, West Greenland, measured by airborne laser altimetry. *Ann. Glaciol.*, 21:259–262.

Troller, M., Cocard, M., and Geiger, A. (2000). Modellierung 4 dimensionaler Refraktionsfelder zur Berechnung von Weglängen-Korrekturen bei Satellitenmessungen. *Proc.: Simulation raumbezogener Prozesse: Methoden und Anwendungen, 26.9.2000, Münster*, IfGI prints(Nr.9).

van Graas, F. and Braasch, M. (1991). GPS Interferometric Attitude and Heading Determination: Initial Flight Test Results. *J. of The Institute of Navigation*, 38(4):297–316.

Vaughn, C. R., Bufton, J. L., Krabill, W. B., and Rabine, D. (1996). Georeferencing of airborne laser altimeter measurements. *Int. J. Remote Sensing*, 17(11):2185–2200.

Wahba, G. (1965). A Least Squares Estimate of Spacecraft Attitude. *SIAM Review*, 7(3):409.

Wehr, A. and Lohr, U. (1999). Airborne laser scanning—an introduction and overview. *ISPRS Journal of Photogrammetry & Remote Sensing*, 54(2–3):68–82.

Wertz, J. R., editor (1978). *Spacecraft Attitude Determination and Control*. Kluwer Academic Publishers, The Netherlands. 858 p.

Wessel, P. and Smith, W. H. F. (1998). New, improved version of Generic Mapping Tools released. *Eos Trans AGU*, 79(47):579.

Wübbena, G., Schmitz, M., Menge, F., Böder, V., and Seeber, G. (2000). Automated Absolute Field Calibration of GPS Antennas in Real-Time. In *ION-GPS 2000, Sept. 19–22, Salt Lake City*. on CD-Rom.

Zumbühl, H. and Holzhauser, H. (1988). Alpengletscher in der Kleinen Eiszeit. *Die Alpen*, 64(3):322. 3. Quartal, Sonderheft zum 125. jährigen Jubiläum des SAC.

Zumbühl, H. and Holzhauser, H. (1990). Alpengletscher in der Kleinen Eiszeit. *Geographica Bernensia*. Band G 31. Ergänzungsband zu 'Die Alpen 64(3)'.

Favey, E., 2001. *Investigation and Improvement of Airborne Laser Scanning Technique for Monitoring Surface Elevation Changes of Glaciers.* ETH Zurich, Diss. No. 14045

# A. Rotational Issues

## A.1. Approximation of the Derivation of a Rotation Matrix

A rotation is split up into its composing elementary rotations:

$$\boldsymbol{R} = \boldsymbol{R}_3(\vartheta_3)\boldsymbol{R}_2(\vartheta_2)\boldsymbol{R}_1(\vartheta_1) \tag{A.1}$$

with

$$\boldsymbol{R}_1 = \begin{pmatrix} 1 & 0 & 0 \\ 0 & \cos\vartheta_1 & \sin\vartheta_1 \\ 0 & -\sin\vartheta_1 & \cos\vartheta_1 \end{pmatrix} \quad \boldsymbol{R}_2 = \begin{pmatrix} \cos\vartheta_2 & 0 & -\sin\vartheta_2 \\ 0 & 1 & 0 \\ \sin\vartheta_2 & 0 & \cos\vartheta_2 \end{pmatrix} \quad \boldsymbol{R}_3 = \begin{pmatrix} \cos\vartheta_3 & \sin\vartheta_3 & 0 \\ -\sin\vartheta_3 & \cos\vartheta_3 & 0 \\ 0 & 0 & 1 \end{pmatrix}$$
$$\tag{A.2}$$

Linearized for $\vartheta_i \to d\vartheta_i$, this becomes

$$\boldsymbol{R}_i \approx (\boldsymbol{I} + \boldsymbol{I}_i \cdot d\vartheta_i) \tag{A.3}$$

with

$$\boldsymbol{I}_1 = \begin{pmatrix} 0 & 0 & 0 \\ 0 & 0 & 1 \\ 0 & -1 & 0 \end{pmatrix} \quad \boldsymbol{I}_2 = \begin{pmatrix} 0 & 0 & -1 \\ 0 & 0 & 0 \\ 1 & 0 & 0 \end{pmatrix} \quad \boldsymbol{I}_3 = \begin{pmatrix} 0 & 1 & 0 \\ -1 & 0 & 0 \\ 0 & 0 & 0 \end{pmatrix} \tag{A.4}$$

and therefore

$$\boldsymbol{R}(d\boldsymbol{\vartheta}) = \prod_{i=1}^{3} \boldsymbol{R}_i(d\vartheta_i) \approx \boldsymbol{I} + \sum_{i=1}^{3} \boldsymbol{I}_i \cdot d\vartheta_i = \boldsymbol{I} + \boldsymbol{\Omega} \tag{A.5}$$

where $\boldsymbol{\Omega}$ is the skew symmetric matrix:

$$\boldsymbol{\Omega} = \sum_{i=1}^{3} \boldsymbol{I}_i \cdot d\vartheta_i = \begin{pmatrix} 0 & d\vartheta_3 & -d\vartheta_2 \\ -d\vartheta_3 & 0 & d\vartheta_1 \\ d\vartheta_2 & -d\vartheta_1 & 0 \end{pmatrix} \tag{A.6}$$

If $\boldsymbol{R_0}$ is a rotation with approximate angles $\boldsymbol{\vartheta}_0$, so that $\boldsymbol{R}(\boldsymbol{\vartheta}_0 + d\boldsymbol{\vartheta})$ is linearized as $\boldsymbol{R_0}\boldsymbol{R}(d\boldsymbol{\vartheta})$, and if $\boldsymbol{k}$ is an arbitrary vector, we can say

$$
\begin{aligned}
\boldsymbol{R}(\boldsymbol{\vartheta}_0 + d\boldsymbol{\vartheta})\boldsymbol{k} \approx \boldsymbol{R_0}(\boldsymbol{I} + \boldsymbol{\Omega})\boldsymbol{k} &= \boldsymbol{R_0}\boldsymbol{k} + \boldsymbol{R_0}\boldsymbol{\Omega}\boldsymbol{k} \\
&= \boldsymbol{R_0}\boldsymbol{k} + \boldsymbol{R_0}\boldsymbol{K}d\boldsymbol{\vartheta}
\end{aligned}
\tag{A.7}
$$

with

$$
\boldsymbol{K} = \begin{pmatrix} 0 & -k_3 & k_2 \\ k_3 & 0 & -k_1 \\ -k_2 & k_1 & 0 \end{pmatrix}
\tag{A.8}
$$

Thus the derivation of the rotation of the vector $\boldsymbol{R}(\boldsymbol{\vartheta}_0 + d\boldsymbol{\vartheta})\boldsymbol{k}$ is approximated by the derivation of its linearization as given in Equation A.7:

$$
\left. \frac{\partial(\boldsymbol{R}\boldsymbol{k})}{\partial \boldsymbol{\vartheta}} \right|_{\boldsymbol{\vartheta}_0} \approx \boldsymbol{R_0}\boldsymbol{K}
\tag{A.9}
$$

# B. Refraction

## B.1.  Influence of refraction onto laser beam

The refraction index $n$ of visible and infrared light can be expressed as (Barrel and Sears, 1939):

$$N = (n - 1) \cdot 10^6 \;\; = \;\; N_G \frac{273.16}{T} \frac{p}{1013.25} - \frac{11.20}{T} e \qquad (B.1)$$

$$\text{where } N_G = (n_G - 1) \cdot 10^6 \;\; = \;\; 287.604 + 3\frac{1.6288}{\lambda^2} + 5\frac{0.0136}{\lambda^4}$$

and

$N_G$ : group refraction number at 0°C and 1013.25 mbar.
$\lambda$ : laser wavelength [$\mu$m]
$T$ : atmospheric temperature at the laser site in Kelvin [K].
$p$ : atmospheric pressure at the laser site [mbar].
$e$ : water vapor pressure at the laser site [mbar].

For $T$, $p$, and $e$ we use values of a standard atmosphere modelled as a function of the height $h$:

$$T(h) \;\; = \;\; T_0 + \gamma h + 273.16 \qquad (B.2)$$

$$p(h) \;\; = \;\; p_0 \cdot e^{-\frac{h}{H_p}} \qquad (B.3)$$

$$e(h) \;\; = \;\; e_0 \cdot 10^{-\frac{h}{H_e}} \qquad (B.4)$$

with $T_0 = 15\,°\text{C}$ at sea level, $\gamma = -6.5 \cdot 10^{-3}\,°\text{C/m}$, $p_0 = 1023.25\,\text{mbar}$ at sea level, $H_p = 8000\,\text{m}$, $e_0 = 17\,\text{mbar}$ at sea level, and $H_e = 4500\,\text{m}$.

Thus, for a horizontal distance measurement (with $n_0 = $ index at altitude of calibration measurements) we get:

$$s + \Delta s \;\; = \;\; \int_0^s n_0 dh = n_0 s \qquad (B.5)$$

Favey, E., 2001. *Investigation and Improvement of Airborne Laser Scanning Technique for Monitoring Surface Elevation Changes of Glaciers.* ETH Zurich, Diss. No. 14045

For a vertical range, as with the laser measurement in our case from the aircraft to the ground, we use a linear approximation of $n(h)$ ($n_a$ = index at altitude of aircraft, $n_g$ = index at altitude of glacier ground point):

$$
\begin{aligned}
s + \Delta s &= \int_0^s n(h)\, dh = \int_0^s \frac{n_a + n_g}{s} h\, dh = \frac{n_a + n_g}{s} \cdot \frac{1}{2} h^2 \Big|_0^s \\
&= \frac{n_a + n_g}{2} \cdot s
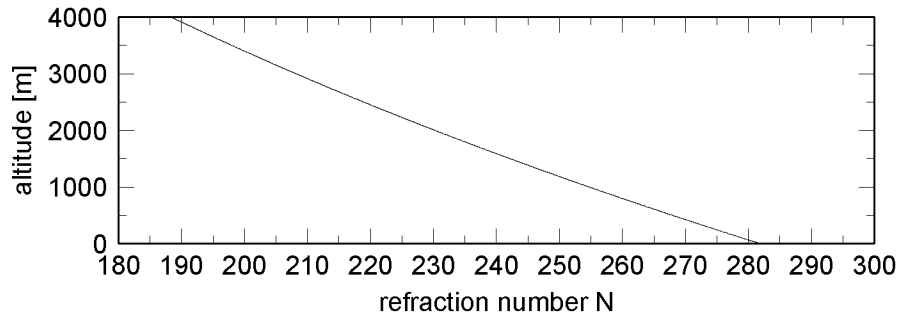\end{aligned}
\tag{B.6}
$$



Figure B.1.: Refraction number $N$ as a function of altitude $h$ for a standard atmosphere

# Curriculum Vitae

Name:            Etienne Favey

Date of birth:   October 26, 1971

Place of birth:  Männedorf, Switzerland

Nationality:     Swiss

## Education

1978–1984: Primary school, Stäfa (ZH)

1984–1986: Secondary school, Stäfa (ZH)

1986–1990: Mathematisches Naturwissenschaftliches Gymnasium Rämibühl, Zürich

1988–1989: Amarillo High School, Amarillo, TX

1991–1992: Seminar für Pädagogische Grundausbildung, Zürich

1992–1997: Swiss Federal Institute of Technology, Zürich, Environmental Engineering and Geodesy

## Degrees

1990: Matura Typus C, Mathematisches Naturwissenschaftliches Gymnasium Rämibühl, Zürich

1997: Diploma in Geodesy, ETH Zürich

## Professional Positions

1994–1997: Student Assistant, Institute of Geodesy and Photogrammetry, ETH Zürich

1997–2000: Assistant, Geodesy and Geodynamics Laboratory, Institute of Geodesy and Photogrammetry, ETH Zürich